Universidade de Coimbra
Faculdade de Ciências e Tecnologia

Masters in Astrophysics and Space Instrumentation

Finding a needle in a haystack: Background studies & WIMP detection efficiency in LUX

Paulo Alexandre Brinca Costa Brás

Advisor
Alexandre Miguel Ferreira Lindote

Advisor
Francisco Filipe Bento Neves

"This thesis does not include the reviews and suggestions done by the Jury"

Finding a needle in a haystack: Background studies & WIMP detection efficiency in LUX

Sumário

A pesquisa pela esquiva Matéria Escura, que compõe a maior parte da massa do nosso Universo, está actualmente em curso. Experiências de detecção de matéria escura de vanguarda e incrivelmente sensíveis exploram vários cenários propostos por diferentes modelos teóricos, sendo um dos quais o da existência de partículas pesadas que interagem por força fraca, ou WIMPs na sigla inglesa. A deteção de possíveis eventos de interação destas partículas com átomos de matéria comum é o objectivo das experiências de detecção directa de matéria escura, das quais a experiência LUX é actualmente aquela que apresenta a maior sensibilidade.

No trabalho desenvolvido nesta tese, exploramos as evidencias da existência da matéria escura e como esta ajuda a moldar o Universo que observamos actualmente, analisamos a modulação do halo de matéria escura que se postula envolver a nossa galáxia e o que se espera observar numa experiência de detecção directa desta matéria. Fazemos também uma análise do principio de funcionamento do detector da experiência LUX e da sua construção. O cerne deste trabalho incide sobre o modelo de fundos radiogénicos e de activação de materiais, por neutrões gerados por muões cósmicos, durante a primeira operação de recolha de dados para a procura de WIMPs que ocorreu desde Abril a Agosto de 2013, as principais implicações destes fundos na experiência LUX e um estudo da eficiência desta experiência para deteção de eventos de recuos nucleares como os esperados das interações de partículas WIMP.

Finding a needle in a haystack: Background studies & WIMP detection efficiency in LUX

Abstract

The search for the elusive dark matter that makes up most of the matter content of our Universe is currently underway. Several state-of-the-art and incredibly sensitive Dark Matter detection experiments are currently exploring different scenarios that could explain the existence of this exotic matter, one of which is the existence of Weakly Interacting Massive Particles, or WIMPs. The detection of possible interaction events of these particles with ordinary matter atoms in a target material is the purpose of Dark Matter direct detection experiments, of which the LUX experiment presents the current highest sensitivity.

In the work presented in this thesis, we explore the evidences for the existence of Dark Matter, the way it helps in shaping the Universe we observe today, the modulation of the Dark Matter halo that is postulated to envelop our galaxy and what is expected to be observed in a direct detection experiment. We also analyse the basic operating principles of the LUX detector and its main components. The core of this work focuses on the analysis of the radiogenic and muon-induced background model for the first WIMP search run that occurred from April to August 2013, the main implications of these backgrounds in the LUX experiment and an analysis of the detection efficiency of nuclear recoil events, as the ones expected from WIMP interaction.

Acknowledgements

This work is dedicated to all people that contributed to my academic endeavour and personal fulfilments.

To my family, for providing me with as much education and opportunities as possible.

Never have I felt more at home than at the $E.5$ office of the Physics Department, University of Coimbra. A special thanks to the LIP Dark Matter Group. To the Doctors Alexandre Lindote and Francisco Neves, I could not have picked more dedicated and inspiring mentors, that provided all the help I needed in my integration, the valuable advices and the tireless patience. To Doctor Claudio Silva for all the help and occasional jump-scares (perks of working back-to-back at the office). To Researcher Vladimir Solovov and to Filipa Balau for all the help and support.

A very special thanks to Professor Doctor Maria Isabel Silva Ferreira Lopes, for inviting me into this amazing adventure and providing me with this unique opportunity, for all the support in my academic endeavour and for all the good advices that I will surely never forget.

I would like to express my thanks to the entire LUX Community, for welcoming me in their midst and for all the support they have provided throughout this work.

One last appreciation to the Jury: Professor Doctor José Lopes Pinto da Cunha, Doctor José Carvalho Maneira and Doctor Alexandre Lindote, that made the effort of reading this thesis.

Acronyms

BAO	Baryon Acoustic Oscillations
BG	Background
CMB	Cosmic Microwave Background
DM	Dark Matter
DPF	Data Processing Framework
DRU	Differential Rate Unit
ER	Electron Recoil
LUX	Large Underground Xenon
LXe	Liquid Xenon
LZ	LUX-ZEPLIN
MACHO	Massive Astrophysical Compact Halo Object
NR	Nuclear Recoil
PHE	Photoelectron
PMT	Photomultiplier Tube
RQ	Reduced Quantities
SM	Standard Model
SURF	Sanford Underground Research Facility
WIMP	Weakly Interactive Massive Particle

Contents

Chapter 1

Introduction

“As for me, I am tormented with an everlasting itch for things remote. I love to sail forbidden seas [...]”

– Herman Melville, *”The Whale”*.
Quoted from the book “Pale Blue Dot”, by Carl Sagan.

Several experimental evidences suggest that approximately 95% of the content of the Universe is in some forms not entirely understood, and dark matter accounts for most of its mass [CK09]. These evidences come from accurate measurements of galactic rotation curves, velocities of galaxies in clusters, gravitational lensing created by non-luminous massive structures associated with galactic clusters, mapping of large scale structures, precise measurement of the cosmic microwave background (CMB) fluctuations and relative abundance of light elements [BHS05, BCnG10]. A strong evidence supporting dark matter was published in 2006 with the measurement of weak-lensing of the Bullet cluster [CBG+06]. Further evidence in favour of dark matter was provided by the Planck mission in 2015, with new CMB measurements of unprecedented precision [PA+15]

Dark matter may be composed of not yet observed weakly interactive massive particles (WIMPs), and models supporting WIMP candidates are being probed by a variety of experiments - either by direct detection through scattering in terrestrial detectors, indirect detection by observing WIMP annihilation products in high density dark matter regions, and particle accelerator searches [Sch10, JKG96, A+13b, CHL15].

The current best limit for the WIMP-nucleon scattering cross section was obtained by LUX: the largest detector ever operated using dual-phase xenon technology, operating at the Sanford Underground Research Facility [A+13e]. Improvements in key areas such as shielding, cryogenics and background reduction allowed the LUX detector to reach an unprecedented sensitivity of $7.6 \times 10^{-46}\ cm^2$ with a 85.3 day run [A+13e].

In the work presented in this thesis, a detailed analysis of the radiogenic and muon-induced background model for the first WIMP search run of LUX is presented, along with the main implications of these backgrounds in the LUX experiment and a computational analysis of the detection efficiency of nuclear recoil events in the LUX detector, as the ones expected from WIMP interaction with the liquid xenon target of LUX.

A brief historical approach of the Dark Matter subject is presented in Chapter 2, along with the underlying Physical and Cosmological theories as well as evidences that support the existence of Dark Matter. The modelling and parametrization of the galactic dark matter halo surrounding our Milky Way galaxy, along with some calculations of dark matter interaction rates and the expected nuclear recoil energy spectrum, is covered in Chapter 3. An additional approach to the dark matter halo as a non canonical isothermal sphere and the main consequences in the quantities calculated is also described in this chapter. The basic functioning principle and components of the LUX detector are described in Chapter 4. The modelling of the major background sources in the LUX detector is the main focus of Chapter 5, along with complementary studies of simulated γ-ray sources and simulation tools. The analysis of the simulated WIMP nuclear recoil detection efficiency in LUX is covered in Chapter 6, with a brief reflection on the main contributions of the detector response to an interaction event and major processing stages used by the LUX collaboration to treat data obtained by the detector. Some final conclusions are presented on Chapter 7.

Chapter 2

Dark Matter

A substantial fraction of the matter in our Universe is in a form that is not yet understood. Several scientific evidences agree with the existence of this unseen matter [CK09, BHS05, BCnG10, CBG$^+$06] that does not absorb, emit or scatter light, and is therefore labelled as "dark".

Dark matter was first postulated to resolve the "missing mass" problem – the observation of large cosmological structures such as galaxies and clusters of galaxies indicated that a larger fraction of the mass of the system was not detectable, and the observed mass from the visible component accounted only a small fraction of the total mass inferred. In 1933 the swiss astronomer Fritz Zwicky (Figure 2.1 on the left) first proposed dark matter to justify the large differences on the mass of the Coma cluster (Abell 1656) calculated by galactic motion and inferred by the visible matter in it [Zwi33, Zwi37]. One year before, the dutch astronomer Jan Oort (Figure 2.1 in the middle) had postulated that additional (unseen) mass was necessary to explain the fast stellar motion in our neighbourhood [Oor32], but these findings could be explained by dim structures composed of regular matter such as white dwarf stars. Nevertheless, Oort gave a crucial contribution to the controversial "missing mass" subject.

Zwicky applied the Virial theorem to the coma cluster in order to estimate its mass from the relative motion of the galaxies in it, assuming that the system was in equilibrium and all galaxies were tightly bound by gravity with no net expansion, contraction or rotation. The Virial theorem relates the average over time of the kinetic (E_K) and potential (Ω) energies of a N-particle system bound by potential forces and is, for a system in these conditions, given by Eq. 2.1 [Cun15].

$$2\langle E_K \rangle = -\langle \Omega \rangle \tag{2.1}$$

The theorem is based on general assumptions and holds true even for very complicated systems where an exact solution of the average kinetic energy $\langle E_K \rangle$ is not trivial.

Zwicky determined the average radial velocity of the galaxies in the cluster by measuring their redshift z – the increase in wavelength of light from a distant source due to the rate of increase in distance of the radiative body to Earth, in this case caused by the relative motion of the galaxies. With this technique only the component of the velocity pointing towards the observer can be measured. Assuming that the radial projection of the velocity is, on average, equal to the other orthogonal projections, *i.e.* $\langle v^2 \rangle = 3\langle v_r^2 \rangle$ [Zwi37], and excluding the overall Coma cluster redshift, the average kinetic energy can be calculated as in Eq. 2.2

$$\langle E_K \rangle \approx \frac{M_c}{2}\langle v^2 \rangle = \frac{3}{2}M_c\langle v_r^2 \rangle \tag{2.2}$$

where M_c is the mass of the cluster. The average gravitational potential energy for the same cluster is given by Eq. 2.3

$$\langle \Omega \rangle \approx -\frac{GM_c^2}{R_c} \tag{2.3}$$

where G is the gravitational constant and R_c is the radius of the cluster that encompasses the mass M_c. The radius of the cluster can be obtained by measuring its distance to the observer, using the overall redshift of the object, and the apparent angular size of the cluster.

Using Eq. 2.1 and combining Eqs. 2.2 and 2.3 the mass of the cluster can be estimated, as demonstrated in Eq. 2.4 [Cun15].

$$M_c = \frac{3}{G}\langle v_r^2 \rangle R_c \tag{2.4}$$

The value obtained by Zwicky for the mass of the Coma cluster, using the Virial theorem, was $M_c = 4.5 \times 10^{13} \ \ M_\odot$, nearly 170 times the mass that he could infer from luminosity [Zwi37]. Zwicky called this mass that was not being accounted *"dunkle materie"* – german for "dark matter".

More recent approaches of the Coma cluster mass problem account for the interstellar gas, that comprises most of the baryonic (regular) matter content of the cluster, and use precise values of the Hubble constant, not so rigorously calculated at the time. The Coma cluster mass is closer to $M_c \approx 2 \times 10^{15} \ \ M_\odot$, meaning that less than 2% of the mass content of this cluster comes from stars and $\sim$ 10% is due to interstellar gas [Ryd03]. The remaining fraction of mass comes from the vast amounts of dark matter present in the Coma cluster, as well as in all clusters of galaxies.

Another important evidence for the existence of dark matter can be found in the flat galactic velocity profile at large radii. The greatest contribution to this field came from Vera Rubin (Figure 2.1 on the right) that systematically analysed the velocity curves of several galaxies

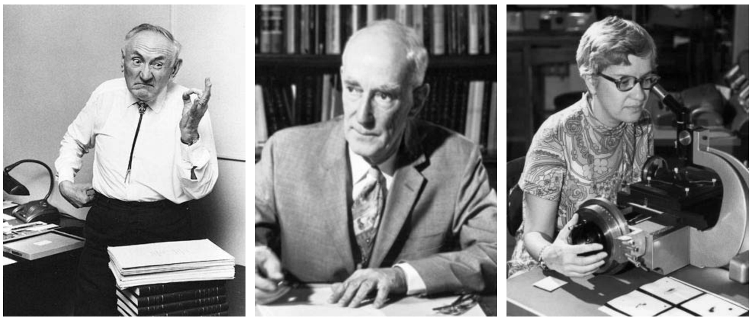

Figure 2.1: A grumpy Fritz Zwicky on the left, Jan Oort in the middle and Vera Rubin on the right. The three most influential characters in the "missing mass" odyssey.

and found that all behaved in disagreement with Newtonian dynamics. Rubin observed that the velocity of stars and gas clouds remained approximately constant at large radii, contrary to what would be expected from the gravitational influence of the visible matter present (as seen in Figure 2.2). The high velocities observed at larger radii should tear the galaxies apart, as these fast objects would surpass the escape velocity of these galaxies considering only the contribution of the mass from the luminous matter.

As the distance to the center of a galaxy increases, the velocity of an object is expected to behave as in Newton's law of gravitation (Eq. 2.5).

$$v(r) = \sqrt{\frac{GM(r)}{r}} \tag{2.5}$$

where $M(r)$ is the mass of the galaxy contained inside the radial distance r. For large radii, considering that most of the mass of a galaxy is concentrated in the center region (bulge), the velocity should follow $v(r) \propto r^{-1/2}$. This means that stars and gas further away from the center of the galaxy should move slower than those closer to the bulge mass – similarly to the behaviour of the planets of our solar system, that move slower for increasing distances to the Sun.

By measuring the redshift of the 21 cm emission line of hydrogen (the largest constituent of interstellar gas) as a function of radial distance to the galactic center, a rotation curve (as the one presented in Figure 2.2 for the NGC3198 spiral galaxy) is obtained.

This flat rotation curve implies that mass in the galaxy, rather than falling exponentially with the radial distance, has a proportional behaviour with the distance to the center of the system – as is evident in Eq. 2.5 if $v(r)$ becomes constant, implying $M(r) \propto r$. The presence of a massive dark matter halo that reaches far beyond the galactic luminous disk explains the observed behaviour, present in nearly all galaxies observed. From Figure 2.2 it is clear that the radial velocity becomes nearly constant at $\sim$ 150 km s^{-1} beyond $\sim$ 6 kpc. The contributions from the disk of stars and gas and from the dark matter halo that best fit the observable velocity profile are also included in Figure 2.2. To obtain a nearly flat curve, the halo mass distribution must increase with the radial distance, and the size of the dark matter halo is expected to be $\mathcal{O}(10)$ times larger than the diameter of the galactic disk. On our Milky Way galaxy this halo

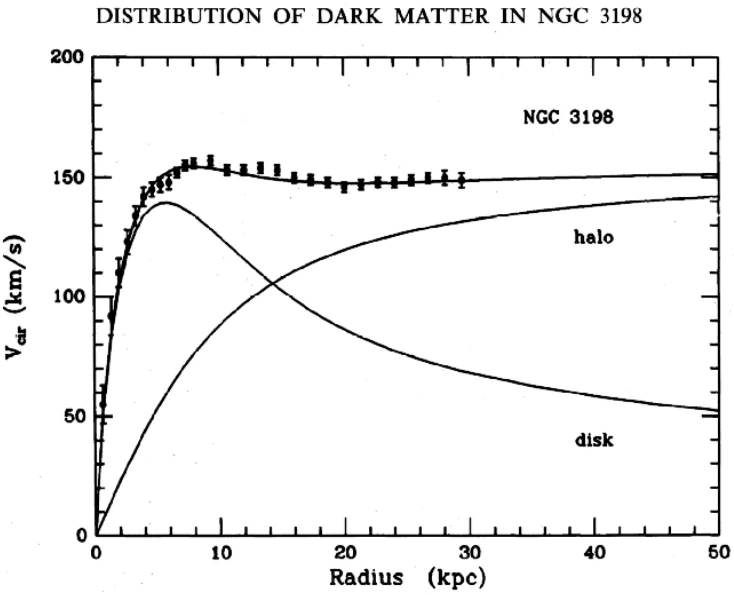

Figure 2.2: Rotation curve of the galaxy NGC3198, obtained by measuring the redshift of the 21 cm emission line of neutral hydrogen gas. The upper curve represents the best fit of the velocities to the data obtained, while the curves marked with “halo” and “disk” represent the mass density contribution of the dark matter halo and galactic disk (stars, gas and dust), respectively, whose sum would result in the observed flat velocity profile. Picture taken from [vBBS85].

is expected to compose $\sim$ 88.5% of the mass of the galaxy [KSLB14].

Further evidences of a non interacting dark matter component of our Universe are found in CMB anisotropies, large-scale structure formation, Big Bang nucleosynthesis and gravitational lensing, explained in detail in Section 2.2.

2.1 The ΛCDM model of the Universe

The history of our Universe since the time of inflation can be modeled using the cosmological constant Λ and a non-baryonic, non-relativistic (cold) dark matter component (CDM) [B$^+$12b].

By measuring the redshift (z) of several galaxies, Edwin Hubble observed that almost all of them were moving away from each other. The larger the distance to the galaxy observed, the larger the redshift measured (proxy to the velocity of the moving galaxy). Hubble had discovered the expansion of the Universe.

$$cz = H_0 r \tag{2.6}$$

In Eq. 2.6, the parameter H_0 is the Hubble constant and represents the rate of expansion of the Universe at the current time t_0.

The *Cosmological Principle* states that the Universe looks isotropic and homogeneous [B$^+$12b]. The expansion of the Universe can be modeled using a scale factor $a(t)$ that represents the size of the Universe at the time t (cosmic scale factor), and the Hubble parameter $H(t)$, that represents the rate of expansion of the Universe at time t, can be defined as in Eq. 2.7.

$$H(t) = \frac{\dot{a}(t)}{a(t)} \tag{2.7}$$

By definition, the cosmic scale factor is considered to be $a(t = t_0) = 1$ at the current time t_0, defining $H(t = t_0) = H_0$.

The Friedmann equations relate the parameter $a(t)$ with the energy density $\epsilon(t)$, curvature parameter κ and pressure $p(t)$ summed for all components of the Universe, and are used to describe the expansion of the Universe assuming the *Cosmological Principle* to be true [B$^+$12b, Fah14]. The two independent Eqs. (2.8 and 2.9) are obtained directly from the field equations of General Relativity.

$$\left(\frac{\dot{a}}{a}\right)^2 = H^2 = \frac{8\pi G}{3c^2}\epsilon - \frac{\kappa c^2}{R_0 a^2} + \frac{\Lambda}{3} \tag{2.8}$$

$$\frac{\ddot{a}}{a} = -\frac{4\pi G}{3c^2}(\epsilon + 3p) + \frac{\Lambda}{3} \tag{2.9}$$

The first equation provides the essential components to relate the measured expansion rate of the Universe with its energy content, provided by ϵ, and the curvature of the Universe, defined by the curvature parameter κ and the curvature radius R_0 if $\kappa \neq 0$.

The cosmological constant Λ was first introduced by Albert Einstein in 1915 in order to obtain a static Universe ($\ddot{a} = 0$) and was thus set to $\Lambda = 4\pi G\epsilon/c^2$ to “fight off gravity” [B$^+$12b]. As far as it was known at the time General Relativity was proposed, the Universe was static, otherwise gravity would have collapsed matter over the time and our Universe would not exist. This *ad hoc* solution provided by Einstein was later justified as being the work of the intrinsic energy of space, a negative pressure that countered the attractive behaviour of gravity. His “biggest blunder”, as Einstein called it, turned out to be something more: the vacuum energy density, also known as Dark Energy. Einstein was not wrong in modeling the Universe to what was best known at the time, the “biggest blunder” was in fact that he had not predicted that the Universe could be dynamical. Later on, Friedmann, Lemaitre, Robertson and Walker [Fri99a, Fri99b, Rob35, Lem31] found the solutions that Einstein failed to acknowledge.

The contribution of the cosmological constant on Eq. 2.8 can be included in the energy density parameter, and so ϵ accounts for all contributions to the energy content of the Universe.

A flat Universe is defined by a curvature parameter $\kappa = 0$, while an open Universe (hyperbolic space-time) and a closed Universe (spherical) are defined by $\kappa = -1$ and $\kappa = 1$, respectively [Fah14]. The critical energy density of the Universe, ϵ_c, is defined considering a flat geometry in Eq. 2.8.

$$\epsilon_c(t) = \frac{3c^2}{8\pi G} H(t)^2 \tag{2.10}$$

The density parameter $\Omega(t)$ is then defined as:

$$\Omega(t) = \frac{\epsilon(t)}{\epsilon_c(t)} \tag{2.11}$$

This dimensionless quantity appears often in the form Ωh^2, where $h = H_0/(100 \text{ km s}^{-1} \text{ Mpc}^{-1})$ is the dimensionless Hubble parameter.

The first Friedmann equation can be represented by the different contributions to the density parameter Ω, yielding:

$$\frac{H^2}{H_0^2} = \frac{\Omega_r}{a^4} + \frac{\Omega_m}{a^3} + \frac{\Omega_\kappa}{a^2} + \Omega_\Lambda \tag{2.12}$$

where Ω_r, Ω_m, Ω_κ and Ω_Λ represent the energy density parameters for radiation, matter, the curvature of space and the vacuum energy density, at the current time, respectively. $\epsilon_c(t_0)$ represents the critical energy density. As the cosmic scale factor is set to 1 at the current time, these contributions sum up to $\Omega_r + \Omega_m + \Omega_\kappa + \Omega_\Lambda = 1$. The denominator factor in each density parameter contribution is related to different equations of state for matter and radiation[1]. By analysing Eq. 2.8, for the current time, it becomes apparent that the curvature contribution term Ω_κ can be related to the current energy density parameter as:

$$\Omega_\kappa = 1 - \Omega_0 \tag{2.13}$$

This means that the parameter Ω also provides a measurement of the curvature of space-time: A Universe with $\Omega = 1$ is flat, $\Omega > 1$ results in a closed Universe and $\Omega < 1$ results in an open Universe.

Today we live in a matter-dominated Universe, meaning that $\Omega_r \sim 0$. If the Universe is flat as it appears [PA$^+$15], then $\Omega_\kappa \sim 0$, meaning that the remaining contributions (matter and dark energy) sum up to 1. The energy density contributions from matter and dark energy can also be used to measure the deceleration parameter q_0, derived from the second Friedmann equation (Eq. 2.9) and defined as in Eq. 2.14.

---

[1] The evolution of ϵ for each component depends on the scale factor a as stated by the fluid equation $\dot{\epsilon} + 3(\epsilon + w\epsilon)\frac{\dot{a}}{a} = 0$ considering $p = w\epsilon$, yielding $\epsilon_w(a) = \epsilon_{w,0} a^{-3(1+w)}$, where $w = 0$ represents a non-relativistic dispersion and $w = 1/3$ a fully relativistic scenario [Fah14]. As dark energy contributes with a negative pressure, $w < 0$. The most accepted value is $w_\Lambda = -1$ [PA$^+$14].

$$\begin{aligned} q_0 &= -\left(\frac{\ddot{a}}{aH^2}\right)_{t=t_0} = \frac{1}{2}\sum_w \Omega_w(1+3w) \\ &= \Omega_r + \frac{1}{2}\Omega_m - \Omega_\Lambda \end{aligned} \tag{2.14}$$

This parameter uses the measured values of the density parameters to determine if the expansion of the Universe is slowing down ($q_0 > 0$) or speeding up ($q_0 < 0$).

The current best estimate to the values of the ΛCDM model are presented by the Planck Collaboration [PA$^+$15] and are summarized in Table 2.1. The current best estimate of the mass-energy content of the Universe is schematically represented in Figure 2.3.

Table 2.1: Latest results from the Planck Collaboration [PA$^+$15] for the cosmological parameters of the ΛCDM model. The values presented have 68% error bands and combine data from WMAP+JLA+BAO.

Parameter	Symbol	Value
Hubble constant [km s^{-1} Mpc^{-1}]	H_0	67.74 ± 0.46
Baryon energy density	$\Omega_{b,0}h^2$	0.02230 ± 0.00014
Cold Dark Matter energy density	$\Omega_{DM,0}h^2$	0.1188 ± 0.0010
Total matter energy density	$\Omega_{m,0}$	0.3089 ± 0.0062
Dark energy density	Ω_Λ	0.6911 ± 0.0062
Curvature	$\Omega_{\kappa,0}$	$0.0008^{+0.0040}_{-0.0039}$
Sum of neutrino masses [eV]	$\sum m_\nu$	< 0.194
Age of the Universe [Gy]		13.799 ± 0.021

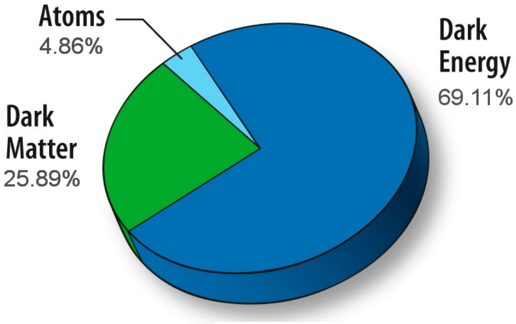

Figure 2.3: Planck Cosmic Recipe for our Universe.

2.2 The evidence of Dark Matter

2.2.1 The dynamics of Galaxies and Clusters

As discussed in the beginning of this chapter, a strong evidence supporting dark matter can be found in the dynamical behaviour of galaxies and intergalactic dust in clusters of galaxies, and also in the motion of stars and gas in individual galaxies. Like in the work of Fritz Zwicky and Vera Rubin [Zwi33, Rub83], the unobserved additional mass from dark matter becomes noticeable by the gravitational influence it has in the visible matter. This influence allows the dark matter content of a given cosmological system to be determined.

The analysis of clusters of galaxies, much like the study of the Coma cluster by Zwicky, provides scientific evidence that cosmic structures are moulded by dark matter and that this component is very common in our Universe today.

Galaxy rotation curves like the one presented in Figure 2.2 are in agreement with a dark matter halo surrounding the galactic disk, but could also be explained with modified gravity, as will be explained in further detail in Section 2.3.5.

It is also important to mention that a self-gravitating, non-interacting "ideal gas" of massive particles follows a Maxwell-Boltzmann velocity distribution that automatically results in a density $\rho(r) \propto r^{-2}$ and thus $M(r) \propto r$, as expected for a galactic halo that contributes to a flat rotation curve, observed in most young galaxies analysed [Ryd03].

A recent study of the Coma cluster resulted in the discovery of more than 800 dark galaxies [KYYK15]. These dim, diffuse galaxies have an abnormal amount of dark matter when compared to their stellar content - around 98% of the mass of these galaxies is due to dark matter. The low barionic content of dark galaxies, below the cosmic average, means that some process removed the gas in the galaxies and disabled star formation. It becomes apparent from these findings that dark matter structures the size of the Milky Way are more common than previously thought.

2.2.2 Cosmic Microwave Background

The Cosmic Microwave Background (CMB) is a thermal radiation that isotropically fills the Universe. It exhibits a blackbody spectrum with a temperature of 2.722 ± 0.027 K [PA$^+$15]. In 1965, the radio-astronomers Arno Penzias and Robert Wilson of the Bell Telephone Laboratories noticed a persistent noise in the Holmdel Horn Antenna while studying satellite communications [PW65]. Some previous studies had predicted that the Universe would be filled with a blackbody radiation remnant from the Big Bang [Gam48, AH48]. The discovery of the CMB was the major evidence in favour of the Big Bang theory [B$^+$12b].

The cosmic background is the result of the decoupling of photons trapped in the photon-baryon-electron plasma in the infant Universe. Temperatures in the plasma were initially high and photodissociation suppressed the combination of protons and electrons to form neutral hydrogen atoms. With the adiabatic expansion of the Universe, the temperatures began to decrease, and at some point were low enough for hydrogen atoms to form and the plasma became transparent to the trapped photons, that have been travelling to this day. This moment is called the "time of last scattering", and occurred at a redshift of $z \approx 1100$ (around 361 thousand years after the Big Bang) [PA$^+$15]. The wavelength of the primordial photons was stretched due to the expansion of the Universe, and at the present has a low-energy microwave wavelength. Information about the state of the Universe at the time of decoupling including a map of the denser and hotter regions remained imprinted in this "baby cry of the Universe".

The denser regions of the primordial plasma were hotter because photons would interact strongly with electrons via Thompson scattering [Viv10]. As the Universe cooled, electrons and protons formed neutral hydrogen, and as photons do not interact as strongly with neutral matter as with fully ionized plasma, the mean free path of these thermal photons became of order of the size of the Universe. The CMB thermal anisotropies arise from the density (and consequently temperature) fluctuations in the photon-baryon plasma at the time of last scattering, becoming imprinted in the emitted photons – regions with higher temperatures had more energetic photons while cooler regions resulted in lower-energy photon emissions – resulting in a "photograph" of the state of the Universe at a very young age.

Figure 2.4 represents the sky map of the CMB as seen from the latest data of Planck [PA$^+$15]. The CMB is smooth across the sky, with temperature fluctuations of only ±250 μK. These fluctuations are related to the temperature and density distribution of the Universe at the time of last scattering.

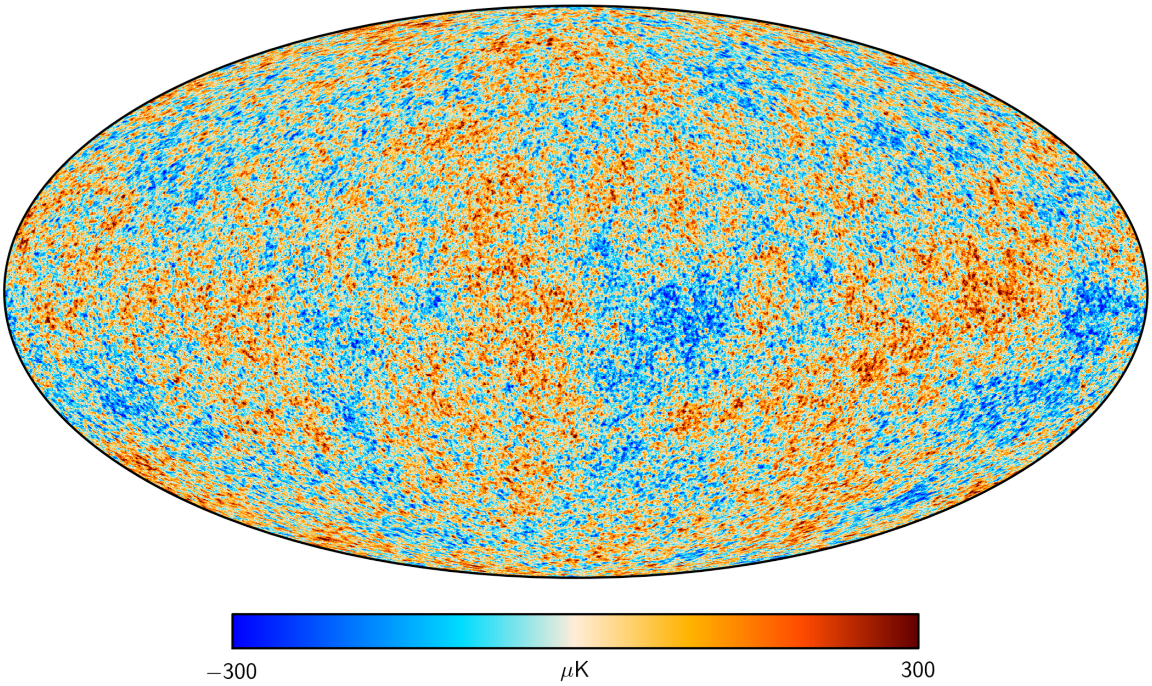

Figure 2.4: Mollweide projection of the CMB seen by the Planck satellite with the 2015 data, with monopole (mean temperature) and dipole (Doppler shift) contributions removed. Figure taken from [Col15b].

The resolution of the CMB map obtained with Planck increased significantly relatively to previous CMB experiments, allowing for a more detailed description of the conditions in the early Universe than ever before. Figure 2.5 demonstrates the resolution improvement in the CMB mapping from the Wilkinson Microwave Anisotropy Probe (WMAP) of NASA to the Planck satellite.

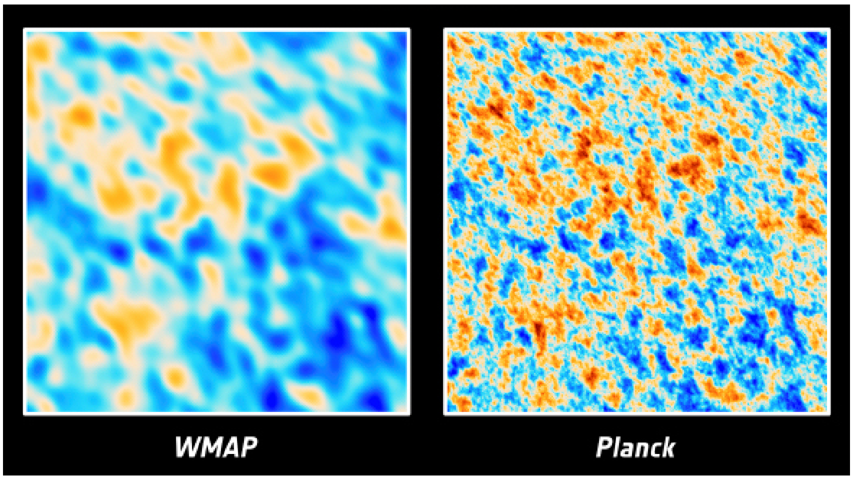

Figure 2.5: Comparison between the CMB field as seen from WMAP (left) and Planck (right). With greater resolution and sensitivity over nine frequency channels, Planck has delivered the most precise image so far of the Cosmic Microwave Background. Image adapted from [Col15b].

Figure 2.6 shows the amazing detail of Planck, with a reconstructed image of the Orion Molecular Cloud – a large region of star formation about only 1300 ly away from the Sun. The polarization measurements of Planck allow mapping of the Galactic magnetic fields.

Measurement of the temperature power spectrum

The temperature fluctuations in the early Universe were dependent of several cosmological parameters, as matter density, vacuum energy density, baryon-to-photon ratio and the baryon fraction in total matter. It is expected that these parameters influence the shape of the CMB angular power spectrum by changing the angular separation and intensity of the thermal fluctuations. Therefore the CMB anisotropies encode substantial information of the early stages of the Universe and the cosmological parameters that led the Universe from the hot plasma of matter and radiation to its current state. Usually a multipolar analysis is used to separate the angular scales (or multipole moments) using a spherical harmonic expansion like the one in Eq. 2.15 [Fah14]

$$T(\theta,\phi)=\sum_{l}^{\infty}\sum_{m=-l}^{l} a_{lm}Y_{lm}(\theta,\phi) \tag{2.15}$$

where l is the multipole number and m the multipole projection number. The monopole ($l=0$)

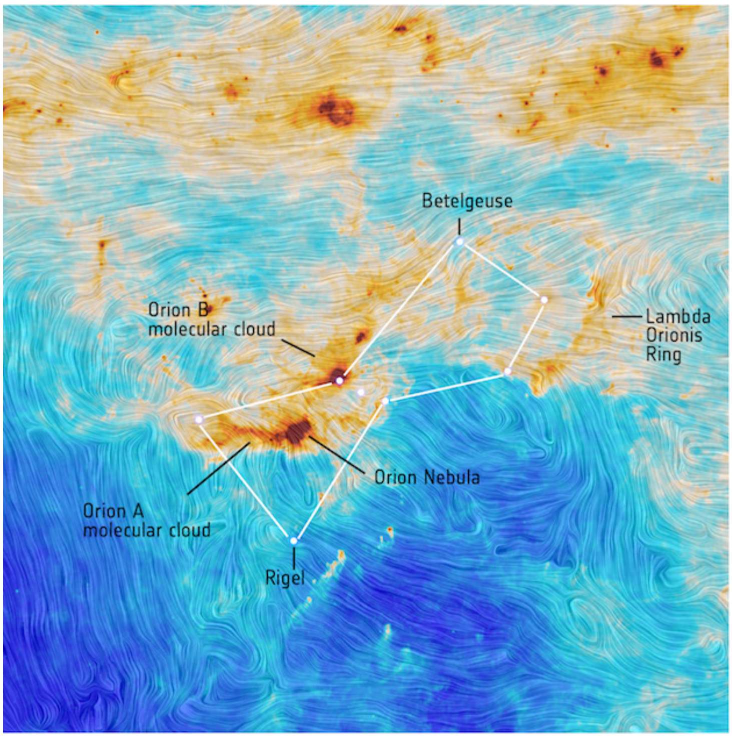

Figure 2.6: Detail image of star formation and magnetic turbulence in the Orion Molecular Cloud, as seen by Planck in microwave and sub-millimetre wavelength. The texture in the image represents the Galactic magnetic field lines, while color represents thermal variations. The contour of the Orion constellation, main stars and the nebula are marked. Image taken from [Col15b].

is the mean temperature of the CMB, with value 2.722±0.027 K [PA$^+$15]. The dipole component of the CMB map ($l = 1$) is the strongest anisotropy measured and results of the relative motion of the Sun[2] towards the invariant CMB field, which results in a Doppler shift of the microwave radiation with a 90° angular distribution and amplitude 3.555 ± 0.008 mK [B$^+$12b]. In order to reveal the underlying anisotropies arising at higher multipoles, the mean temperature from the monopole (first term of Eq. 2.16) and the Doppler shift from the dipole (second term of Eq. 2.16) need to be removed.

$$T(\theta,\phi) = \langle T_{CMB} \rangle + (3.555 \pm 0.008 \text{ mK}) \cos\theta + \sum_{l=2}^{\infty} \sum_{m=-l}^{l} a_{lm} Y_{lm}(\theta,\phi) \tag{2.16}$$

The vast majority of the cosmological information is present in the temperature two point correlation function, that accounts for the temperature fluctuations separated by an angular distance regardless of the direction. The spherical harmonics expansion of the CMB field can then be expressed in terms of Legendre polynomials $P_l(\cos\theta)$ and the coefficients C_l [Fah14].

---

[2] The motion of the Sun around the center of the Milky Way plus the motion of the galaxy in the Local Group plus the motion of the Local Group towards the constellation of Hydra.

$$C(\theta) = \langle \frac{\Delta T(\theta,\phi)}{T} \frac{\Delta T(\theta,\phi)}{T} \rangle \tag{2.17}$$

$$C(\theta) = \frac{1}{2\pi} \sum_{l=2}^{\infty} \left(l + \frac{1}{2} \right) C_l P_l(\cos\theta) \tag{2.18}$$

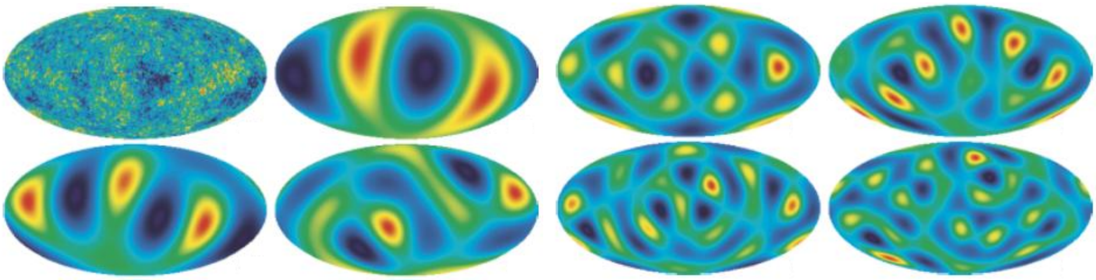

Figure 2.7: Representation of the multipole analysis of the CMB data. The multiple harmonics contribute differently to the thermal anisotropies. The analysis is made from lower multipoles excluding $l = 0; 1$ and up to higher multipoles of order $l \approx 1000$. Higher multipole number l represents smaller angular distances between fluctuations. The first image is a representation of the CMB map, while the subsequent images are representations of the correlation function in therms of multipole moments, from $l = 1$ (dipole) to $l = 7$. Figures from [Col15b].

The correlation function presented in Eq. 2.18 can then be broken into multipole moments C_l, and the correlation function is represented as a power spectrum given by Eq. 2.19, and is represented in terms of either l or θ.

$$D_l \equiv \frac{l(l+1)}{2\pi} C_l \tag{2.19}$$

The temperature power spectrum obtained in the analysis of the CMB anisotropy data from Planck 2015 results is represented in Figure 2.8.

The peaks in the power spectrum arise from acoustic oscillations of density in the primordial plasma at the time of last scattering. The first large peak at $l \approx 200$ (or $\theta \approx 1\,\mathrm{deg}$) corresponds to the angular size of the Hubble distance at the time of last scattering, as seen from the Earth. The gravitational potential wells that would trap matter in the acoustic wave modes would have the size of the Hubble distance scale – the distance a photon could travel in the age of the Universe. The angular size of this distance would be $\theta_H(z) = c/(H(z)d_A(z))$, for $z = 1100$ that returns $\theta_H = 0.2$ Mpc/(14000 Mpc / 1100) $\approx 1°$. The relative position of this peak is sensitive to the expansion history of the Universe, dependent of the dark energy density and curvature of the Universe, as a curved space would return different angular distances of distant objects, as it can be seen in Figure 2.9 (first two panels). The value obtained by Planck is consistent with a flat Universe, with $\Omega = 1$.

The amplitudes of the first peaks, corresponding to the amount of gravitational compression of the primordial plasma, are sensitive to the baryonic content of the plasma as seen in Figure 2.9 – more baryonic mass would increase the inertia of the oscillating fluid and alter the vibration

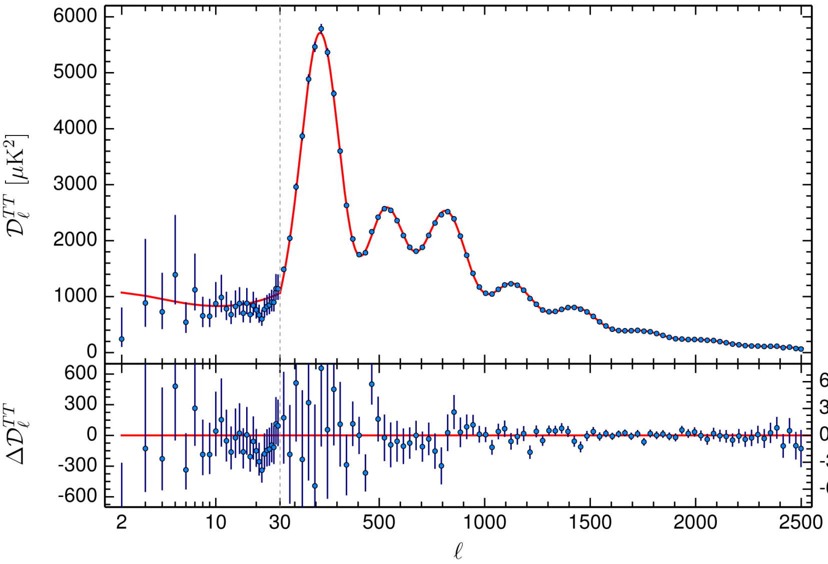

Figure 2.8: Planck Angular Power Spectrum of the CMB, obtained using multipolar analysis to the CMB map. The red line represents the theoretical model prediction with values of the ΛCDM model that best fit the data. The first acoustic peak is clearly visible at $l \approx 200$, followed by the secondary peaks and damping tail, at higher l. A detailed description of the peaks is presented in the main text. Figure from [Col15b].

modes, non-baryonic dark matter is not accounted because it does not interact with the photons. Fitting the relative size of the first, second and third peaks of the spectrum yield the baryonic density parameter Ω_b [Hu08].

As the driving force of the acoustic oscillations is gravity, fitting the overall amplitude of the temperature power spectrum returns the total matter density parameter Ω_m. As the parameters Ω_b and Ω_m are determined independently, the amount of non-baryonic matter in the Universe can be obtained directly from the analysis of the CMB.

The dark energy density can be indirectly obtained from $\Omega_\Lambda = \Omega - \Omega_m$, or directly by analysing the redshifting or blueshifting of photons as they cross the gravitational wells of the density waves at the time of last scattering, that depend on the expansion of the Universe at the time the photons were travelling in the well [HSS97]. As photons enter the high density regions, they get blueshifted, but when they leave these dense regions, due to the expansion of the Universe, the amount of redshift experienced does not equal the amount of blueshift the photons suffered on the way in. The temperature fluctuations created by the change in the gravitational potentials is called the Integrated Sachs-Wolfe (ISW) effect [HSS97]. This effect can be measured at high angular scales in the power spectrum, being a measurement of the total matter density and the vacuum energy density parameters.

The CMB allows to analyse the ΛCDM model in detail, being sensitive to most of the model parameters, such as Ω_m, Ω_b, Ω_Λ, Ω_k and $\Omega = \Omega_r + \Omega_m + \Omega_\Lambda + \Omega_k$. A summary of the results from the Planck 2015 CMB data analysis [PA$^+$15] for the cosmological parameters is presented in Table 2.1.

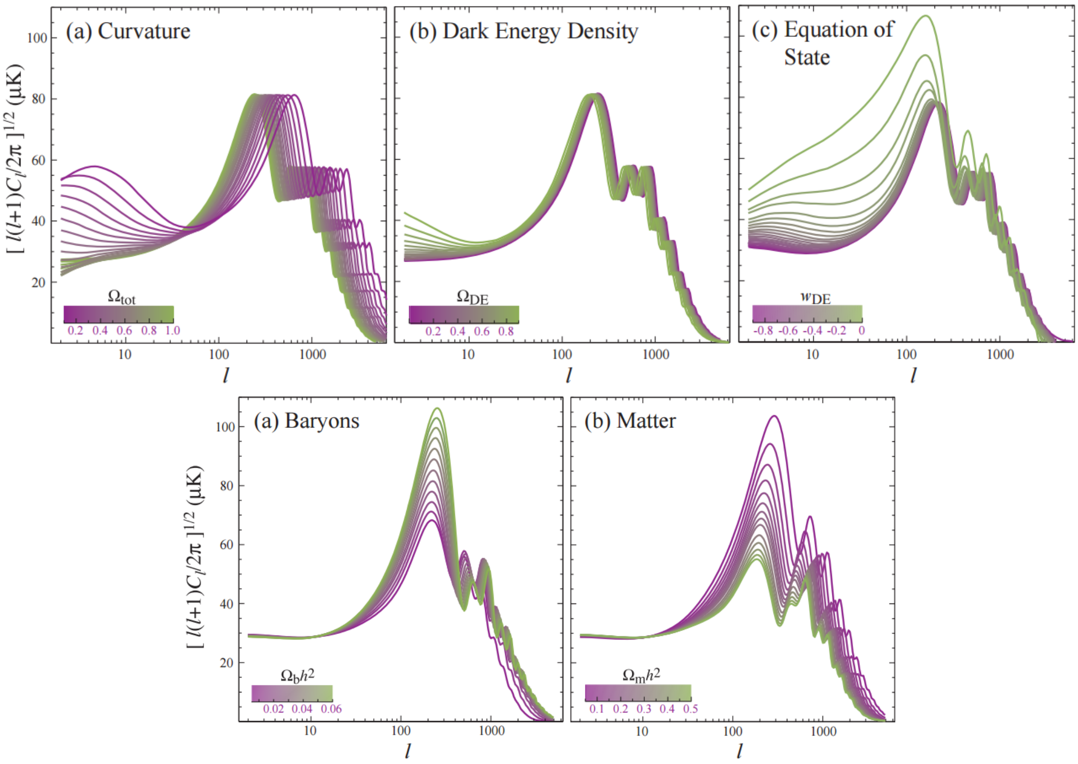

Figure 2.9: CMB Angular Power Spectrum profile with the variation of different cosmological parameters. Considering the ΛCMB model, the cosmological parameters can be determined using a profile likelihood analysis. Figure reconstructed from [Hu08].

2.2.3 Baryon Acoustic Oscillations

Fluctuations in the matter density of the infant Universe seeded the formation of structures observable today, such as galaxy clusters and superclusters. Baryon Acoustic Oscillations are acoustic waves created in denser regions (anisotropies) of the hot primordial plasma that favoured the formation of dense structures as the Universe expanded [SZ70].

The denser regions gravitationally attract more matter, but as photons are still tightly coupled to matter, the heat generated by these interactions generates outward pressure. Oscillations arise from the counteracting forces of gravity and radiation pressure [Fah14]. As a denser region contains baryons, dark matter and photons, the outward pressure results in a baryon-photon acoustic wave moving away from the density center, while the gravitationally bound dark matter with no other interaction mechanism with the baryon-photon plasma remains at the center of the density perturbation. Baryons and photons move outwards together with the wave, in a density shell, until temperatures become low enough for these particles to decouple, and the photons diffuse away unobstructed. This decoupling relieves the pressure of the acoustic wave, leaving a shell of baryonic material at a defined radius, called the sound horizon [ESW07].

Figure 2.10 represents the evolution of the oscillations before and after photon decoupling from baryons (center left panel). As decoupled photons disperse, the baryonic acoustic wave stalls

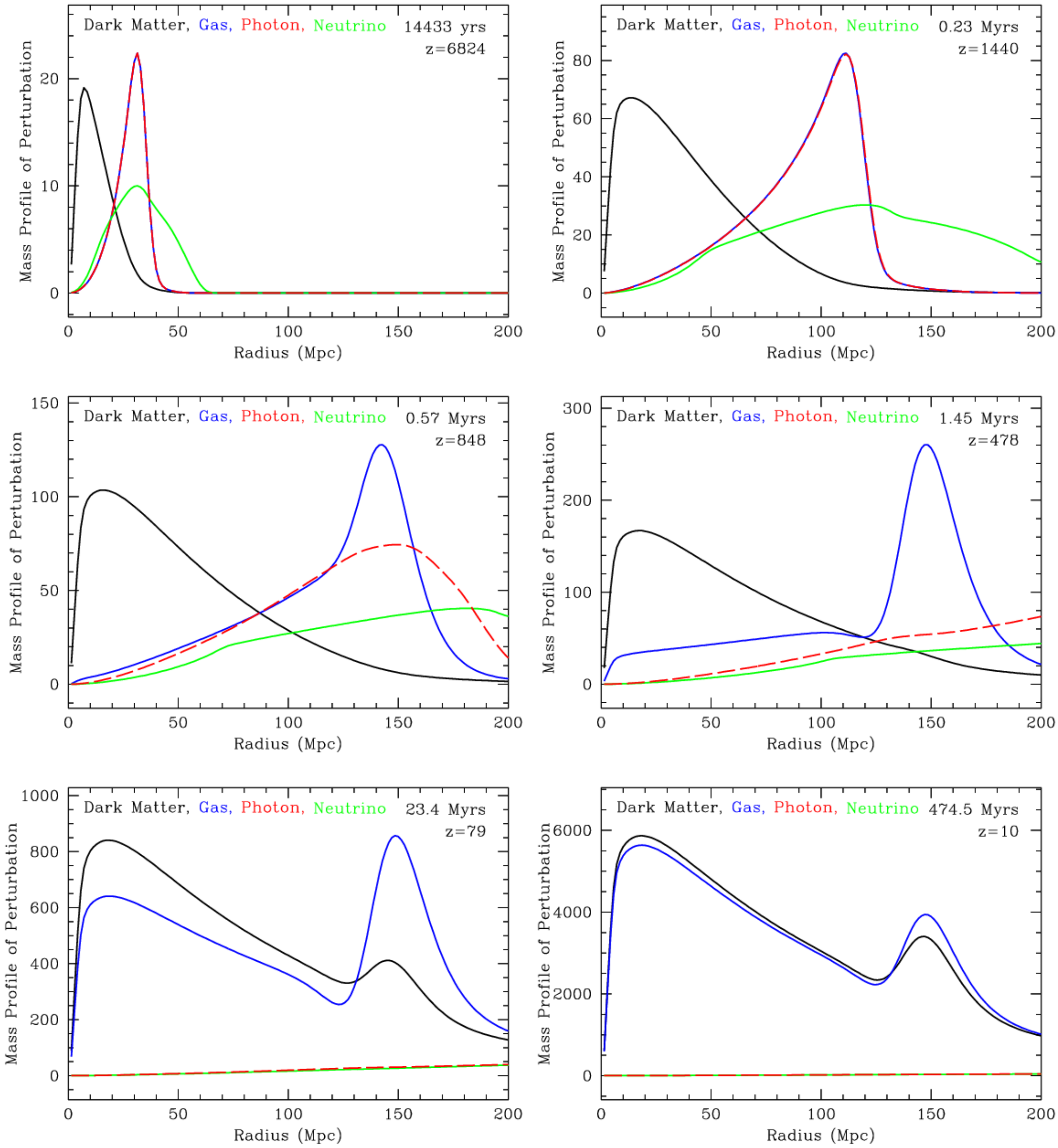

Figure 2.10: Evolution of an acoustic wave in the primordial plasma, showing the different species present and their behaviour (mass distribution) over different moments: baryons (named "gas", blue), dark matter (black), photons (red), and neutrinos (green). The center-left panel represents the decoupling of photons and baryons, where photons disperse and the baryonic peak stalls. Dark matter and baryonic matter then rearrange due to gravity, resulting in the merging of the respective curves as portrayed in the last figure. Figures taken from [ESW07].

behind and an excess of baryonic matter is left at a defined distance – the sound horizon – from the density fluctuation. On the course of time, dark matter merges with baryonic matter due to gravitational influences and the mass distribution profiles become similar [ESW07].

The analysis of acoustic oscillations is done using a distance correlation function $\xi(r)r^2$ that represents the average amount of matter at any distance r, convoluted with all points in space, returning a frequency spectrum of distances between observable mass distributions [Fah14].

It is expected that a larger number of massive structures are found separated by a distance equal to the sound horizon than by smaller length scales. This effect cannot be observed directly, as the density fluctuations on the primordial plasma were randomly distributed and each fluctuation resulted in a concentric shell of baryonic matter, rendering the effect diffuse. However, analysing the separation of a great number of galaxies statistically, or measuring the abundance of intergalactic gas by redshifted Lyman-α emissions [SIK+13], it is possible to detect the sound horizon length scale, as it is demonstrated in Figure 2.11. In this Figure, taken from analysing the Lyman-α forest[3] to obtain the spacial distribution of intergalactic neutral hydrogen gas, the baryonic acoustic peak at $100 - 130\ h^{-1}$ Mpc scale is clearly visible.

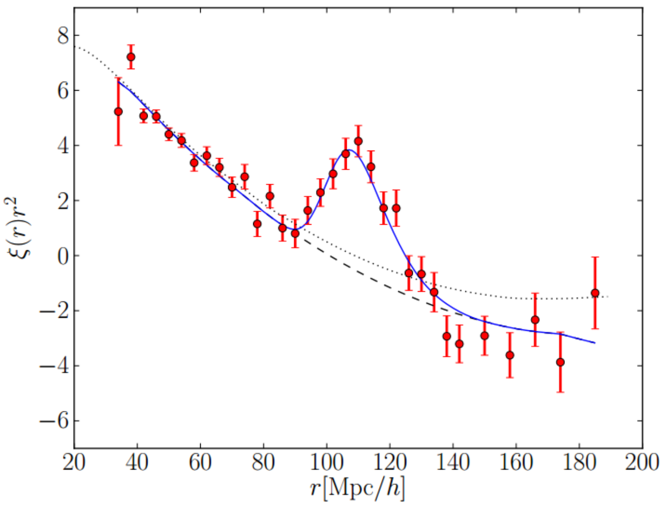

Figure 2.11: Baryon acoustic peak measured from the Lyman-α forest, with redshift-space distortions corrected. The peak in the correlation function is clearly visible at length scale $r = 100 - 130\ h^{-1}$ Mpc with a 4σ significance. Figure taken from [SIK+13].

Baryon acoustic oscillations are one type of *standard ruler*, an object with a known size in space that can be used to measure distances. BAO can also constrain cosmological parameters, as the length-scale of the baryon-acoustic peak is sensitive to the acceleration rate of the Universe and the baryon fraction of the total matter content of the Universe. The best values for the fraction of baryonic matter in the total matter content are $\Omega_b/\Omega_m \approx 0.2115$ [T+06], consistent with data from CMB and BBN data, and proving that only a large fraction of non-baryonic matter can justify the observations of large-scale structure present today.

---

[3] The Lyman-α forest is the term used to describe the spectrum of neutral hydrogen gas illuminated from a distant source, like a quasar. The spectrum presents several peaks relative to the Lyman-α line of hydrogen and deuterium being redshifted. This allows the mapping of the intergalactic gas.

2.2.4 Big Bang Nucleosynthesis

The relative abundance of light elements we see today (H, D, ^{3}He, ^{4}He, ^{6}Li and ^{7}Li) is the result of a series of processes that occurred in a short time window just seconds after the Big Bang. This production of light elements, called Big Bang Nucleosinthesis (BBN), started when the temperature of the primordial proton-neutron plasma dropped below $T = \mathcal{O}(10\ \text{MeV})$ allowing free protons and neutrons to undergo nuclear fusion and form light nuclei [B$^+$12b]. Higher temperatures would result in the photodissociation of nuclei from MeV photons and BBN could not proceed. Nucleosynthesis was a race against time, being essentially over in just a few minutes after the Big Bang, when temperatures dropped below $T = \mathcal{O}(\text{keV})$, rendering fusion inefficient.

Neutrons and protons are in equilibrium through the reactions presented in Eqs. 2.20 to 2.22 [Fah14]. The neutron to proton relative number density, $f = n_n/n_p$, at $t \sim 1$ s is approximately 1 and begins to decrease rapidly, stabilizing with a value estimated at $f = 0.2$ when the neutrino interaction rate becomes comparable to the Hubble parameter, “freezing” out the relative abundance of protons and neutrons.

$$n + \nu_e \rightleftharpoons p + e^- \tag{2.20}$$

$$n + e^+ \rightleftharpoons p + \bar{\nu}_e \tag{2.21}$$

$$n \rightleftharpoons p + e^- + \bar{\nu}_e \tag{2.22}$$

As neutrons naturally decay with a 885 s half-life [End00], the fraction of neutrons to protons decreases before deuterium begins to form. At this time, around 1 neutron to 7 protons are available for fusion into deuterium.

Deuterium

The first and most important step in primordial nucleosynthesis is deuterium, D, which is obtained by the fusion of one proton with one neutron in the reaction described by Eq. 2.23 [Fah14].

$$p + n \rightleftharpoons D + \gamma \tag{2.23}$$

The left arrow in Eq. 2.23 represents the photodissociation of deuterium by high energy photons. As the creation of higher atomic mass nuclei is hindered by the available deuterium, only when a substantial fraction of neutrons are implemented as deuterium can the following nucleosynthesis steps occur. When temperatures reach the keV level, photodissociation no longer separates deuterium and nearly half the neutrons can be found bound to protons. The ratio D/H is sensitive to the baryon-to-photon ratio η, an important cosmological parameter that influences the early or late beginning of BBN [Fah14, B$^+$12b].

Helium

At $t \sim 200$ s, deuterium and free neutrons and protons are available in the dense plasma to begin building other nuclei, more precisely ^{3}He and ^{4}He. Only two-body reactions are relevant because of the low density of baryons, and these reactions occur rapidly until nearly all available neutrons are part of ^{4}He. The main reactions for generating helium nuclei are presented in Eqs. 2.24 to 2.30 [Fah14].

$$D \ + \ n \ \rightleftharpoons \ ^3He \ + \ \gamma \tag{2.24}$$

$$D \ + \ D \ \rightleftharpoons \ ^3He \ + \ p \tag{2.25}$$

$$D \ + \ D \ \rightleftharpoons \ ^4He \ + \ \gamma \tag{2.26}$$

$$^3He \ + \ n \ \rightleftharpoons \ ^4He \ + \ \gamma \tag{2.27}$$

$$^3He \ + \ D \ \rightleftharpoons \ ^4He \ + \ p \tag{2.28}$$

$$T \ + \ n \ \rightleftharpoons \ ^4He \ + \ \gamma \tag{2.29}$$

$$T \ + \ D \ \rightleftharpoons \ ^4He \ + \ p \tag{2.30}$$

In Eqs. 2.29 and 2.30, T stands for tritium, produced in small quantities by deuterium reactions.

Figure 2.12 displays the nuclear binding energy of common isotopes. The ^{4}He nucleus is strongly bonded, as it can be seen in the figure presented, meaning that as deuterium and ^{3}He begin to generate this nucleus the creation of nuclei heavier than helium is highly suppressed. As ^{4}He is not spent in significant amounts and the available ^{3}He ends up forming ^{4}He and heavier nuclei, the primordial fraction of ^{4}He, $Yp \approx 0.25$, remains almost unchanged at the current time, being used to calibrate the ratios of other nuclei ratios.

Beryllium and Lithium

The reactions responsible for creating ^{6}Li, ^{7}Li and ^{7}Be are presented in Eqs. 2.31 to 2.33 [Fah14].

$$^4He \ + \ D \ \rightleftharpoons \ ^6Li \ + \ \gamma \tag{2.31}$$

$$^4He \ + \ T \ \rightleftharpoons \ ^7Li \ + \ \gamma \tag{2.32}$$

$$^4He \ + \ ^3He \ \rightleftharpoons \ ^7Be \ + \ \gamma \tag{2.33}$$

No nucleus with $A = 8$ is stable, meaning that nuclei heavier than ^{7}Be are not produced in measurable quantities.

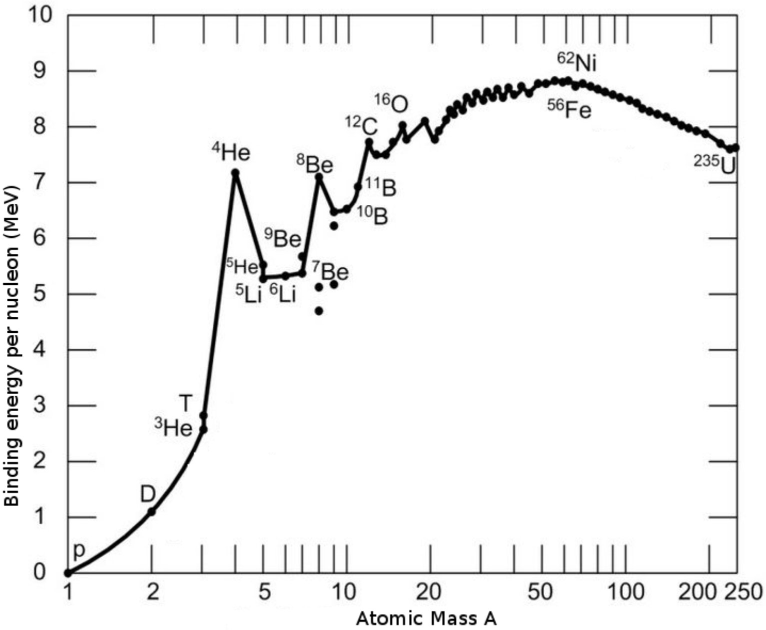

Figure 2.12: Nuclear binding energy per nucleon for several elements. ^{56}Fe is commonly considered as the most tightly bound nucleus, despite some authors considering ^{58}Fe and ^{62}Ni to be more strongly bound. Figure adapted from [Com].

Baryon Energy Density

The current estimates for the nuclei abundances yield $D/H = (3.02 \pm 0.23) \times 10^{-5}$, $^3He/H = (1.1 \pm 0.2) \times 10^{-5}$, $Y_p = 0.2534 \pm 0.0083$ and $^7Li/H = (1.58 \pm 0.31) \times 10^{-10}$ [Coc13]. In order to measure the relative abundance of primordial elements, areas with low stellar "contamination" need to be chosen to perform the measurements. The metallic[4] content of a star or neighbouring gas means that the primordial nuclei abundance is no longer maintained. Stars are efficient at dissociating deuterium, and in order to measure the D/H ratio, an intergalactic gas sample needs to be considered.

Knowing the relative abundance of the elements in the Universe makes possible, through BBN, to estimate the value of η. Figure 2.13 represents the abundances of the primordial nuclei species as function of the baryon-to-photon ratio η. Comparing the measured abundances with the expected from BBN, the value of η can be extracted, and the baryonic energy density parameter is calculated to be $\Omega_{b,0}h^2 = 0.021 \pm 0.002$.

---

[4] Metals in this context refers to any element with a mass number higher than ^{7}Be.

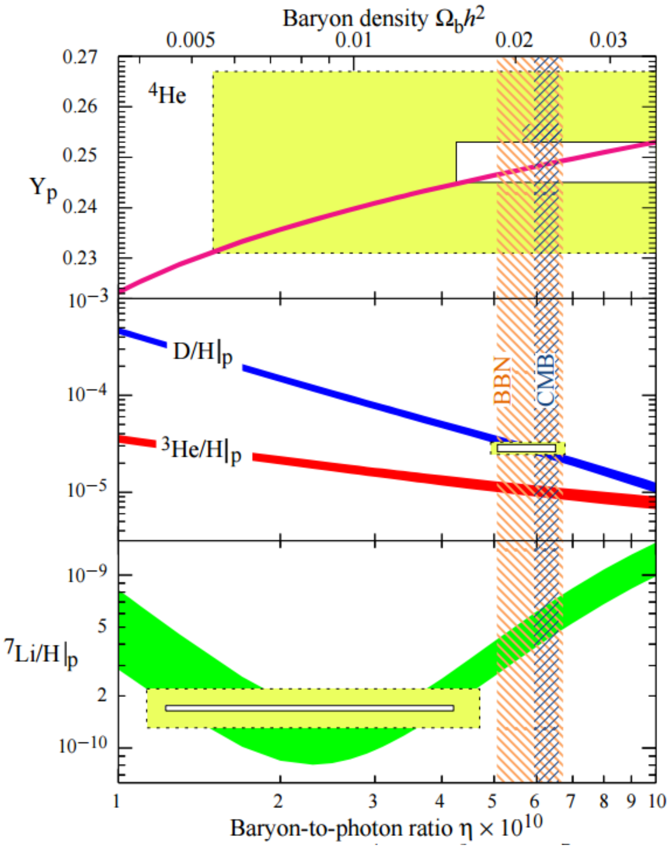

Figure 2.13: The abundances of ^{4}He, D, ^{3}He and ^{7}Li as a function of the baryon-to-photon ratio η, as predicted by BBN. Band width represents a 95% confidence limit and the boxes represent the abundances of the light elements observed in the Universe. The abundance of the light elements is normalized to the H abundance. ^{4}He abundance increases for higher η values because deuterium production would start earlier. Consequently, the relative abundances of ^{3}He and D decrease with η because of the anti-correlation of these nuclei with ^{4}He (Eqs. 2.26 and 2.28). The vertical lines represent the CMB cosmic baryon density measurements and BBN concordance range. Figure taken from [B$^+$12b].

2.2.5 Supernova Type Ia

The *Cepheid* variables are a type of stars that can be used as distance indicators up to 30 Mpc scale [F$^+$01]. These stars, with masses between $4-20\ M_\odot$, pulsate radially – they change in temperature and radius, producing variable luminous output whose frequency depends of the proprieties of the star [Rod57]. The variation in size and luminosity is due to the compensation of the radiation pressure with gravitational pressure around a stable value, with a period of several days to months[5]. By knowing the frequency at which the star varies the luminous output, establishing the star maximum light output (absolute magnitude) is possible. The *RR Lyrae* variables are another type of pulsating stars that can be used as distance indicators but, unlike *Cepheid* variables, these star have masses typically around half the mass of our Sun.

---

[5] The star contracts (minimum luminosity) due to its self-gravity and the abundant ionized helium becomes double-ionized, increasing the opacity of the star. As the internal pressure increases, the star expands and radiates significantly (maximum luminosity). When gravitational forces overcome the internal pressure forces the star contracts again and the cycle continues.

Both *Cepheid* and *Lyrae* variables are used as standard candles – objects with a known luminosity output that allow their astronomical distance to be known by measuring the apparent magnitude m, knowing the absolute magnitude M beforehand (see Eq. 2.34). But these star are relatively dim and a different *standard candle* is required for larger distances. The best candidates are Supernovae Type Ia.

A supernova is the violent explosion of a dying star [CCRS15]. As a star burns out nearly all of its fuel (hydrogen and helium) by fusing it into heavier elements up to carbon and oxygen in the core of the star, one of two scenarios can occur [Fah14]

- If the mass of the star is larger than $\sim 8\ M_{\odot}$ then the pressure at the core is high enough to overcome the electron degeneracy pressure and fusion of carbon and oxygen occurs until iron and nickel are produced. At this point, photodissociation of ^{56}Fe and ^{4}He along with electron capture from free protons weaken the electron degeneracy pressure that no longer fights off gravity and a violent core-collapse occurs[6], followed by a outward rebound into a supernova (SNe).

- If the mass of the star is lower than $\sim 8\ M_{\odot}$, oxygen and carbon will form at the core but fusion can no longer be maintained. The outer layers of hydrogen and helium expand and form a planetary nebula, leaving the hot, dense[7] carbon-oxygen core exposed, becoming a white dwarf.

White dwarves have a finite mass limit of $1.4\ M_{\odot}$ from which the degeneracy pressure maintains the stability of the star, known as the Chandraseckhar limit. If a white dwarf has a companion star, the former can accrete material from the latter and grow in size and eventually reaching the Chandraseckhar limit. At this point a violent thermonuclear explosion of the carbon-oxygen core results in a supernova of the type Ia. Some studies show evidence that an alternative mechanism, where two white dwarves form a binary pair, is behind the SNe Ia phenomenon [HKRR13].

As this type of supernovae occurs for a precise mass of the dwarf star, the luminous output is practically constant between events, considering some light curve width corrections [P^{+}97]. The luminosity is also calibrated with data from *Cepheid* and *Lyrae* variable stars at lower z values. The SNe Ia well-determined maximum absolute magnitude as a function of the shape of their light curve allows the measurement of distances of order $\mathcal{O}(100\text{ Mpc})$.

It is possible to look at the acceleration history of the Universe, and thus determine the proper cosmological parameters, using supernova surveys [S^{+}12, P^{+}97, F^{+}01]. The distance modulus μ as a function of the redshift z and the deceleration parameter q_0 is defined as in Eq. 2.34.

---

[6] The collapse of the core has a radial velocity of around 0.3 c, equivalent to compress the Earth to the size of a house in 0.07 ms.

[7] As an example, a marble-size sphere of typical density white dwarf material would weigh around 100 tonnes.

$$\mu = m - M = 5log_{10}\left(\frac{d_L}{10\text{ pc}}\right) \approx 5log_{10}(z) + 1.086(1-q_0)z - 5log_{10}(h) + 42.40 + \mathcal{O}(z^2) \quad (2.34)$$

where d_L is the luminosity distance of the observed object. The SNe Ia surveys indicate that the deceleration parameter is approximately $q_0 \approx -0.55$ and dark energy dominates the energy density of the Universe. Figure 2.14 demonstrates the good agreement of several SNe Ia surveys, where an estimated value of $\Omega_\Lambda = 0.705^{+0.040}_{-0.043}$ is obtained from SNe Ia data alone [S$^+$12].

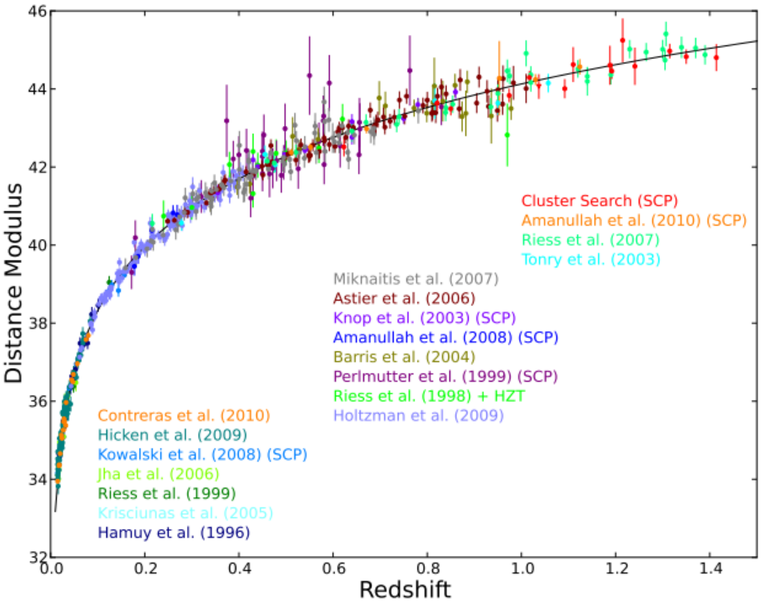

Figure 2.14: Best fit to the combined data of type Ia supernovae from several surveys. The distance modulus parameter μ as function of the redshift z depends on the deceleration parameter defined in Eq. 2.14 as shown in Eq. 2.34. Figure taken from [S$^+$12].

Figure 2.15 shows the confidence level contours in the $\Omega_m - \Omega_\Lambda$ space from SNe Ia, CMB and BAO data.

2.2.6 Gravitational Lensing

According to General Relativity, light propagates in a null geodesics in space-time. A distorted space-time, curved by the presence of a massive object, can bend the trajectory of light in an effect called gravitational lensing. Much like an optical lens, light becomes distorted to an observer if a massive object lies between its trajectory. Two different lensing regimes can occur: strong and weak gravitational lensing. The first occurs when the massive object distorts the light source in a way that aberrations like arching and multiple images are observed. The second regime is not so apparent to an observer, where the images of the background light sources are only slightly distorted and the effect is only perceived through statistical analysis of coherent distortions along a particular direction perpendicular to the gravitational lens [Mel99].

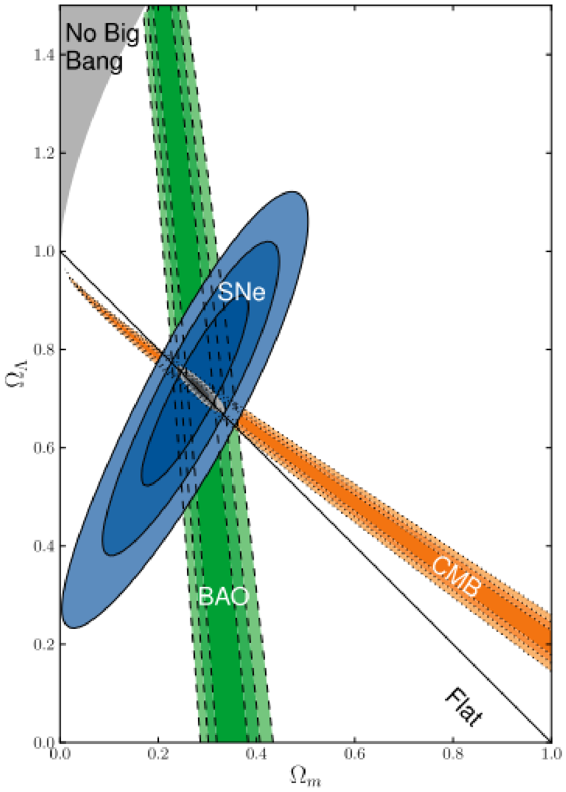

Figure 2.15: Constraints of the cosmological parameters Ω_m aand Ω_Λ from type Ia Supernova, Cosmic Microwave Background and Baryonic Acoustic Oscillations. The best value from all data is $\Omega_\Lambda = 0.724 \pm 0.016$ and $\Omega_m = 0.282 \pm 0.017$. The region marked with “No Big Bang” means that for that set of cosmological parameters the Universe starts in a contracting state, resulting in a bouncing Universe [CPT92]. Figure taken from [S+12].

The two regimes are represented in Figure 2.16 that shows a galaxy cluster simulation with a foreground invisible mass in the bottom left corner causing the lensing of the background image. Close to the massive object, strong gravitational lensing can be observed, where the distortion of the background image is evident, displaying tangential and radial arcs. Away from the distortion source, on the top right corner, only subtle weak gravitational lensing can be detected. The zoomed image of the top right corner shows the contours of the galaxies observed. The two lines at the top corner represent the true (lower line) and estimate (upper line) direction of the weak lensing effect, the latter obtained by statistical analysis.

Another regime, called microlensing, occurs when a massive object is aligned with a bright light source, such as a bright star or galaxy, increasing the luminosity of the source with no apparent distortion, focusing the light reaching the observer. This effect is rare because a sufficiently fine alignment of two bodies is unlikely.

As gravitational lensing allows the detection of massive objects with little to no light emission and the measurement of their mass, it becomes an outstanding tool for detecting the gravitational influence of dense dark matter structures present in dark galaxies and galaxy clusters.

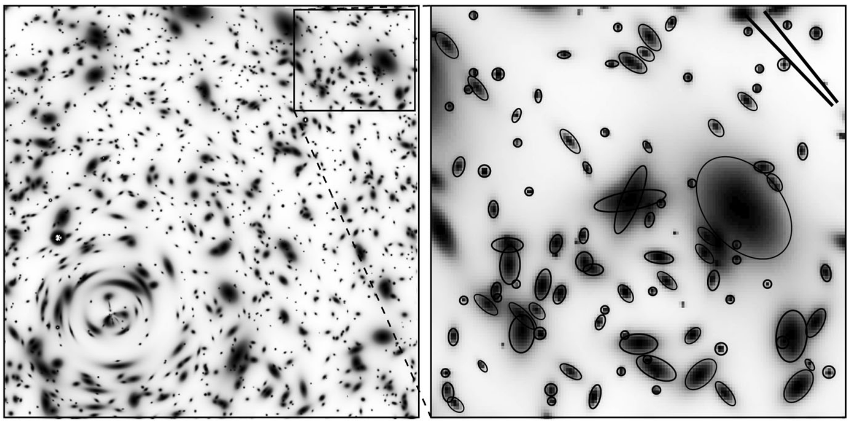

Figure 2.16: Representation of strong and weak gravitational lensing in an image of a galactic cluster with a simulated invisible mass in the foreground (bottom left corner). Figure taken from [Mel99].

One of the most compelling evidence of dark matter is found in the collision of clusters of galaxies. The Bullet Cluster (1E 0657-558) is the most famous case of two clusters colliding and an important finding for dark matter research [CBG⁺06].

Figure 2.17 shows the two clusters[8] colliding, superimposing the contributions of the X-rays emitted by the hot intergalactic gas (pink) and that of the mass that would generate the weak gravitational lensing observed (blue) to the image in the visible region of the spectrum. Clusters like the one presented are composed primarily of galaxies, intergalactic gas and the speculative dark matter. These components are expected to behave differently from each other in the event of a cluster collision.

It is apparent that the hot intergalactic gas and the galaxies in the cluster (the baryonic matter present in the cluster) and the majority of the mass of the cluster generating the gravitational lensing have a clear offset in their position, with 8σ significance, meaning that most of the mass of the cluster is not from the gas nor galaxies in it. Furthermore, this offset demonstrates that whatever comprises the majority of the mass content of the subclusters does not interact significantly with each other neither with regular matter, passing through the gas and remaining matter with its velocity unchanged.

As the clusters merge, colliding transversally to the field of view of an observer on Earth, the hot interstellar gas from a subcluster interacts strongly with the gas within the other subcluster, decelerating due to friction and heating up. As the galaxies in each cluster are dispersed, they pass by each other with practically no collisions and are neglectfully slowed down by the gas. But the majority of the mass in each subcluster carries on without slowing down, becoming separated in position from the gas.

The Bullet cluster not only provides a strong evidence to the existence of dark matter but also provides a good idea of its nature – a weakly-interacting and abundant matter. Modified gravity theories[9] cannot fully explain this phenomenon, favouring dark matter.

---

[8] The Bullet cluster is actually just the smaller, cone-shaped cluster, which is the reason for his name.

[9] See Section 2.3.5

Figure 2.17: Image of the bullet cluster where the contributions of the intergalactic gas from its X-ray emission (pink) and the majority of the matter in the cluster inferred from weak gravitational lensing (blue) are represented. The 8σ significance position separation between the gas from each colliding subcluster and the majority of the mass content of each subcluster is a strong evidence in favour of dark matter. Credit: X-ray: NASA/CXC/CfA/M.Markevitch et al.; Optical: NASA/STScI; Magellan/U.Arizona/D.Clowe et al.; Lensing Map: NASA/STScI; ESO WFI; Magellan/U.Arizona/D.Clowe et al.

Several other cluster collisions observed (MACS J0416.1-2403, MACS J0152.5-2852, MACS J0717.5+3745, Abell 370, Abell 2744 and ZwCl 1358+62) seem to be in agreement with the findings in the Bullet Cluster, meaning that these events are not anomalous.

2.3 Dark Matter Candidates

2.3.1 MACHOs

Massive Astrophysical Compact Hal Objects (MACHOs) are massive, non-luminous bodies of regular matter, such as neutron stars, white dwarfs, brown dwarfs, Jupiter-like planets, black holes[10], etc., that could explain the unaccounted mass in astrophysical systems [T^{+}07]. As these objects have low luminous output due to being cold or small-sized, their presence in a dynamical cosmic system would only be detected through their gravitational interaction with the luminous matter, providing a simple explanations for the “missing mass problem”.

The best way of determining the abundance of these objects is with gravitational microlensing (see Section 2.2.6). When a massive, compact, non-luminous object passes between the observer and a bright light source, such as a star, it distorts space and creates a lensing effect on the light coming from the star. The luminosity of the star increases when the object is completely aligned

---

[10] Not quite of baryonic nature, but still a valid contribution to the mass of a system from baryonic sources.

with the line of sight due to light being concentrated by the gravitational lens. A statistical survey of the sky that could effectively detect light variations would constraint the abundance of MACHOs in nearby systems. The EROS-2 collaboration surveyed 7 million stars in order to determine the MACHO contribution to dark matter. Only one microlensing candidate was detected, constraining the contribution to dark matter at less than 4% to low mass stars and planets, and less than 1% to objects with approximately the mass of the Sun [T$^+$07].

Another constraint on MACHOs is the young Universe we live in. Most of the dense baryonic matter structures would not have enough time to cool down enough in the time scale of structure formation in the Universe. Also, as these objects are very dense and would clump together, if dark matter was entirely composed of MACHOs then large structures of cool baryonic matter clumped together should be present in the Universe today.

2.3.2 WIMPs

Perhaps the most interesting and strongly motivated dark matter candidate is the Weakly Interacting Massive Particle, or WIMP. Strong evidences suggest that dark matter particles are of non-baryonic nature, do not interact via the electromagnetic force, are abundant enough to account for the missing matter density and are stable in the time scale of the age of the Universe [JKG96]. Dark matter does not interact significantly with either other dark matter particles or baryonic matter, as the Bullet Cluster collision suggests. WIMPs are defined as generic neutral particles with a mass between some GeV up to the TeV level that do not interact strongly with matter. This generic definition means that any particle with the characteristics of a WIMP could explain dark matter.

WIMPs would have been abundantly produced at the time of the Big Bang [JKG96]. In the extreme conditions of the early Universe, WIMPs, χ, would annihilate with their own antiparticles, $\bar{\chi}$, when temperatures were greater than the WIMP mass, $kT \geq m_\chi$.

$$\chi \; + \; \bar{\chi} \; \rightleftharpoons \; X \; + \; \bar{X} \tag{2.35}$$

where X and $\bar{X}$ denote any particle-antiparticle pair that couple to the weak force. The left arrow in Eq. 2.35 denotes the creation mechanism of WIMPs from pairs of particles in the hot primordial plasma. The abundance of WIMPs was maintained by this thermal equilibrium until temperatures dropped below the WIMP mass, where the creation process was suppressed and the equilibrium abundance began to decrease due to annihilation. The annihilation rate Γ_A of WIMPs is defined by Eq. 2.36,

$$\Gamma_A = n_\chi \langle \sigma_A v \rangle \tag{2.36}$$

where n_χ is the WIMP number density, σ_A is the WIMP annihilation cross section and v is the relative velocity of the two particles, making the term $\langle \sigma_A v \rangle$ the thermally averaged annihilation cross section. As annihilation proceeds, the number density n_χ decreases and so does the annihilation rate. The turning point comes when Γ_A decreases below the expansion rate of the Universe ($\Gamma_A < H$), thermal equilibrium is broken as the processes depicted in Eq. 2.35 "freeze out". The result is a thermal "relic" density of WIMP particles that, if the WIMP is stable, remains to this day. This "relic" density today depends on the strength of the annihilation cross section, as a higher annihilation (or a slow expansion rate) results in fewer WIMPs today.

The relic density of WIMPs can be estimated from the Boltzmann equation for the processes in 2.35 [JKG96]

$$\frac{dn_\chi}{dt} + 3Hn_\chi = \langle\sigma_A v\rangle[(n_\chi^{eq})^2 - (n_\chi)^2] \tag{2.37}$$

The left-hand side of Eq. 2.37 accounts for the dilution of the WIMP number density with the expansion of the Universe, while the right-hand side represents the annihilation (n_χ term) and creation (n_χ^{eq} term) dependencies. There is no analytical solution for Eq. 2.37, but a simple analytical approximation with an expected error of $\sim 10\%$ can be made [JKG96].

$$\Omega_\chi h^2 \approx \frac{3 \times 10^{-27}\ \text{cm}^2\ \text{s}^{-1}}{\langle\sigma_A v\rangle} \approx \frac{0.1\ \text{pb c}}{\langle\sigma_A v\rangle} \tag{2.38}$$

This result is independent of m_χ. The WIMP density contribution is inversely proportional to the thermal annihilation cross section, as discussed before. A massive particle with an annihilation cross section of order $\sim 10^{-25}$ cm^2 s^{-1}, the scale of the weak interaction, would result in a relic abundance of $\Omega_\chi h^2 \sim 0.1$, remarkably similar to the energy density contribution of the non-baryonic matter observed today $\Omega_{DM,0}h^2 \approx 0.1188$. It is important to notice that there is no *a priori* reason to use a weak-scale interaction in these calculations, meaning that the definition of WIMPs alone is compatible with the observations of the cosmological parameters.

Supersymmetric WIMPs

Supersymmetry (SUSY) is an extension of the Standard Model (SM) of particle physics that introduces a global symmetry between fermions and bosons [JKG96]. This model implies that every SM particle has a superpartner of the opposite nature - fermions have bosonic superpartners (**s**fermion) and bosons have fermionic superpartners (bos**ino**). A spontaneously broken supersymmetry gives the superpartners a large mass, explaining why no superpartner was discovered yet.

The Minimal Supersymmetric Standard Model (MSSM) offers some WIMP candidates, being the most relevant the lightest supersymmetric particle (LSP) [JKG96]. MSSM theories introduce R-parity to explain the stability of the proton, that grant all supersymmetric particles $R = -1$, and all Standard Model particles $R = +1$. This means that the LSP cannot decay as it is the lightest particle with $R = -1$, making it stable and long-lived. Most models indicate the *neutralino*, a linear *eigenstate* combination of the supersymmetric partners of the photon (*photinos*), Z^0 (*zinos*) and the Higgs bosons (*higgzinos*). The mass of the neutralino is, according to some models, in the range of $10 - 1000$ GeV and its interaction cross section with matter is at the weak scale [JKG96].

The MSSM has recently been put to the test by the LHCb detector, that measured the decay rate of the $B_s \to \mu^- \mu^+$, having results inconsistent with the expected from minimal supersymmetry models, favouring the SM predictions [LA+13].

2.3.3 Neutrinos

The Universe is filled with weakly-interacting, neutral, relativistic neutrinos that could, at least in part, explain the dark matter density observed. However, structure formation and calculated relic density of neutrinos disfavours these candidates as a complete explanation for dark matter [Fah14]. Neutrinos are very light particles, with total mass from the three neutrino species combined[11] being less than $\sum m_\nu < 0.194$ eV [PA+15], resulting in neutrinos travelling at relativistic speeds and classified as *Hot Dark Matter* (HDM), in contrast to non relativistic *Cold Dark Matter* that best explains the Universe we see today.

If a galactic halo was comprised only of neutrinos, these particles would disperse due to their velocities being greater that the escape velocity of the galaxy. This can be proven using the Virial theorem. For an ultra-relativistic (UR) gas of non-interactive particles bounded by a central potential, the Virial theorem states that [Cun15]

$$\langle E_K \rangle \approx -\langle \Omega \rangle \tag{2.39}$$

Eq. 2.39 states that in a weak gravitational field, a self gravitating gas of UR particles would have total energy $\langle E \rangle = \langle E_K \rangle + \langle \Omega \rangle \approx 0$. This is characteristic of a unbound system because no energy is required to remove a particle from the gravitational potential. Neutrinos could not form a dark matter halo to explain the observed flat galactic rotation curves [Cun15].

From thermal relic calculations, the neutrino density contribution is calculated to be:

$$\Omega_\nu = \frac{0.336 \ \ m_\nu}{5.2 \text{ [eV]}} \tag{2.40}$$

For neutrinos to account for the entire dark matter density in the Universe, their mass would have to be around 4 eV. Planck constraints the mass of the neutrinos at $m_{\sum \nu} < 0.194$ eV, from CMB data, resulting in a neutrino contribution to dark matter of only around $\Omega_\nu = 0.013$.

---

[11] Neutrinos present themselves in three different flavours: electron, muon and tau neutrinos.

2.3.4 Axions

The axion is doubly motivated as a dark matter candidate because it would not only solve the dark matter problem but would also solve a major problem of particle physics – the CP violation in strong interactions [Fah14].

The strong CP problem is manifested in the discrepancy of the expected large value of the neutron electric dipole moment, d_n and the measurements performed. The neutron electric dipole moment (nEDM) was measured to be remarkably small, of order $|d_n| < 2.9 \times 10^{-26}$ e cm [B$^+$06], being inconsistent with the expected from *Quantum Chromodynamics* (QCD).

A possible solution for the CP problem was introduced by Peccei and Quinn, in 1977. A new hidden and spontaneously broken global symmetry (PQ symmetry) allows the value of nEDM to relax to zero. A spontaneously broken symmetry generates a pseudo-Goldstone boson [Fah14], and in the case of the PQ symmetry, the axion arises.

Axions would not be produced thermally [B$^+$12b], meaning that they are not expected to acquire relativistic speeds. If they exist, they would contribute to the dark matter density of the Universe as cold dark matter.

The detection of axions can be made using different methods. The *Axion Dark Matter eXperiment* (ADMX) collaboration [vBC13] uses a microwave resonance cavity with a strong magnetic field to detect resonant radio frequencies corresponding to the Compton wavelength of the axion, measuring its mass. The ADMX experiment excluded axions with masses between $1.9 - 3.6$ μeV. In the presence of a strong magnetic field, axions can decay into photons by the Primakoff effect [FRS$^+$14]. This forced decay of the axion can also happen in reverse, where two photons convert into an axion. This effect is expected to occur inside the Sun, resulting in the emission of axions [FRS$^+$14].

WIMP direct detection experiments can also detect axions at a certain level because of the axio-electric effect, when an axion is converted to a photon inside the detector volume and produces an electron recoil.

2.3.5 Modified Gravity

Despite being a rivalling theory to dark matter and not a DM candidate, it is important to make a brief overview of modified gravity theories, in particular, the Modified Newtonian Dynamics (MOND) [Sca06].

Modified gravity looks at the “missing mass problem” from a different point of view: no mass is missing in the system, luminous matter alone is present on large scale structures, avoiding the need to summon new exotic, non interacting particles. The effects of additional mass observed is the result of the alleged misconception that Newtonian gravity works the same way locally and at large distances. MOND was developed to explain the galactic rotation curves without the need to invoke additional mass.

However, MOND fails at calculating the total mass of clusters because it is not general enough to cover medium-scale and large-scale effects simultaneously, still requiring a substantial amount of unseen matter to justify the observed motion. MOND also fails to explain gravitational lensing. But the most compelling evidence of dark matter still cannot be justified using any modified gravity theory: the Bullet cluster represents a transversal effect of non interactive dark matter being separated from the baryonic gas of the colliding clusters [AFZ06]. Modifying the gravitational influence at larger scales would not justify the effect observed, as it requires a non interacting matter with no light scattering, emitting or absorbing proprieties.

Chapter 3

Galactic Halo and Detection of Dark Matter

A very prominent evidence of dark matter is found when analysing galactic dynamics. Ever since Jan Ort published his article on the unexpected movement of stellar objects in the Sun's neighbourhood [Oor32], a considerable amount of non-luminous matter was thought to be present in our galaxy. The findings of Vera Rubin in her studies of galactic rotation curves indicate that a large amount of matter reaching further than the luminous galactic disk surrounds each observed galaxy, being the largest contribution for the mass of the galaxies [Rub83].

If the dark matter halo is composed of WIMPs, then the WIMP flux passing through the Earth would result in some measurable scattering events with a target of enough mass, or WIMP annihilation products should be detectable in high WIMP density regions. The purpose of this Chapter is to briefly explore the various WIMP detection methods and the expected signal and event rate for a dark matter direct detection experiment, considering the canonical dark matter halo model and some non-canonical approaches.

3.1 Detection Methods

The search for dark matter is not exclusive to the observation of gravitational or cosmological effects of its presence in a system. The nature of dark matter is currently unknown and only with a detection experiment, either indirect or direct measurement of WIMP interactions, can some light be shed on the proprieties of WIMPs. An indirect detection would refer to the measurement or observation of WIMP annihilation products, while a direct detection means the measurement of signal from a WIMP interaction with a material target on Earth. Another possible method of detecting dark matter would be the production of dark matter particles at particle colliders.

Indirect detection

Indirect detection of dark matter would provide valuable information about the DM particles. WIMP annihilation would result in the creation of particle-antiparticle pairs with high energy, as in Eq. 2.35. These particles could be high-energy neutrino-antineutrino pairs or two photons that could easily reach a Earth-bound detector.

The Fermi Gamma-Ray Space Telescope (FGST, former GLAST) searches for WIMP annihilation signatures by measuring high-energy γ ray emissions in Dwarf Spheroid Galaxies (DSG) – galaxies with a relative large amount of dark matter and a small number of γ ray sources [CHL15]. DSGs are the most promising place to search for WIMP annihilation γ rays, as they have a high dark matter density that favours WIMP self-annihilation.

In September 2014, the XMM-Newton space observatory claimed the detection of an Axion decay signature in the magnetosphere of the Earth [FRS$^+$14]. Axions can forcefully decay into photons in a strong magnetic field as the one generated by our geodynamo (the Primakoff effect, see Chapter 2.3.4). The XMM-Newton findings could be explained by other effects unrelated to solar axion production, as stated by some authors [RT15].

Despite the advantages of a indirect detection signal, the information obtained is very model-dependent and could be open to interpretation, as it was the case of the XMM-Newton 2014 findings.

Production of dark matter

Another possible method to search for dark matter is the creation of dark matter particles in particle colliders like the LHC at CERN and Tevatron at Fermilab [A$^+$13b, C$^+$12, BFH10].

In the conditions of the early universe, when particles had enough thermal energy, the process denoted by the left arrow in Eq. 2.35 on Section 2.3.2 was undergoing, as Standard Model (SM) particles annihilated to produce dark matter particles. Given enough energy in order to produce the dark matter particle-antiparticle pair – $E_{th} > 2m_\chi$ – it should be possible to recreate this reaction at a particle collider. This method provides more information about dark matter particles, if observed, than any other method, not only exploring the nature of the particles but also supporting or excluding different standard model extensions that predict dark matter candidates, like supersymmetry (SUSY) models.

The mass of the *Higgs* boson, discovered in 2012 [A$^+$12a], is in agreement with SUSY predictions – gauge symmetry protects the *Higgs* potential from divergence and grand unification of the gauge couplings is achievable [CCP06]. This serves as a tremendous motivation to investigate SUSY theories at the LHC. If an R-parity conserving supersymmetric extension of the SM exists, events with gluon jets, leptons and a large amount of missing transverse energy should be observed at electroweak-scale energies. The missing energy is the result of the low interaction cross section of a dark matter particle that, upon creation, would leave the detector without interacting.

So far no solid evidence for SUSY particle creation was achieved, as the events being searched are consistent with the expected SM background events. However, some particle physics experiments like the Tetravon at Fermilab and ATLAS and CMS at CERN have set constraints on dark matter mass and production cross section, as well as constraint some Supersymmetry (SUSY) theories [A$^+$13b, A$^+$13a, A$^+$14, A$^+$15, C$^+$12, BFH10]. The constraints from CMS and ATLAS on neutralino[1] cross section for spin-dependant interactions with SM particles are the most stringent amongst direct detection and production experiments by several orders of magnitude over the entire $1 - 1000$ GeV mass range, while for spin-independent models, CMS presents the best constraints for WIMP masses below 3.5 GeV [C$^+$12, A$^+$13a] (a detailed discussion on WIMP spin-dependent and spin-independent interactions is presented on Section 3.2.1).

Direct detection

Direct detection of dark matter provides constraints on the interaction cross section of these particles with normal matter. This method does not provide as much information about the particles being detected as production or indirect detection methods, but could present the strongest evidence for the existence of a non-baryonic component of matter in the universe as well as a value for the interaction cross section of such matter with baryonic matter.

The difference between direct and indirect detection is not standard. The simplest definition is to consider the measurement of dark matter interaction events on an Earth-bound detector as direct and the detection of signatures from dark matter interaction elsewhere as indirect. On this basis, both axion and WIMP search on specialized detectors are defined as direct detection experiments. This work will focus on WIMP direct detection only.

WIMP direct detection experiments aim to detect nuclear recoils caused by the elastic scattering of dark matter particles with the atoms of a target material in a low-background detector. More specifically, the goal is to measure the rate and energies of the nuclear recoils [Sch10]. Some experiments search for an annual modulation of WIMP signal and others also aim to measure the scatter direction of the nucleus to infer the direction of the dark matter flux on Earth.

If a dark matter particle interacts with a nucleus of a target material, the deposited energy can be measured. The main difficulty in the search for dark matter is the expected low rate of events due to its weak-interacting nature. The detector for a WIMP search experiment needs to suppress background events in order to allow the rare WIMP scattering signals to be observed. Therefore, the validity of a direct detection signal is dependent of the rejection of background events with the same characteristics of that of a WIMP scattering signal. Usually these low-

---

[1] The neutralino, χ^0, is the lightest stable particle on several SUSY theories and a strong candidate to explain dark matter. See Section 2.3.2.

background experiments are operated underground to reduce the flux of cosmic particles that contribute to the background events. Additional concerns on the materials used and on operating conditions, such as the cryogenic temperatures of semiconductor detectors, are also essential.

The excitation energy of a target atom due to a nuclear recoil caused by a WIMP scatter can be measured by three main channels: ionization charge, phonons[2] and scintillation. Furthermore, a detector that uses more than one excitation channel can use the different measured signals to provide extra discrimination methods, as the nuclear recoils from WIMPs and interactions from electromagnetic background sources often produce distinct signatures [Sch10].

By measuring one or more excitation channels, detectors can be divided into four main types:

1. Threshold detectors, like the COUPP experiment [B$^+$12a], use superheated fluid, tuning some thermodynamic parameters, to measure nucleation events from ionization of the target material, similar to bubble chambers.
2. Crystal scintillator detectors measure light signals arising from DM particles interacting within the target material. Usual crystal materials are NaI and CsI. DAMA and DAMA/Libra [B$^+$03, B$^+$13] experiments use ultra-pure NaI crystals[3].
3. Liquid noble element detectors, such as ZEPLIN-III and LUX (described in more detail on Section 4), measure scintillation and/or ionization[4] from interactions with the liquid target volume.
4. Semiconductor detectors measure ionization, heat or scintillation in cryogenic crystals of ultra-pure materials. The most common materials are germanium or silicon crystals at mK temperatures. The CDMS experiment [A$^+$13c] is an example of a semiconductor detector.

3.2 The Canonical Halo model

The simplest model to describe a dark matter halo that encompasses the Milky Way galaxy is considering a isothermal spherical distribution of non-interacting particles that behave as an ideal gas. This state of affairs is denoted the “Canonical” model [LS96].

The halo is considered to have no bulk rotation – otherwise it would be flat at the poles and hence not spherical – and WIMPs move with no preferable direction within the halo. The

---

[2] Vibrations of the target lattice, resulting in increased heat that can be detected in ultra-cooled semiconductor detectors.

[3] The DAMA and DAMA/Libra experiments have claimed to measure a seasonal variation on the 12 year data collected due to WIMP interactions [B$^+$13], but several other experiments [A$^+$13e, A$^+$13c, A$^+$10, A$^+$12f] with increased sensitivity have not yet detected any WIMP interactions to support these claims.

[4] Single-phase set-ups allow scintillation produced in the liquid target to be measured, while Dual-phase (liquid and gas) allows scintillation production in the liquid and extraction ionization charges with an electric field into the gas phase to be measured.

velocity distribution of these particles can be modulated with a Maxwell-Boltzmann (Gaussian) distribution as demonstrated in Eq. 3.1 [LS96]

$$f(\vec{v}+\vec{v}_E) = e^{-(\vec{v}+\vec{v}_E)^2/v_0^2} \tag{3.1}$$

The parameter $\vec{v}$ is the velocity of the particles onto the detector target, and $\vec{v}_E$ is the velocity of the Earth relative to the dark matter distribution. The Earth moves across the WIMP halo due to the motion around the Sun, the motion of the Sun relative to nearby stars, and the circular velocity at the location of the Sun. The most likely WIMP velocity, v_0, can be approximated to the circular velocity as $\langle v_0 \rangle \approx \langle v_r \rangle$ [LS96]. At the location of the Sun, $R_\odot \approx 8.5$ kpc, this velocity is taken to be $v_r = 220$ km s^{-1} [P$^+$14, B$^+$12c] but some authors suggest a higher number, Lewin and Smith use ~ 230 km s^{-1}. On the following calculations, the value of $v_r = 220 \pm 20$ km s^{-1} [Sch10] will be used as it agrees with most of the recent measurements.

Eq. 3.2 represents the modulation of the velocity of the Earth due to its orbital motion around the Sun.

$$v_E = 220 + 15\cos\left(2\pi\frac{t-152.5}{365.25}\right) \text{ km s}^{-1} \tag{3.2}$$

The date $t - 152.5$, with t in days, is relative to June 2$^{\text{nd}}$. This annual modulation results in a variation of the event rate and nuclear recoil spectrum that can be measured by a dark matter experiment. The DAMA/Libra collaboration claim to have detected a modulated signal due to the annual variation of the WIMP scattering event rate with 8.2 σ significance [B$^+$13], but the results are widely contested, and the result could be caused by another annually modulated phenomenon not being considered. Several other dark matter experiments have surpassed the sensitivity of DAMA/Libra with no positive detection results. Despite the critics, no phenomenon yet proposed has been able to completely justify the modulated signal.

There is a limit to the kinetic energy of a WIMP particle that is bound to the galactic halo, defined by the escape velocity. This velocity is measured to be $492 < v_{esc} < 587$ km s^{-1} by the RAVE survey [P$^+$14], with a 90% confidence limit and a median value of 533 km s^{-1} at the radial distance of the Sun. Studies of the motion of halo stars[5] return values of the local escape velocity of $v_{esc} = 550.9^{+32.4}_{-22.1}$ km s^{-1} [KSLB14], in agreement with the values obtained by the RAVE survey. This limit results in a sharp cut-off on the energy of a WIMP given by Eq. 3.3 for a non-relativistic particle in the halo.

$$E_\chi < E_{esc} = M_\chi \frac{v_{esc}^2}{2} \tag{3.3}$$

The density of the Milky Way dark matter halo is estimated by Gates, Gyuk and Turner [GGT95]

---

[5] Halo stars are bound to the galaxy gravitational potential but move outside the galactic disk, with inclined orbits relatively to the galactic plane.

between $0.3 < \rho_{DM} < 0.7$ GeV cm^{-3}, but more recent surveys point to a value of $\rho_{DM} = 0.35 \pm 0.08$ GeV cm^{-3} [KSLB14]. On this work the value of the local density is considered to be $\rho_{DM} = 0.4$ GeV cm^{-3}, as considered in Lewin and Smith, as a conservative limit on the WIMP event rate. The local number density of WIMPs is then defined as in Eq. 3.4.

$$n_\chi = \frac{\rho_{DM}}{M_\chi} \tag{3.4}$$

The density profile for a isothermal spherical halo does not have a analytic solution, but it can be approximated by Eq. 3.5, where $v_\infty \approx v_r$ and $r_c \approx 2.8$ kpc is the core radius that is fitted to the rotation curve [KK98].

$$\rho(r) = \frac{v_\infty^2}{4\pi G r_c^2} \frac{r_c^2}{r_c^2 + r^2} \tag{3.5}$$

If WIMP particles have a mass of $M_\chi = 100$ GeV, a litre bottle of water would enclose on average 4 WIMP particles. This number density associated with the average WIMP speed results in an average flux of $\Phi_\chi \approx 10^7/M_\chi$ s^{-1} cm^{-2}, or around 10 million particles passing through the area of a fingernail every second. Despite the weakly interacting nature of dark matter, this expected high flux of WIMP particles makes direct detection practicable.

With the galactic halo proprieties described, the expected WIMP scattering event rate and the recoil energy spectrum can be calculated. The calculations presented in this chapter follow the work of Lewin and Smith [LS96].

3.2.1 WIMP interaction cross section

Using the parametrization of the canonic halo model described in the previous section, the event rate and recoil energy spectrum of WIMP interactions with an ordinary matter target can be calculated.

Using the Fermi Golden Rule, represented in Eq. 3.6, the energy dependence of the WIMP-nucleus interaction cross section can be divided into a zero-momentum transfer cross section term, σ_{0WN}, and the form factor term $F^2(q)$ containing the dependence on the momentum transfer q [Sch10].

$$\frac{d\sigma_{WN}(q)}{dq^2} = \frac{\sigma_{0WN} F^2(q)}{4\mu_A^2 v^2} \tag{3.6}$$

Here v is the WIMP velocity, μ_A is the WIMP-nucleus reduced mass, $\mu_A = M_\chi M_A/(M_\chi + M_A)$, for the mass of a WIMP particle M_χ and the mass of the nucleus M_A with a mass number A. The zero momentum transfer WIMP-nucleus cross section can be separated into a spin-dependent (SD) and spin-independent (SI) component, as described in Eq. 3.7 [KK04, Sch10].

$$\sigma_{0WN} = \frac{4\mu_A^2}{\pi}(Zf_p + (A-Z)f_n)^2 + \frac{32G_F^2\mu_A^2}{\pi}\frac{J+1}{J}(a_p\langle S_p\rangle + a_n\langle S_n\rangle)^2 \tag{3.7}$$

The parameters $f_{p,n}$ and $a_{p,n}$ are effective spin-independent and spin-dependent couplings, respectively, of the WIMP particle with a proton or neutron. The remaining terms are characteristic of the target material: atomic number Z, atomic mass A, total nuclear spin J and the expectation values of the proton and neutron spins within the nucleus $\langle S_{p,n}\rangle = \langle N|S_{p,n}|N\rangle$. The first half of the right-hand side of Eq. 3.7 represents the spin-independent component and the second half represents the spin-dependent component. An even number of protons or neutrons in a nucleus would result in a lower expectation value of the respective nucleon spin within the nucleus, $\langle S_{p,n}\rangle$, meaning that only target materials with odd number of protons or neutrons are sensitive to proton or neutron SD interactions, respectively. Also, targets with even number of both protons and neutrons have $J = 0$ and are insensitive to SD interactions.

Some experiments have presented good constraints on WIMP SD interaction cross section [A$^+$13f, B$^+$12a] but despite SD couplings being around three orders of magnitude larger than SI couplings [Sch10], background or background rejection difficulties and the resulting lower sensitivity of these experiments results in the lack of benefit from SD experiments and the favouring of spin-independent constraints on the WIMP cross section.

For SI interactions, the effective couplings are expected to be identical, $f_p \approx f_n$, meaning that the SI component of the zero-momentum transfer WIMP-nucleus interaction cross section can be expressed as:

$$\sigma_{0WN,SI} = \frac{4\mu_A^2}{\pi}f_n^2A^2 \tag{3.8}$$

The subscript letter n in Eq. 3.8 now refers to "nucleon". It is generally more useful to express the WIMP-nucleon interaction cross section, which is independent of the target material and allows for the comparison of results from experiments with using different targets. Eq. 3.8 can be rewritten as:

$$\sigma_{0WN,SI} = \frac{4\mu_n^2f_n^2}{\pi}\frac{\mu_A^2}{\mu_n^2}A^2 = \sigma_{SI}\frac{\mu_A^2}{\mu_n^2}A^2 \tag{3.9}$$

The dependence on the target material is called the coherence factor, expressed in the term $A^2 \quad \mu_A^2/\mu_n^2$. The (target independent) SI WIMP-nucleon interaction cross section is expressed in Eq. 3.10.

$$\sigma_{SI} = \frac{4\mu_n^2f_n^2}{\pi} \tag{3.10}$$

Nuclear form factor correction

The effective particle-nucleus scattering cross section begins to drop when the transferred momentum $q = \sqrt{2M_A E_R}$ increases beyond a point where the associated de Broglie wavelength $\lambda = h/q$ is no longer large in comparison to the nuclear radius. As taken from Eq. 3.6, the effective cross section can be expressed by a "zero-momentum transfer" cross section σ_0 that contains all dependencies on the specific interaction, and a nuclear form factor $F(q)$ that contains all the dependencies on the transferred momentum.

$$\sigma(q) = \sigma_0 F^2(q) \tag{3.11}$$

The term σ_0 does not depend of the transferred momentum and represents the effective cross section for small values of q, *i.e.* $q \to 0$, where the form factor is unity. The form factor correction to the WIMP-nucleus elastic scattering cross section is a modifier of the cross section in order to account the internal nuclear structure. In the first Born approximation, for a nucleus with finite size, the form factor is the Fourier transform of the spacial density distribution of nucleons (scattering centres) in the nucleus, $\rho_n(r)$, so that:

$$F(q) = \int \rho_n(r) e^{-i\vec{q}\cdot\vec{r}} d^3r \tag{3.12}$$

Eq. 3.12 can be simplified considering a spherically symmetric distribution of nucleons inside the nucleus:

$$F(q) = \frac{4\pi}{q} \int_0^\infty r \cdot \sin(qr) \rho_n(r) dr \tag{3.13}$$

As a WIMP scattering can be spin-dependent or spin-independent, it is useful to consider the form factor obtained by Fourier transform of:

(a) a thin shell that represents the unpaired nucleon in the nucleus, for SD interactions.
(b) a solid sphere that represents the whole nucleus, for SI interactions.

For the thin shell approximation (SD interactions), the Fourier transform returns the first spherical Bessel function:

$$F(q)_{\text{ (thin shell)}} = j_0(qr_N) = \frac{\sin(qr_N)}{qr_N} \tag{3.14}$$

where r_N is the effective nuclear radius.

For the solid sphere approximation (SI interactions), the resulting form factor is:

$$F(q)_{\text{ (solid sphere)}} = \frac{3j_1(qr_N)}{qr_N} = \frac{3}{(qr_N)^3}\left[\sin(qr_N) - qr_N\cos(qr_N)\right] \tag{3.15}$$

The nuclear charge density distribution is usually approximated by either a Fermi or Gaussian distribution, given by:

$$\rho(r)_{\text{ (Fermi)}} = \frac{\rho_0}{1+e^{\frac{(r-R_u)}{a}}} \tag{3.16}$$

$$\rho(r)_{\text{ (Gaussian)}} = \rho_0\left(1+\frac{\omega r^2}{a^2}\right) + e^{\frac{(r^2)}{a^2}} \tag{3.17}$$

where R_u is the characteristic radius parameter, ω is the oscillator angular frequency, and a is the surface diffuseness parameter [Viv10]. The Fermi distribution is generally considered to be the most realistic. However, a truncated Gaussian distribution proposed by Helm [Hel56] has the advantage of yielding an analytical form factor, given by:

$$F(qr_N) = \frac{3j_1(qr_N)}{qr_N}e^{-\frac{(qs)^2}{2}} \tag{3.18}$$

where s is a measure of the nuclear skin thickness, defined as the distance in which the density goes from 90% to 10% of the maximum and considered to be essentially constant at $s \approx 0.9$ fm. The value for the effective nuclear radius of $r_N = 1.14A^{1/3}$ fm provides a good fit of the Helm distribution to the numerically integrated Fermi distribution for most values of A and in the NR energy range of $0-400$ keV [LS96].

3.2.2 Event rate

The basic event rate per unit mass of WIMP interactions with a cross section per nucleus σ on a target of atomic mass A, is given by:

$$dR = \frac{N_A}{A}\sigma v dn \tag{3.19}$$

where n is the WIMP number density and $N_A = 6.022\times10^{26}$ mol^{-1} is the Avogadro number. The event rate for the zero momentum transfer cross section, *i.e.*, ignoring the form factor correction, is then obtained by integrating Eq. 3.19:

$$R = \frac{N_A}{A}\sigma_0\int v dn \equiv \frac{N_A}{A}\sigma_0 n_0\langle v\rangle \tag{3.20}$$

The time-independent rate per unit mass for zero Galactic velocity $v_E = 0$ and $v_{esc} = \infty$ (using the definition of n_0) is defined as:

$$R_0 = \frac{2}{\sqrt{\pi}} \frac{N_A}{A} \frac{\rho_{DM}}{M_\chi} \sigma_0 v_0 \tag{3.21}$$

so that:

$$R = R_0 \frac{\sqrt{\pi}}{2} \frac{\langle v \rangle}{v_0} \approx R_0 \frac{1}{2\pi v_0^4} \int v f(\vec{v} + \vec{v}_E) d^3 v \tag{3.22}$$

The differential rate is then given by:

$$dR = R_0 \frac{1}{2\pi v_0^4} v f(\vec{v} + \vec{v}_E) d^3 v \tag{3.23}$$

The total rate R_0 is expressed in units kg^{-1} d^{-1} or "*tru*" for total rate units. Considering a WIMP mass of $M_\chi = 100$ GeV, a target made of xenon ($A = 131$) and a WIMP-nucleon interaction cross section $\sigma_{0Wn,SI} = 1 \times 10^{-45}$ cm^2, using Eq. 3.21 the total rate obtained is $R_0 \approx 2.37 \times 10^{-3}$ kg^{-1} d^{-1}, or less than 1 event per kg of target material per year.

The goal of direct detection experiments is to measure the rate and the signature energy spectrum of WIMP elastic scattering interactions with the nuclei of the target material. The recoil energy of a nucleus struck by a WIMP with kinetic energy $E = 1/2 M_\chi v^2$ scattered by an angle θ is given by:

$$E_R = Er \frac{(1 - \cos\theta)}{2} \tag{3.24}$$

where r is a dimensionless parameter related to the reduced mass μ_A as:

$$r = \frac{4\mu_A^2}{M_\chi M_A} = \frac{4 M_\chi M_A}{(M_\chi + M_A)^2} \tag{3.25}$$

Notice that $r \leq 1$ for any set of values of M_χ and M_A. The maximum value $r = 1$ arises from $M_\chi = M_A$, meaning that the recoil energy is maximum when the target nucleus has the same mass as the WIMP particle. This results in different target materials being more sensitive to different WIMP masses.

As the scatters are assumed isotropic (uniform in $\cos\theta$) the recoils are uniformly distributed in $0 \leq E_R \leq Er$, and so:

$$\frac{dR}{dE_R} = \int_{E_{min}}^{E_{max}} \frac{1}{Er} dR(E) = \frac{1}{E_0 r} \int_{v_{min}}^{v_{max}} \frac{v_0^2}{v^2} dR(v) \tag{3.26}$$

The minimum particle energy that can generate a recoil of energy E_R is $E_{min} = E_R/r$. The most likely WIMP energy E_0 is the energy of a WIMP particle with velocity v_0, *i.e.* $E_0 = 1/2 M_\chi v_0^2 = (v_0^2/v^2)E$. The minimum velocity v_{min} is the correspondent velocity of a WIMP particle with energy E_{min}, *i.e.* $v_{min} = \sqrt{2E_{min}/M_\chi} = \sqrt{E_R/E_0 r}v_0$.

Now the result from Eq. 3.23 can be used to obtain the nuclear recoil spectrum, as represented in Eq. 3.27.

$$\frac{dR}{dE_R} = \frac{R_0}{E_0 r}\frac{1}{2\pi v_0^2}\int_{v_{min}}^{v_{max}} \frac{1}{v} f(\vec{v}+\vec{v}_E)d^3v \tag{3.27}$$

Considering again $v_E = 0$ and $v_{esc} = \infty$, Eq. 3.27 yields the expression for the unmodified nuclear recoil energy spectrum:

$$\frac{dR(v_E = 0, v_{esc} = \infty)}{dE_R} = \frac{R_0}{E_0 r} e^{-\frac{E_R}{E_0 r}} \tag{3.28}$$

Again, judging from Eq. 3.25, the differential rate is maximum when $r \approx 1$, meaning that it is desirable to have materials whose nuclear mass is similar to the expected WIMP mass. For this simplified model, the expected recoil energy is given by the mean value of the exponential distribution $\langle E_R \rangle = E_0 r$. For a WIMP mass of 100 GeV with expected income velocity $v_0 = 220$ km s^{-1} scattering with a xenon nucleus ($A = 131$), an average recoil energy $\langle E_R \rangle \approx 25$ keV is obtained.

For non-zero v_E and finite v_{esc}, the differential event rate takes a more complex form, represented in Eq. 3.29.

$$\frac{dR(v_E, v_{esc})}{dE_R} = \frac{k_0}{k_1}\frac{R_0}{E_0 r}\left[\frac{\sqrt{\pi}v_0}{4v_E}\left[erf\left(\frac{v_{min}+v_E}{v_0}\right) - erf\left(\frac{v_{min}-v_E}{v_0}\right)\right] - e^{-\frac{v_{esc}^2}{v_0^2}}\right] \tag{3.29}$$

Here $erf()$ represent the error function. The constants k_0 and k_1 are normalization factors related to the velocity distribution $f(\vec{v}+\vec{v}_E)$ arising from considering $v_{esc} = \infty$ and by truncating the velocity distribution at $|\vec{v}+\vec{v}_E| = v_{esc}$, respectively. Eqs. 3.30 and 3.31 represent these normalization factors as obtained by Lewin and Smith.

$$k_0 = (\pi v_0^2)^{3/2} \tag{3.30}$$

$$k_1 = k_0\left[erf\left(\frac{v_{esc}}{v_0}\right) - \frac{2v_{esc}}{\sqrt{\pi}v_0}e^{-\frac{v_{esc}^2}{v_0^2}}\right] \tag{3.31}$$

3.3 Non-Canonical Halos

The canonical halo model is the simplest conjecture of the distribution of dark matter that surrounds our galactic disk. As stated in Section 3.2, this simplified halo has a isothermal spherical shape with no bulk rotation. However, most of the dark matter halos that surround galaxies are not strictly spherical but irregular ellipsoids [WHC$^+$15, KSLB14]. Also, galactic dark matter structures are expected to have some rotation due to conservation of angular momentum of any small net rotation of the dark matter distribution as they collapse to form the halo. This rotation results in some flattening of the halo at the rotation poles, which results in a variation of the local dark matter density ρ_χ up to a factor of two [KK98].

Furthermore, the halo could have an alternative radial profile, rather than the $\rho_\chi \propto r^{-2}$ density distribution arising from a isothermal sphere model. Essentially, all the empirical information we have on the halo is provided by the galactic rotation curves [KK98].

Two alternative halo models can be analysed independently in order to determine the variation of ρ_χ and v_0: (a) a non-spherical (oblate spheroid) halo with no variation of the velocity distribution; (b) a spherical halo with either co-rotation or counter-rotation relatively to the motion of the Earth across the halo. These two models independently modulate the variations on the local dark matter density and the velocity distribution, respectively, and provide a conservative analysis of the uncertainties associated with the detection rates.

A) Flattened halo

The family of analytic axially-symmetric distribution functions proposed by N. W. Evans [Eva93] allows the study of the effects of flattening and bulk rotation on the halo parameters. This family of functions of the system binding energy E and azimuthal component of angular momentum L_z is described by Eq. 3.32.

$$F(E, L_z^2) = \left(AL_z^2 + B\right) e^{\frac{4E}{v_0^2}} + Ce^{\frac{2E}{v_0^2}} \tag{3.32}$$

with

$$A = \left(\frac{2}{\pi}\right)^{5/2} \frac{1-q^2}{Gq^2v_0^3} \quad ; \quad B = \left(\frac{2}{\pi}\right)^{5/2} \frac{R_c^2}{4Gq^2v_0} \quad ; \quad C = \frac{2q^2-1}{4\pi Gq^2v_0} \tag{3.33}$$

where v_0 is the circular velocity at large radii, $R_c \approx 7$ kpc is the core radius [KK98] and q is the flattening parameter. A completely spherical halo has $q = 1$, but the flattening limit for a non-negative distribution function is for $q = 1/\sqrt{2} \approx 0.707$ [KK98].

This distribution function returns a density distribution function represented in 3.34.

$$\rho(R,z) = \frac{v_0^2}{4\pi G q^2} \frac{(2q^2+1)R_c^2 + R^2 + (2-q^{-2})z^2}{(R_c^2+R^2+z^2q^{-2})^2} \tag{3.34}$$

where R is the radial distance and z is the vertical distance above the disk plane. This parametrization produces rotation curves which rise linearly at small radii and flatten at larger radii, and is therefore a valid model.

Figure 3.1 shows some isodensity contours for values of the flattening parameter of $q = 1; 0.85; 1/\sqrt{2}$ and for $R_c = 7$ kpc. For the maximum flattening parameter (bottom left image) the ratio of the azimuthal and radial axis is close to 1:2 for the galactocentric distance of our Sun, $R_\odot = 8.5$ kpc. The bottom right figure shows the halo density profiles arising from the model proposed by Evans with no flattening and no bulk velocity (blue line) and from the canonical model (black line). Both curves were obtained using Eqs. 3.34 and 3.5, respectively.

B) Co-rotating and counter-rotating halos

On the previous models there were as many particles circling around clockwise and counter-clockwise. However, the dark matter halo could have some bulk rotation either with the same direction of the circular motion of the Sun around the center of the Milky Way (co-rotation) or with the opposite direction (counter-rotation). Any rotation motion will modify the velocity distribution of dark matter particles onto a detector.

Considering the binding energy given by Eq. 3.35 [KK98],

$$E = -\frac{1}{2}v^2 - \frac{1}{2}v_0^2 log(R_c^2 + R^2 + z^2q^{-2}) \tag{3.35}$$

and using it in the distribution function on Eq. 3.32, considering the transformation to the rest frame of the Sun $v = \sqrt{v_R^2 + v_z^2 + (v_\phi + v_\odot)^2}$, one obtains:

$$\begin{aligned} f(R = R_0, z = 0) =& [AR_0^2(v\cos\alpha + v_\odot)^2 + B]\frac{e^{-\frac{2}{v_0^2}(v^2+2v_\odot v\cos\alpha + v_\odot^2)}}{(R_c^2+R_0^2)^2} + \\ &+ C\frac{e^{-\frac{1}{v_0^2}(v^2+2v_\odot v\cos\alpha + v_\odot^2)}}{(R_c^2+R_0^2)} \end{aligned} \tag{3.36}$$

The maximally co-rotating velocity distribution can be obtained considering [KK98]:

$$F_{+\odot}(E, L_z^2) = \begin{cases} F_\odot(E, L_z^2) & v_\phi > -v_\odot \\ 0, & v_\phi < -v_\odot \end{cases} \tag{3.37}$$

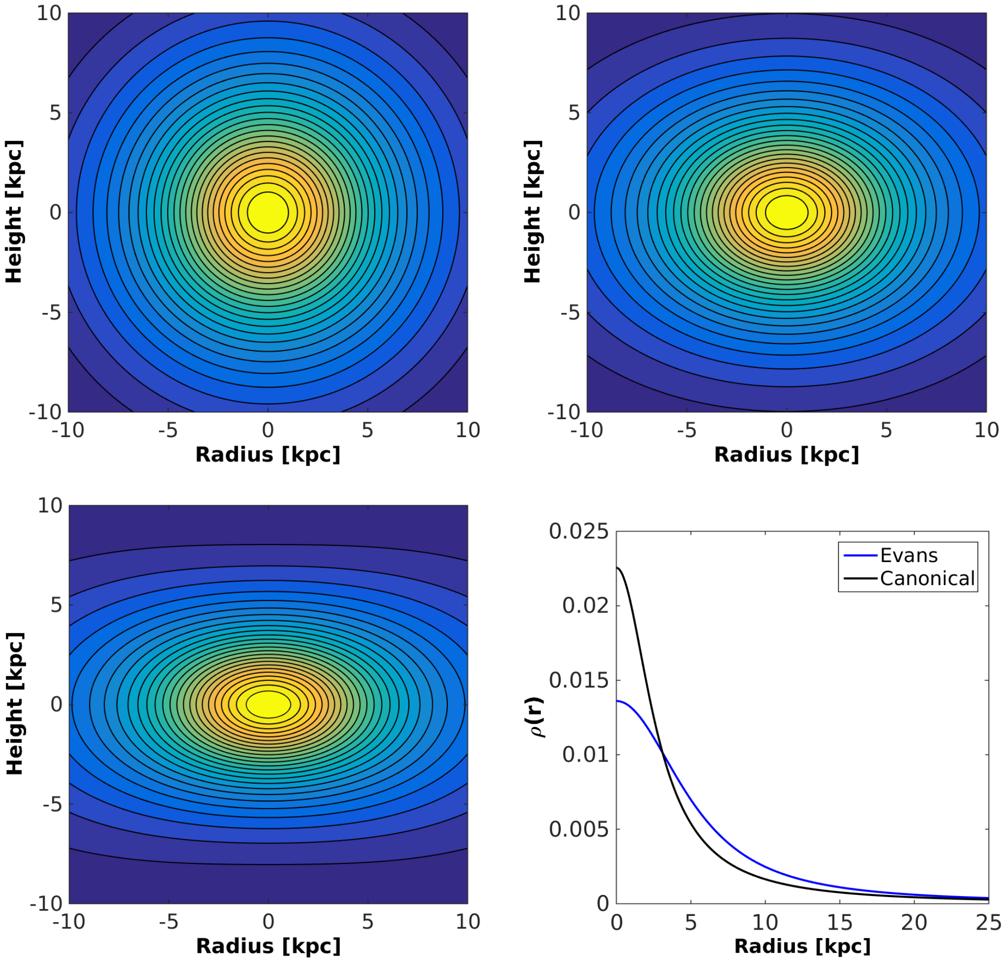

Figure 3.1: Halo isodensity contours for different flattening parameter values of the model described by Eq. 3.34: top-left) $q = 1$, corresponds to the spherical halo; top-right) $q = 0.85$; bottom left) $q = 0.707$; corresponds to the limit case of maximum flattening allowed by the model; bottom right) comparison of the normalized density profiles from the canonical halo (black line) and Evans model with no flattening and no rotation (blue line). The halo density at the location of the Sun is slightly higher in the model proposed by Evans even for a non-flattened, non-rotating halo corresponding to the top left figure.

and the maximally counter-rotating velocity distribution considering [KK98]:

$$F_{-\odot}(E, L_z^2) = \begin{cases} 0, & v_\phi > -v_\odot \\ F_\odot(E, L_z^2) & v_\phi < -v_\odot \end{cases} \tag{3.38}$$

Figure 3.2 represents the velocity distributions arising from the non rotating, co-rotating and counter-rotating models for the three values of the flattening parameter described, taken from [KK98].

These halo rotation velocities are extreme cases that allow a conservative comparison of the influences on the detection rate and recoil spectra, and are not expected to occur in the light

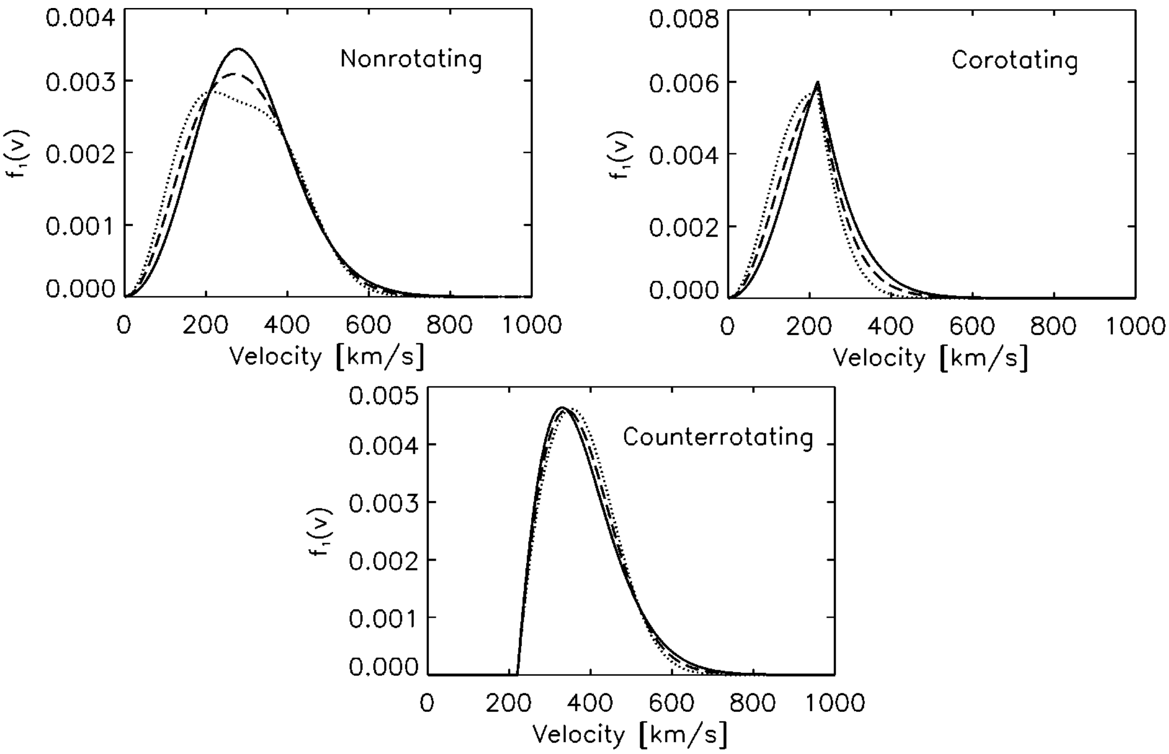

Figure 3.2: Velocity distribution functions for the non rotating (top left), co-rotating (top right) and counter-rotating (bottom) models described. The sets of curves on each plot are from considering some flattening of the halo: spherical with $q = 1$ (solid curves); flattened with $q = 0.85$ (dashed); maximum flattening parameter $q = 1/\sqrt{2}$ (dotted). Pictures taken from [KK98].

of some galactic formation models. Realistic velocity distributions should be in between these models and closer to the non rotating scenario [KK98].

3.3.1 Repercussions on WIMP detection

The plausible halo models described in Section 3.3 reproduce different results in the WIMP direct detection rates. The most significant astrophysical uncertainties in the differential event rate come from the uncertainties in the local density and circular velocity. The uncertainty in ρ_χ translates directly into an uncertainty in constraints on the scattering cross section. Different shapes of the WIMP velocity distribution vary the *time averaged* differential event rate values weakly, as these values are obtained by integration of the velocity distribution function considered [BCnG10].

A flattened halo described by an isopotential axial ratio q will provide a rise in the local WIMP density proportional, in first approximation, to q^{-1}, resulting in the same behaviour of the differential event rate. Any observational uncertainty in the local DM density translates directly into an uncertainty in the event rate and the inferred constraints or measurements of the WIMP scattering cross section [BCnG10]. The flattening does not contribute significantly to changes of the velocity distribution function, meaning that the nuclear recoil spectrum should remain practically unchanged [KK98].

Figure 3.3 represents the total event rate R as a function of the flattening parameter q for the non-rotating, co-rotating and counter-rotating halos considered, where the approximated relation $R \propto q^{-1}$ is well noticeable. The overall decrease in the rate from the counter-rotating model results from the stronger form factor suppression due to the increased average velocity of WIMP particles onto the target. The opposite effect takes place in the co-rotating halo model.

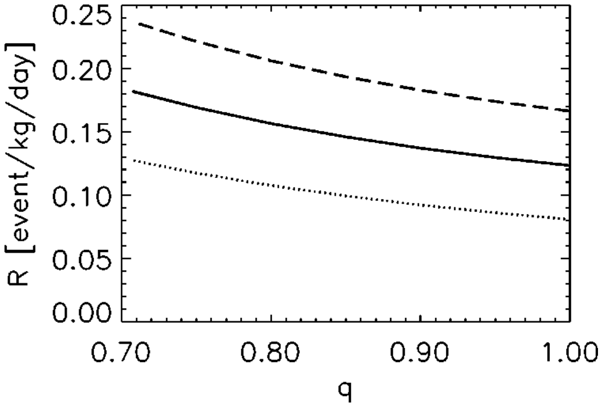

Figure 3.3: Total detection rate as a function of the halo flattening parameter for: non-rotating model (solid line), maximally co-rotating (dashed) and maximally counter-rotating (dotted). Picture taken from [KK98].

Currently there are no empirical constraints to the bulk rotation of the galactic dark matter halo. Both the maximally co-rotating and counter-rotating scenarios could affect the detection rate by ~ 40%. Maximally rotating halos should not be common according to most galactic formation models, so the contribution to the bulk rotation should not exceed ~ 10% [KK98].

Figure 3.4 shows the effect of halo rotation on the differential event rate for a halo with no flattening (left) and with maximal flattening allowed by the Evans model (right). As discussed before, the changes on the differential rate spectrum caused by flattening are minimal. These different spectral shapes allow that direct detection experiments could be used to constraint halo rotation models.

The implication of the measurements of a lower local escape velocity and higher dark matter density provided by the RAVE survey also mean that the results of direct detection experiments constraint even further the WIMP interaction cross section, up to 40% [LM15]. The results obtained by direct detection experiments would result in a best understanding and parametrization of the galactic halo by setting constraints on the parameters described here.

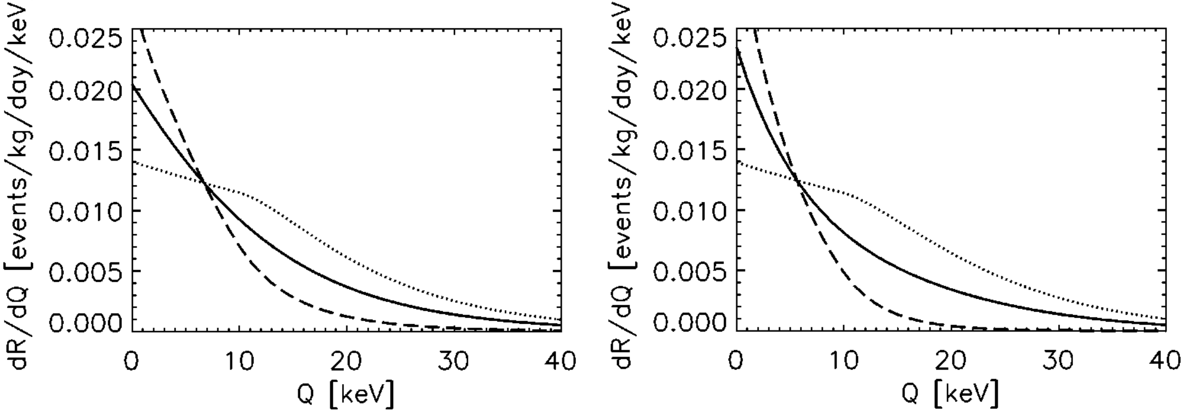

Figure 3.4: Differential detection rates as a function of the recoiling energy for different halo rotation models: non-rotating model (solid line), maximally co-rotating (dashed) and maximally counter-rotating (dotted). The left figure is for a spherically symmetric halo ($q = 1$) and the one on the right is for the maximal flattening allowed by Evans model ($q = 1/\sqrt{2}$). Pictures taken from [KK98].

Chapter 4

The Large Underground Xenon experiment

Dark matter direct detection experiments aim to probe the interaction cross section of this elusive form of matter with common baryonic matter. The Large Underground Xenon (LUX) experiment aims to clearly detect, or at least further exclude, Weakly Interacting Massive Particles (WIMPs), a leading dark matter candidate, by progressively constraining the WIMP-nucleon interaction cross section. The overall goal of the experiment is to reduce backgrounds to under 1 WIMP-like event in the fiducial volume in 300 days of running and reach sensitivities that allow probing the WIMP-nucleon spin-independent cross section down to 2×10^{-46} cm^2 [A$^+$12b]. LUX currently holds the lead in sensitivity amongst direct dark matter search experiments, discrediting some previous claims of direct dark matter detection and having established in October 2013 the world leading upper limit on the interaction cross section of 7.6×10^{-46} cm^2 at a WIMP mass of 33 GeV [A$^+$13e]. Figure 4.1 shows a plot of several experimental WIMP-nucleon spin-independent cross section limits from different dark matter experiments, where the latest LUX results are displayed. The inset in the same figure also displays some of the acceptance regions for WIMP masses from dark matter direct detection claims.

To search for WIMP dark matter, the LUX collaboration uses a dual-phase xenon time projection chamber (TPC), operated 1478 meters below the surface at the Davis Campus in the Sanford Underground Research Facility (SURF) in Lead, South Dakota. Joining the collected knowledge from several previous noble gas DM experiments [A$^+$07, A$^+$11d, A$^+$08, A$^+$12f], LUX uses a powerful technology: dual-phase setup with a liquid xenon volume to generate scintillation light and ionization charge from particle interactions and an upper-adjacent gas phase xenon region to generate electroluminescence from the ionization charges extracted from the liquid phase, drifted from the interaction site by electric fields applied on both regions, resulting in the measurement of both scintillation light and ionization charge yields. More details on the dual-phase technique are presented further.

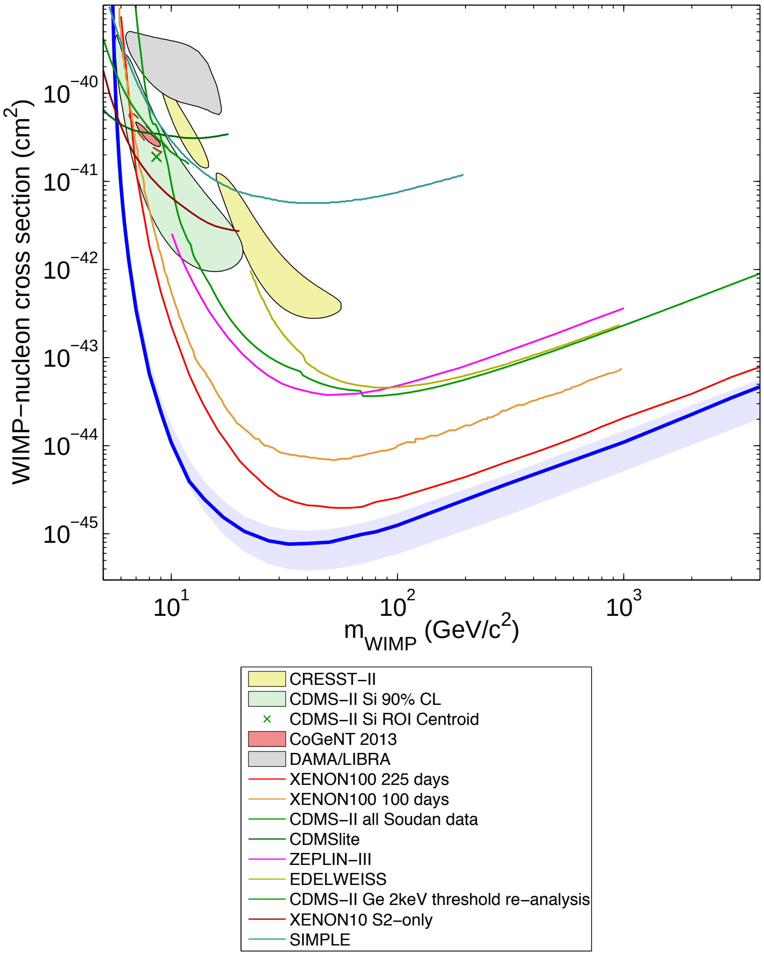

Figure 4.1: WIMP-nucleon cross section limit plot as a function of WIMP mass for several dark matter experiments. The coloured lines represent the exclusion limits obtained by different experiments, and the LUX 90% confidence limit on the spin-independent elastic WIMP-nucleon cross section is represented by the blue line. The coloured regions represent the WIMP allowed regions from several dark matter detection claims. Notice that the sensitivity of the LUX experiment has excluded most of the WIMP-nucleon cross section parameter space where the allowed regions for the claims of direct detection are defined. Figure taken from [Cha14].

4.1 Advantages of Dual-phase Xenon detectors

Dual-phase detector operation means that two separated excitation channels are recorded per interaction and a full position reconstruction of the event is possible. Figure 4.2 demonstrates how a dual-phase noble gas detector records interactions in its target by measuring primary scintillation light (S1) and secondary electroluminescence (S2) from ionization electrons being extracted from the liquid phase. If an incident particle interacts with a xenon[1] atom in the active volume, it will either excite or ionize nearby atoms, aside from energy dissipated through increase of atomic motion (heat). A diagram of the process leading to scintillation light production in xenon is shown in Figure 4.3. Excited atoms will result in the production of short-lived singlet or longer-lived triplet states of an excited dimer, Xe_2^*, when the excited atom briefly bonds with another nearby xenon atom. The de-excitation of these dimers results in the emission of a single 175 nm photon to which atomic xenon is transparent, allowing its collection using light sensors. Some of the ionization electrons produced can recombine with nearby ionized atoms, releasing more photons that contribute to the primary scintillation light, but most of the charge yield will be drifted using an applied electric field before it can recombine with a nearby ionized atom.

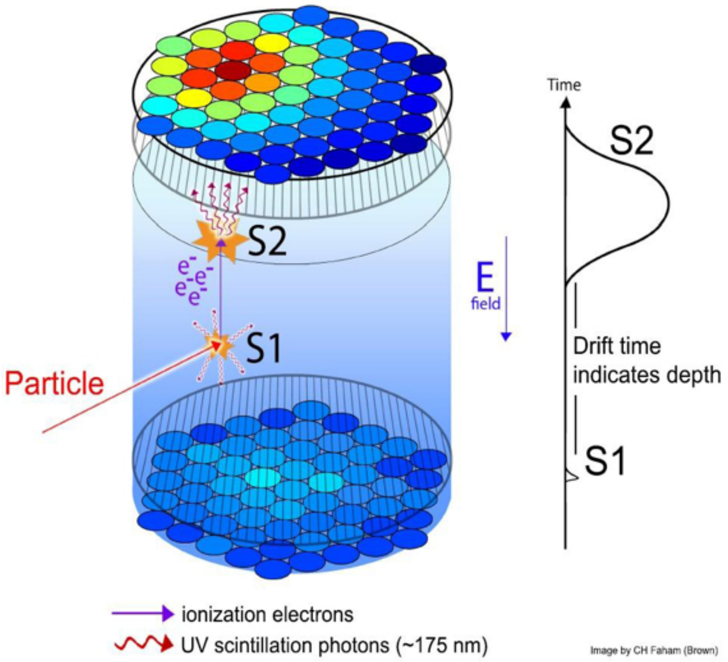

Figure 4.2: Dual-phase detector operating principle. An interaction of an incident particle with a xenon atom will produce primary scintillation light (S1) and ionization electrons. An electric field drifts these electrons across the liquid xenon volume up to the liquid/gas border where they are extracted to the gas phase through the use of a much stronger electric field, producing more light through electroluminescence (S2), as extracted electrons are rapidly accelerated in the gas. Both light signals are captured by two arrays of PMTs placed above and below the liquid xenon region. A representation of the measured S1 and S2 pulses is displayed to the right of the detector scheme. The electron drift time measured from pulse separation is a proxy to the interaction depth and the mapping of the S2 light detected (mainly) by the top PMT array can be used to reconstruct the position in the xy plane, allowing full 3D reconstruction of the event. Figure taken from [A$^+$12b].

LUX uses 370 kg of purified xenon as target. Liquid xenon has a high density, roughly 2.888 ± 0.005 g cm^3 [Ati13], higher than liquid argon or liquid neon. A high-density target is preferable mainly because a modest-size detector can enclose a substantial target mass, result in higher WIMP interaction rates. A high-density target material is also more easily scalable to a large detector.

---

[1] This technique can be implemented with other noble gases such as argon.

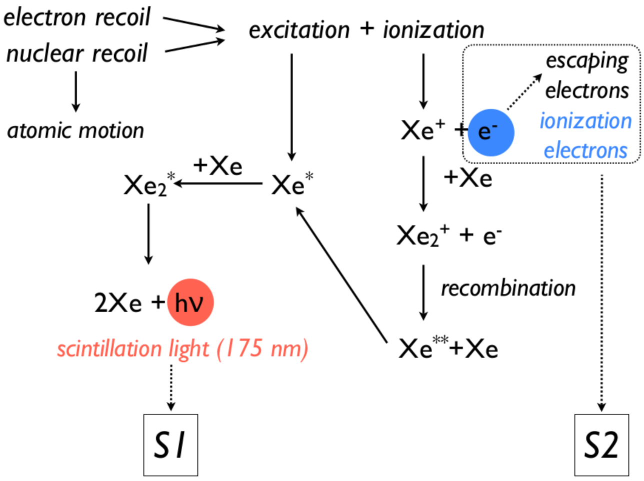

Figure 4.3: Schematic representation of the micro-processes that occur in xenon following an energy deposition, ultimately leading to the production of primary scintillation (S1) light and ionization electrons in liquid xenon. Both excitation and ionization channels can produce excited dimers. Figure taken from [MCK+10].

Another advantage in using xenon as target is its high γ ray suppression or self-shielding proprieties. As a dense liquid and with a high atomic number and mass, $Z = 54$, $\langle A \rangle = 131$, the attenuation of electromagnetic radiation in the outer layers of the liquid xenon volume is significant, resulting in a low-background region at the center. Selecting events only from the innermost region of the detector (fiducialization) helps to exclude external background events that will most likely interact in the edges of the detector.

The mass of a xenon atom, around 123 GeV averaged[2], is roughly in between the expected WIMP 10 GeV − 1 TeV mass range and close to the most promising mass value of 100 GeV for a relic weakly interacting particle[3]. The WIMP interaction rate depends on the relation between WIMP mass and target mass, being maximum when both mass values are identical. Therefore xenon provides a rather heavy target nucleus when compared to dark matter experiments using germanium or argon[4], making it more sensitive to the heavier WIMP sector.

Natural xenon has 9 isotopes, 8 stable and the unstable ^{136}Xe with a long half-life of $T_{hl} = 2.11 \pm 0.04_{stat} \pm 0.21_{sys} \times 10^{21}$ yr that decays through $2\nu\beta^-\beta^-$ emission [A+11a]. The relative abundance of ^{136}Xe in natural xenon is around 9%, meaning that natural xenon has a very low radioactive content and will not contribute significantly to LUX intrinsic backgrounds. Argon, however, has an intrinsic unstable isotope, ^{39}Ar, with a half-life of 269 years that makes it a main internal background source in argon-based detectors. Xenon used in LUX was chosen from purified batches that had low impurity levels. Impurities mixed in xenon reduce electron drift

---

[2] Averaged by the relative abundance of xenon isotopes.

[3] CMB constraints on the thermal WIMP annihilation cross section result in a value of $\langle \sigma v \rangle_{DM} \approx 4 \times 10^{-26}$ cm^3 s^{-1}, which is roughly the expected for a thermal relic particle in the $\sim$ 100 GeV mass range that interacts via the electroweak force [Ste15].

[4] Germanium atoms have masses of $\sim$ 68 GeV and argon atoms $\sim$ 38 GeV.

length by absorbing free electrons and result in ionization charge loss, and to minimize this a heated getter purification system is used to remove electronegative and molecular impurities [A+12b]. This system, however, cannot remove noble gas impurities like krypton or radon mixed in xenon. Natural krypton has the unstable isotope ^{85}Kr with concentrations of 20 ppt, and so, to reduce krypton related backgrounds a different method for removing noble impurities was implemented and is explained in more detail in Section 4.3.

Several other characteristics including high electron mobility - around 842 cm^2 V^{-1} s^{-1}, high scintillation yield and shorter lifetime of xenon excitation states also provide an advantage to xenon-based detectors compared to the performance of argon or neon [Sch10]. Also, scintillation light from xenon has a 175 nm wavelength, compatible with some PMTs wavelength sensitivity, allowing good light collection efficiencies, an essential feature in liquid noble element detectors which tend to produce fewer light quanta for low-energy interactions when compared to ionization and phonon yields of semiconductors. Liquid xenon typically yields around 42 scintillation photons per keV deposited energy [Sch10], which is high compared to other scintillation materials typically used, but ionization and phonon yields tend to be greater in semiconductor-based detectors, around 10^2 and 10^4 quanta per keV, respectively [Sch10].

4.2 Detector Internals

The information presented in this Section was taken from reference [A+12b], unless mentioned otherwise. Specific details and further information on the detector components can also be found in the mentioned reference.

4.2.1 Cryostat Vessels

The LUX detector has two cylindrical cryostat vessels made of 0.223″ thick titanium sheets [A+11c] where the xenon target and detection components are placed. The outer vessel is placed inside a 7 ton water tank, held by a steel cryostat stand, and houses the inner vessel in a vacuum for thermal insulation. The inner vessel holds all the internal detector components: the top and bottom copper radiation shields, the top and bottom PMT arrays and copper mounts, field shaping rings and High-Density Polyethylene (HDPE) supports, field grids and steel supports and polytetrafluoroethylene (PTFE) light reflecting sheets. Also, several sensors are placed inside the detector for monitoring, including level sensors, thermometers and calibration instrumentation. Figure 4.4 presents a visualization of LUX detector in the water tank and a detail of the titanium vessels and internals.

The inner vessel hangs from the upper dome of the outer cryostat, attached and insulated with plastic hangers, and has 61.6 cm in diameter and 100 cm height, with a dome welded to the bottom and a 70.5 cm flange welded to the upper rim, where flexible steel couplings enter the cryostat. This vessel encloses the main detector component, the dodecahedral PTFE-surrounded liquid xenon target, where dark matter interactions are to be recorded.

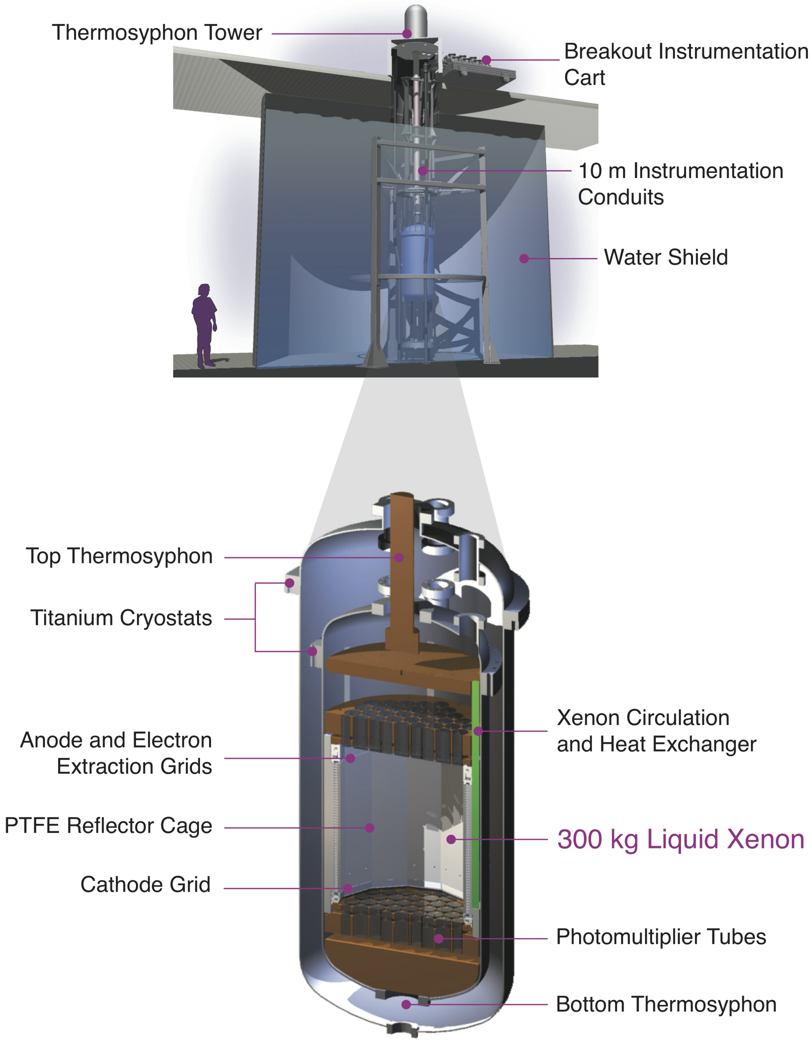

Figure 4.4: Schematic view of the LUX detector. The top figure shows the layout of the detector in its stand inside the water tank, also displaying the thermosyphon tower used for cooling and a human for scale. The bottom figure shows a longitudinal cut of the cryostat vessels and internals, where both vessels, copper radiation shields, PMT arrays, reflector sheets and thermosyphon couplings can be seen. The space between cryostat vessels is kept in vacuum to ensure proper thermal insulation of the inner vessel and liquid xenon.

Two thermal and γ radiation shields are placed on the top and bottom extremities of the inner cryostat to supply further radiation shielding from γ rays coming from the Davis Campus rock floor below the water tank and from the rock above. The top shield is s 5 cm thick, 55 cm diameter copper disk mounted directly in the inner vessel top flange and thermally coupled to the cold-head of a large capacity thermosyphon. The remaining components are supported by six titanium straps attached to the top copper shield.

The two PMT arrays are composed of 61 Hamamatsu PMTs each, supported by a copper structure like the one presented in Figure 4.5. The top PMT array mount is 15 cm below the top thermal shield and together with the bottom PMT array and the 12 light reflective PTFE sheets, encloses the main liquid xenon volume. The bottom PMT array is mounted 60 cm below the top PMT array in a structure similar to the top PMT mount, and below this structure is the 15 cm thick copper shield that fills the bottom cryostat dome and is used to provide additional radiation shielding and to displace inactive xenon. The bottom thermosyphon is thermally connected to this shield to best control the temperature gradient inside the detector. This shield and the bottom PMT mount can be seen in Figure 4.5. The 12 reflective sheets between the PMT mounts are held in place by slotted holes to allow thermal dilation and contraction. All the inner cryostat components were designed to minimize the amount of thermal stress as possible from 310 K to liquid xenon temperatures of 175 K.

To maintain the inner vessel at cryogenic temperatures, four thermosyphon cold heads are used. Each thermosyphon consists of a vertical sealed tube filled with nitrogen gas (N_2) with a condenser at the top immersed in liquid nitrogen (LN), an evaporator (cold head) at the bottom, connected to the detector, and a passive steel line connecting the two ends. The N_2 that condenses inside the condenser at the top flows downward in the steel line with the help of gravity and reaches the cold heads where it evaporates, removing heat from the detector. As it evaporates it ascends in the lines towards the condenser. A large thermosyphon is attached to the top of the inner vessel and thermally coupled to the copper shield and a smaller thermosyphon is attached to the bottom of the inner vessel also thermally coupled to the bottom copper shield. These two thermosyphons are responsible for cooling the detector from room temperature to 175 K. The remaining two cold heads are attached to the copper thermal shield surrounding the inner vessel and help maintain a temperature gradient across the height of the detector.

Nine level sensors are used to ensure and maintain the verticality of the detector and the liquid/gas border aligned and stable. Tree level rods placed in the cryostat stand allow fine alignment of the detector. The width of the S2 pulses increases with the thickness of the xenon gas layer above the liquid surface: if the detector is not levelled properly this distance is not uniform and the S2 signal will not be uniform across the $x - y$ plane of the detector. Temperature is monitored by 40 thermometers in the xenon space in order to be maintained as constant as possible at 175 K and minimize temperature gradients. Other 23 thermometers monitor the cryostat vacuum space and the temperatures of the various thermosyphon components.

4.2.2 Grids and Field-shaping Rings

Drifting ionization electrons across the active region is done by applying an electric field across the liquid xenon. The extraction of these electrons into the gas phase in order to produce electroluminescence is done by applying a stronger extraction field in the gas-liquid interface. The drifting and extraction electric fields are produced by a total of three wire grids, while the remaining two act as a protection for the PMT photocathodes.

The bottom grid is placed 2 cm above the bottom PMT array and its main function is to protect the PMT photocathodes from the high-voltage of the cathode grid, zeroing the field at PMT level, and to produce reverse field regions to suppress S2 signal from interactions in these regions. This grid has an open area ratio of 98%. The nominal operating voltage usually applied to this grid is -2 kV.

The cathode grid, located 4 cm above the lower grid, is responsible for the high voltage required to produce the drifting electric field across the active region. This grid is similar in construction to the bottom grid, but with the steel wires spaced 5 mm from each other, resulting in an open area of 96%. In order to produce a drift field of 182 V cm^{-1} used during the WIMP search run, the nominal operating voltage for the cathode grid is -10 kV. The xenon volume between the cathode and the bottom PMT bank is called the "reverse field region" where no ionization charge can be drifted to the extraction region, and thus no S2 signal is produced, due to the reversed electric field imposed by the bottom grid. Interaction events in the reverse field region still produce S1 scintillation signal that is measured effectively in the nearby bottom PMT array.

Around 49 cm above the cathode grid, and just $\sim$ 5 mm below the liquid/gas border, the gate grid works with the cathode to produce the drift field and with the anode grid to generate the strong extraction field across the liquid xenon surface. It has a 99% open area, and variations of the extraction field across the liquid surface are smaller than 1%. During the WIMP search run, a voltage of -1.5 kV was applied in this grid. The volume of liquid xenon between the cathode and the gate grid is called "active region", with calculated 250.9 ± 2.1 kg of xenon [Sil15] and where event reconstruction is possible with S1 light plus S2 electroluminescence signals being produced and detected. Because of the regular vertical direction of the drift field, the ionization electrons maintain most of the interaction vertex $x-y$ position and form a narrow bulk as they are being drifted.

The anode grid sits $\sim$ 5 mm above the liquid/xenon border and 1 cm above the gate, with which it generates the extraction field to produce electroluminescence by the ionization electrons drifted in the active region. This grid has an open area of 88% and a typical voltage applied of 3.5 kV in order to generate an extraction field of 3.1 kV cm^{-1} in the liquid and 6.0 kV cm^{-1} in the gas, producing a best-fit electron extraction efficiency of 0.65 ± 0.01 [A^{+}13e]. The region between the anode and the liquid surface is called "extraction region" or "S2 region" because it is in this thin layer of gas that the extracted electrons produce the secondary scintillation, with approximately 25 S2 photoelectrons generated per extracted electron.

Finally, the top grid located 4 cm above the anode grid and 2 cm below the top PMT array is similar in geometry to the bottom grid, but with an open area of 99%, crucial to minimize the optical obstruction of the S2 light. The function of this grid is to shield the photocathodes of the top PMT array from the high-voltage of the anode, like the bottom grid does to the bottom array.

Around the active region of the detector, 48 copper field shaping rings are spaced uniformly to minimise irregularities of the electric field. These rings are placed 1 cm apart from each other outside the PTFE reflectors, held together by HDPE supports. Placement and thickness of the rings was chosen to provide the most uniform drift field possible and to shield the region from the electric field produced by the cathode HV cable. The voltage of the field rings is managed with the use of a resistor chain attached to all field rings and to the cathode and gate grids. The top ring is connected to the gate grid by two parallel 0.875 GΩ resistors, while the bottom field ring is connected to the cathode by two 1.25 GΩ resistors and each individual ring is connected to its neighbours by parallel pairs of 1 GΩ resistors.

4.2.3 PMT arrays and Light Reflecting Cage

The LUX detector has two arrays of 61 Hamamatsu R8778 Photomultiplier Tubes (PMTs) each, at the top and bottom of the liquid xenon active region[5]. Both arrays are mounted in large high-purity copper structures as the one showed in Figure 4.5. The bottom array is placed below the cathode grid, with the windows of the PMTs 2 cm below the lower grid, and measures most of the S1 scintillation signal due to internal reflections in the liquid surface. The top array is in the gas phase, above the liquid, and collects a major fraction of the S2 electroluminescence, being used for $x - y$ position reconstruction using likelihood pattern recognition developed for ZEPLIN-III [S^{+}11]. With these techniques, a $x - y$ position reconstruction accuracy of order 1 cm (20% of the PMT diameter) is obtained. The drift time obtained from the time separation of the S1 and S2 pulses, that can be converted to depth in the LUX detector active region. As the primary scintillation light reaches the PMT arrays instantly and the drifting electrons move at 0.15153 ± 0.00109 cm μs^{-1} across the liquid xenon in a 180 V cm^{-1} drift field [Sil15], delaying the S2 electroluminescence signal.

The 12-stage, 5.7 cm diameter Hamamatsu R8778 PMTs were developed in collaboration with XMASS specifically for operating in liquid xenon conditions, at temperature of 170 K and pressures up to 5 atm. Being sensitive to the 175 nm xenon scintillation light, the 15.9 cm^{2} photocathode has typical quantum efficiencies (QE) of 33% at that wavelength.

Additionally to the 12 PTFE reflective plates enclosing the sides of the active volume and the gas phase, the surfaces between PMT windows are also covered with PTFE reflector pieces (aka “trifoils”) to optimize scintillation light collection. This means that the active region is surrounded in 4π by high-reflectivity material and PMTs, increasing the light yield by up to a factor of 5 when compared to using only lateral reflective plates.

---

[5] The active region being the liquid xenon volume enclosed in the PTFE reflectors and between the cathode and the “gate” grid, separated by 48.32 ± 0.32 cm and 250.9 ± 2.1kg [Sil15].

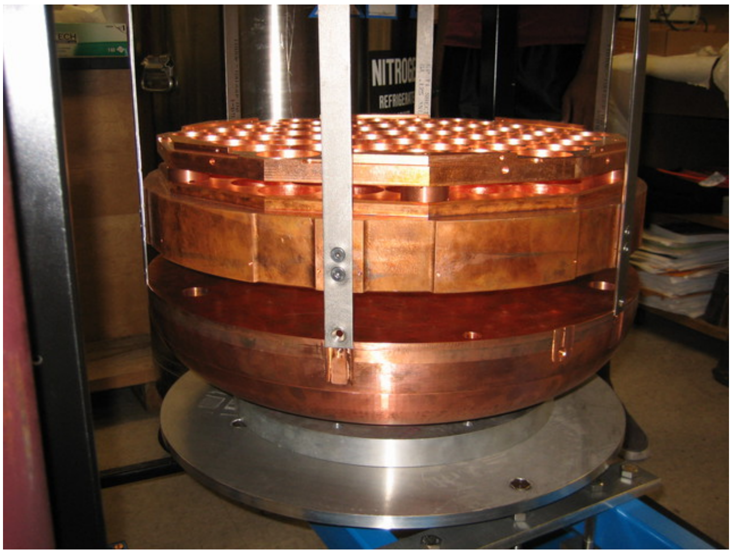

Figure 4.5: Bottom PMT holder (copper structure with PMT sockets) on top of the dome-like lower γ radiation shield. The six titanium strips that hold the entire inner structure together are also visible. Figure taken from [Fah12].

The light collection efficiency in LUX during the WIMP search run is estimated at 8.8 phe/keV$_{ee}$ at zero-field [A^{+}13e]. The reflectivity of the PTFE panels was determined to be $> 95\%$ in liquid xenon and photo absorption length of the scintillation light in that medium is at least 5 m. These values were obtained through Monte Carlo simulations.

The PMTs are also one of the main sources of γ ray background. A more detailed description of the PMT contribution to the LUX background rate is presented in Section 5.6.

4.3 Background Reduction and Discrimination in LUX

The biggest challenge of any dark matter direct detection experiment is to minimize background events to allow a spectrum of rare neutron recoils (NR) events from dark matter interactions to be observed. The three main ways of excluding backgrounds are shielding the detector, the use of low-radioactivity materials and the development of background rejection analysis techniques.

The backgrounds consist of electron recoils (ER) - primarily from γ rays - and nuclear recoils from neutrons. The most challenging background comes from neutron NR interactions that mimic WIMP signal. As neutrons have great penetration power and generate NR in the expected WIMP recoil energy range, they are impossible to distinguish from dark matter interactions from energy deposition and excitation channel relations analysis. ER events in LUX arise mainly from radioactivity within construction materials (naturally occurring or from cosmogenic activation), cosmogenically activated xenon isotopes and intrinsic radioactive isotopes mixed in xenon. Radioactivity from the surrounding materials (rock, laboratory, construction materials, etc.) are not as important because of the radiation attenuation provided by the water tank where the LUX detector is immersed, as it is explained further (see Figure 4.4).

Low-radioactivity materials

The LUX detector was built with radio-pure materials to minimize intrinsic background sources. Most of the mass of the detector, excluding that of xenon, is from copper mounts and shields and from the titanium vessels and holders. All these structures are adjacent to the active region and any radioactive content in them potentially results in background events. In order to minimize these background sources, all copper and titanium used in construction, as well as stainless steel from other inner structures, is selected from top-grade ultra-pure batches. Details of the radioactivity screening of these materials is presented in Section 5.6.1 and in reference [M$^+$14].

The xenon used in LUX was also selected for containing very little radioactive content and impurities. All xenon was extensively purified in order to reduce impurities that would compromise charge yield collection. Furthermore, in order to reduce the ^{85}Kr content in xenon, a chromatographic separation technique was implemented with the objective of reducing the natural krypton content to concentrations < 4 ppt, lowering the background rate due to ^{85}Kr. A column of activated charcoal is used to chromatographically separate krypton and xenon due to their very different adsorption constants [BBS$^+$07] thus reducing krypton levels by an average factor of 3×10^4 and to concentrations of 4 ppt.

Cosmogenical activation of construction materials

Radioactive activation of construction materials and xenon due to storage above ground resulted in activated unstable isotopes being present in almost all detector components. Also, the altitude of the Sanford Surface Laboratory, roughly 1600 m above sea level, leads to substantial cosmogenic muon flux of around 55 m^{-2} s^{-1} [GGRZ04]. This flux of particles generated by interaction of energetic cosmic rays with the atmosphere can induce spallation neutrons with high energies and great penetration power, that can activate atoms of some materials. Copper structures stored at high altitudes suffer activation and consequently have some ^{60}Co content that has a non-negligible half-life of 5.3 years [C$^+$10]. In the case of titanium, activation through muon capture and neutron spallation channels produces ^{46}Sc with an half-life of 84 days [A$^+$11c]. Both ^{60}Co and ^{46}Sc decay modes can generate ER backgrounds, with emission of two MeV scale simultaneous γ rays capable of reaching the inner xenon volume.

Activation of xenon through muon-induced neutron flux resulted in the production of ^{127}Xe, ^{129m}Xe, ^{131m}Xe and ^{133}Xe, with half-lives spanning from 5.3 to 36 days, being one of the main backgrounds for the 85.3 WIMP search run, as explained in detail on Chapter 5.4. By moving the detector underground the activation of xenon ceased and all these isotopes slowly decay away, but the small time interval between underground deployment and data acquisition for the WIMP search run was not enough to reduce some of these isotopes to negligible concentrations. The length of time between xenon activation interruption and the beginning of the WIMP search run was 83 days, just over two half-lives of the isotope ^{127}Xe, $T_{hl} = 36$ days. Therefore, the first half of the WIMP search run had considerable background rates due to this isotope, becoming less prominent throughout the run. The contributions from other xenon activated isotopes became insignificant early on the WIMP search run.

Underground deployment

Cosmic particles constantly irradiate the atmosphere of the Earth. Electromagnetic showers from cosmic rays generate high energy muons with incredible penetration power. Upon interaction these particles can generate spallation neutrons in hadron showers. The muon flux on the surface of the planet varies with altitude due to atmospheric attenuation. At Sanford Lab altitude (Lead, SD) the muon flux is thought to be around 55.2 m^{-2} s^{-1} [GGRZ04]. The 1.478 km of rock of the Homestake mine above the detector correspond to 4.3$\pm$0.2 kilometre-water-equivalent (km·w·e), reducing the muon flux by seven orders of magnitude. The estimated muon flux at the Davis Campus level is (4.4$\pm$0.1) 10^{-5} m^{-2} s^{-1} [MH06], rendering radioisotope activation negligible and making the muon-induced neutron background secondary when compared to other background sources. The neutron flux from the natural radioactive content of the rock at Homestake mine is expected to be (0.55 ± 0.01) 10^{-5} m^{-2} s^{-1} [M^{+}14]. Construction materials used in LUX can also produce neutrons from (α,n) interactions and from spontaneous fission of ^{238}U that are generated in the areas adjacent to the active region and can produce WIMP-like NR events. The internal and external neutron background rates are comparable and consist a sub-dominant NR background in LUX [M^{+}14].

4.3.1 Muon Veto System

The LUX detector is immersed in a 7.6 m diameter, 6.1 m high water tank to provide shielding from ambient radiation. The water tank with the immersed detector is schematically represented in Figure 4.4. Water shielding is preferable than lead and polyethylene shields, previously used typically in dark matter detectors, at stopping radiogenic neutrons and fast neutrons from muon interactions with the cavern walls, specially due to the density of water, higher than typical polyethylene, and because the hydrogen atoms in water molecules, with a high neutron interaction cross section ($\sim$ 20 barn) to sub-MeV neutrons, causing these particles to deposit most of their energy in a collision. Water is also a good γ ray shield, attenuating $\sim$ 50% of γ ray flux of energies lower than 2 MeV in a $\sim$ 15 cm thickness. Comparable to other common shielding materials, water is very cost-competitive, abundant and provides great flexibility in detector scaling and shaping. The LUX-ZEPLIN detector (LZ) [A^{+}11b], a next generation dark matter experiment that uses the collective knowledge of the LUX and ZEPLIN collaborations, will be implemented in the Davis Campus using most of existing structures of LUX, including the water tank for shielding.

With LUX, the 265 m^{3} of water provide a minimum shielding thickness of 2.75 m on the top, 1.20 m at the bottom and 3.50 m at the sides. Additional shielding is also provided by 20 tonnes of low-radioactivity steel plates arranged in an inverted pyramid configuration below the water tank, with a maximum thickness of 31 cm, to attenuate γ ray flux from the cavern rocks. This amount of shielding material renders external radioactive background sources negligible compared to internal detector sources.

The cryostat vessels are anchored to the bottom of the water tank using a metallic frame (cryostat stand) that provides stability and support. The tank is sealed after the installation of the detector and nitrogen gas is poured on the top of the water to purge radon gas. The water is purified to reduce uranium, thorium or potassium impurities that could generate high energy radiation close to the detector [A^+12b].

Within the water tank, a muon tagging system is mounted as an anti-coincidence background rejection mechanism. A total of 20 Hamamatsu R7081 25.4 cm diameter PMTs with a curved window for stereographic light collection are placed inside the tank, arranged in four vertical lines around the walls with 4 PMTs each spaced evenly and detached 25 cm from the walls. Four additional PMTs are placed on the bottom of the tank, adjacent to each PMT line and spacing 50 cm from the edges of the tank. The walls are covered with Tyvek reflectors to optimize light collection. An energetic muon that passes through the water surrounding the detector will emit Cherenkov radiation that can be collected by the surrounding PMTs. If the striking muon produces an electromagnetic shower the light yield will be greater and will easily be picked up by the sensors. Any background event, specially NR, inside the detector that occurred in coincidence with this muon detection can be excluded, thus vetoing any muon-related neutron signal in LUX.

4.3.2 Background discrimination

Fiducial volume

Taking advantage of the great self-shielding proprieties of liquid xenon, a good background exclusion technique is to exclude events beyond a certain distance from the quiet center of the detector. A detector with good position reconstruction such as LUX can exclude an event based on its position. By defining a fiducial volume in the target and only accepting interior events, most of the background events generated outside the target volume, more likely to interact closer to the edges of the detector, are discarded. In practical terms the detector will only have a fraction of its target material as the real target, because if a WIMP interacts outside the fiducial volume it will also be discarded. This technique takes advantage of the disparity of the interaction cross section of dark matter and that of a γ or β. A WIMP interaction is very rare, and being so means that WIMP interactions are expected to be uniformly distributed throughout the entire volume. Electromagnetic interactions, however, have rather large cross sections and a γ ray has a high probability of interaction in the first few centimetres of xenon. A fiducial volume with 118.3 ± 6.5 kg, defined between $38 - 305$ μs drift time (corresponding to $70 - 470$ mm above the cathode grid) and with a radial cut of 18 cm, was set during the WIMP search run [A^+13e]. These fiducial limits were defined with the help of Monte Carlo simulations, to best exclude γ rays from the PMTs and radon daughter related NR from the walls while maintaining a substantial target mass.

Electron and Nuclear recoils

A WIMP is expected to interact only with the nucleus of an atom, producing a nuclear recoil. The electron cloud of an atom should be completely transparent to a chargeless massive particle such as WIMPs and the only interactions that produce electron recoils are from background sources: mainly γ rays and β particles.

A NR event has a different topology than that of an ER event. NR produces a much shorter (μm size) energy deposition track, as the nucleus and the entire atom recoils, and the energy deposition is thus denser than that from an ER track.

Another difference in ER and NR event topologies is the scintillation and ionization charge yields. An ER event generates a total amount of quanta (scintillation light and ionization electrons) proportional to the total energy deposition [SD11]. In a NR event, a fraction of the deposited energy goes to atomic motion and is lost as heat [Sch10]. In both cases the partitioning between scintillation and charge quanta is energy dependent, as seen in Figure 4.6. If electrons are not drifted from the interaction site, recombination with xenon ions results in charge loss and more scintillation, meaning that the partitioning also depends on the strength of the applied electric field.

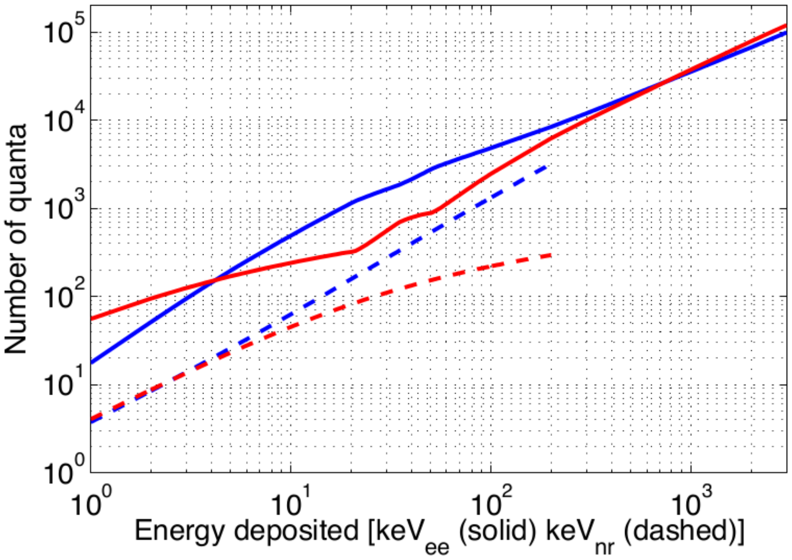

Figure 4.6: Number of detectable scintillation photons (blue) and ionization electrons (red) generated for ER events (solid lines) and NR events (dashed lines) as function of energy deposition in liquid xenon. The NR events have significantly lower light and ionization yields than ER events to the same deposited energy. At lower energies an ER event preferentially generates more ionization charge than scintillation, while a NR creates approximately the same amount. These differences allow ER/NR discrimination when S1 and S2 signals are analysed. Data obtained through the Noble Element Simulation Technique (NEST). Figure taken from [Mal14].

As the observable quanta produced differ greatly for the same energy deposition, it is important to define the energy scale used to reconstruct an event. The energy scale for ER events is denoted keV$_{ee}$, where the subscript stands for "electron-equivalent", representing the energy deposited by an electromagnetic process. For NR events the energy scale is denoted by keV$_{nr}$, where the subscript stands for "nuclear recoil", and refers to energy deposited through a recoiling nucleus.

A very powerful method for discriminating ER from NR events is to analyse the pulse areas for S1 and S2 signals, proportional to scintillation and ionization, respectively. The relation between S2 and S1 yields as a function of S1 signal allows for the separation of ER and NR in two distinct bands, as shown in Figure 4.7 for the LUX detector. The acceptance window for WIMP-like events in this analysis is defined by energies between $3.4-25$ keV$_{nr}$, or $0.9-5.3$ keV$_{ee}$, and a profile likelihood analysis to the measured event distribution profile in the $S2/S1$ ratio over $S1$ parameter space is used to search for WIMP interactions by comparing with the expected profile for different models of WIMP mass. This technique excludes ER events with an expected efficiency for LUX of $(99.8 \pm 0.1_{sys})\%$ for events between $2-30$ photoelectrons (phe) and considering a background-only model [Col15a].

In addition to γ and β, α particles also constitute a background. As α particles generated from radioactive decay tend to have energies of several MeV and deposit their energy in a very dense track due to their charge, the S1 signal observed is from 4×10^4 to 9×10^4 phe. Typical γ ray events read up to only 1.5×10^4 phe, much lower than α events, meaning that α particle interactions are easy to identify as background. Because of that, no α event is expected to fall in the WIMP search energy window because of the large energy depositions involved.

Single and Multiple scatters

Aside from shielding the detector as best as possible with neutron shielding materials, dark matter experiments rely on multi-scattering (MS) discrimination to exclude neutron interactions in the active volume. If two or more energy depositions within LUX ms time window generate two separated S2 pulses for one S1 pulse, differentiable by distinct drift times or $x-y$ position reconstruction from PMT hit maps, the event is tagged as a multiple scatter.

Neutrons generated from spontaneous fission and (α,n) interactions in construction materials, with energies in the scale of MeV, have a mean free path of order 10 cm in liquid xenon. Most of these fast neutrons incident in the 49 cm diameter detector will produce MS events that are tagged as background and therefore excluded. Ultrafast muon-induced neutrons, with energies in the scale of GeV, can potentially generate single scatters due to their long mean free path in liquid xenon, much longer than the size of the detector, and so reducing the muon flux by seven order of magnitude by moving the detector to a depth of 1478 meters is crucial to prevent muon-induced neutron interactions [M$^+$14].

The external radiogenic neutron flux on the LUX detector is estimated in 10^{-16} n per year, expected to produce an estimate ratio of 13 MS events per SS event, which corresponds to an upper limit of 0.37 SS events in the WIMP search run conditions. The expected muon-induced neutron flux at the LUX outer cryostat is 6.3×10^{-7} n s^{-1} - corresponding to roughly 120 nDRU, or ~ 0.1 WIMP-like NR events in a year, in the $3.4-25$ keV$_{nr}$ energy range and in a 100 kg xenon volume. The total neutron background rate from internal and external sources, namely muon-induced and environmental, is estimated to be 350 nDRU for a one year run [M^+14].

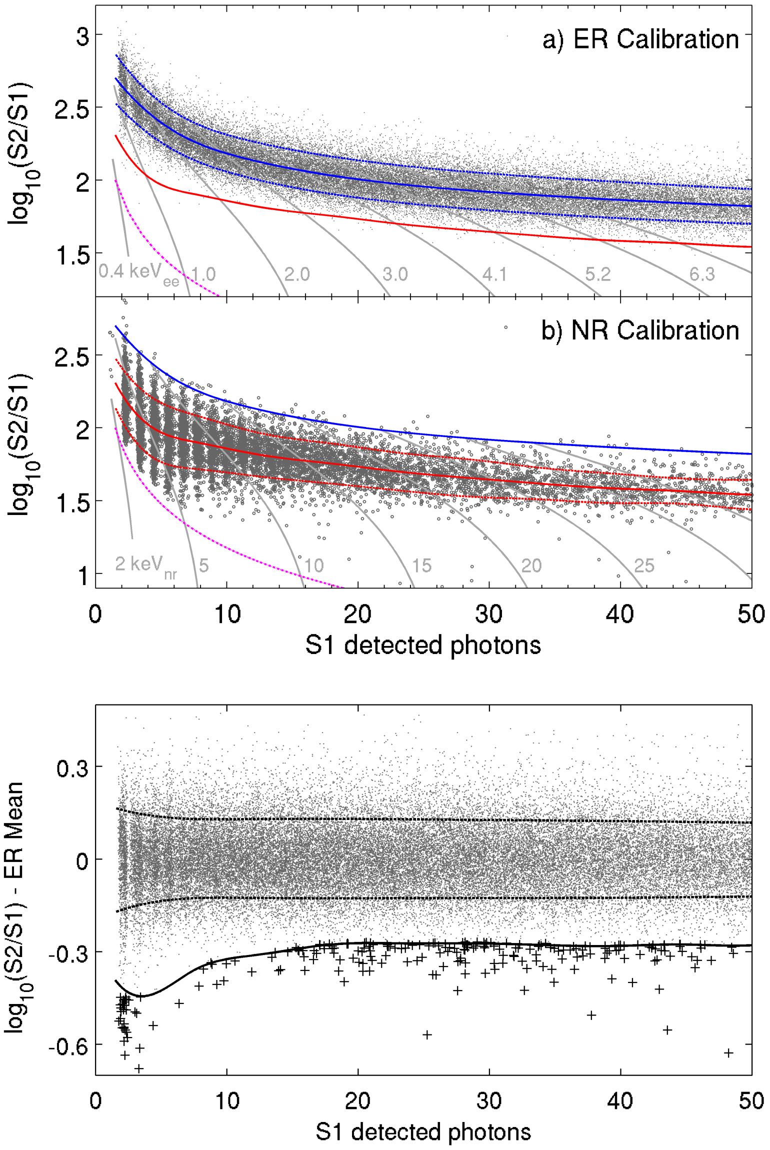

Figure 4.7: Calibration of the LUX detector response in the 118 kg FV. The ER calibration was performed using a tritium source and is shown in the top panel, while the NR calibration, displayed in the middle panel, was performed using a mono-energetic neutrons from a *DD* generator. The dashed lines around each band mean indicate the $\pm 1.28\sigma$ contours (red lines for NR and blue lines for ER). The dot-dashed magenta line represents the S2 threshold applied in the analysis. The bottom panel represents the $log(S2/S1)$ normalized to the mean of the ER band as a function of S1, emphasizing the leakage of ER events (plotted with a plus sign marker) below the NR mean (solid line). Figure taken from [Col15a].

Chapter 5

Backgrounds in LUX

As with all low-background experiments, the main concern in LUX is to minimize unwanted events that could either mask or mimic the signal to be detected. LUX is a fine example of a ultra-low-background, high-sensitivity experiment where rare WIMP events could be observed, leading the sibling dark matter experiments in sensitivity and background rates [A^{+}13e]. To be able to separate the rare nuclear recoil (NR) signatures arising from the extremely low WIMP interaction rate, a precise control of unwanted interactions within the active volume of LUX is of the utmost importance. A complete background analysis was performed and all main backgrounds were extensively simulated [M^{+}14].

WIMP interactions are characterized as single scatter (SS) events and their probability distribution is uniform within the target volume and within the WIMP signal energy range of $3.4 - 25$ keV for a nuclear recoil. It is expected that a WIMP particle, if it interacts with the target, only scatters once in the relatively small volume due to their weakly interacting nature. Any other events recorded in the same conditions would limit the sensitivity of the experiment. Efficient background discrimination techniques are crucial to exclude the unwanted events that are not suppressed. To reject low-energy ER events that fall inside the WIMP search energy range ($0.9 - 5.3$ keV for electron recoils), LUX relies on differences in ionization and scintillation yields from NR and ER events. This method results in good ER discrimination as proven by the ZEPLIN-III experiment, that obtained an efficiency in ER/NR discrimination from analysis of scintillation and ionization yields of 99.99% [A^{+}07]. Only by limiting the unwanted signals and achieving good background discrimination is it possible to improve the sensitivity of the detector and filter the extremely rare WIMP nuclear recoil signatures to be detected.

The main background sources within LUX produce low-energy electron recoil (ER) signatures in the xenon target, via electromagnetic interactions from photons or electrons. Due to differences in xenon scintillation and ionization yields, the $3.4 - 25$ keV$_{nr}$ energy window for NR translates to a $0.9 - 5.3$ keV$_{ee}$ energy range for ER, where the “ee” index denotes the energy scale for ER events. The neutron background signatures are indistinguishable from WIMP events because neutron interactions produce NR events in the WIMP search energy window. The suppression of neutrons from environmental radioactivity and muon interactions is of the utmost importance.

In this work only internal backgrounds[1] that produce ER events in the WIMP search energy window were analysed, excluding those of cosmic and environmental origin like muon-induced neutrons. These main radiogenic backgrounds include cosmogenic-activated xenon-127, radon from the exposure of internal components to the atmosphere, krypton-85 mixed with the xenon and γ rays from construction materials and PMTs.

The background rate for a specific source is usually presented in Differential Rate Units (DRU), or the number of events per kilogram of detector material per keV per day of exposure.

---

[1] By far the most important, due to suppression of external radiation with the shielding of the detector.

5.1 LUXSim

In order to study background rates during the 85.3 day WIMP search run (run 3) of LUX, that lasted from April 21 to August 8, 2013 [A$^+$13e], simulations of the main radiation sources were made using *LUXSim*, a *Geant4* based simulation package used by the LUX collaboration [A$^+$12e]. *LUXSim* inherits the plasticity and physical accuracy of the *Geant4* simulation software for interaction of radiation with matter, developed by CERN, meaning that it can accurately reconstruct the detector of LUX and test the response of the various components to incoming particles of different kinds. As we are dealing with a low-energy and low-background experiment, the underground deployment of the detector and the shielding provided by the water tank have rendered the external radiation sources secondary when comparing to the dominant inner radioactive sources from detector construction materials. In order to simplify the study these low-energy backgrounds, a new set of classes was developed to allow multiple radioactive sources to be set within any number of components. *LUXSim* also allows various levels of detail in data recording and defining them in specific components, making it easier to study and control. This flexibility in source generation and recording control makes *LUXSim* very useful in background analysis and detector response tests.

The simulation package presents the user with various built-in detector geometries, from simple detectors with basic active volumes and PMT arrays to the most complex and accurate detector description, built from the original blueprints of LUX. The result is a reliable framework that generates simulated events that closely mimic those from the real detector, producing event timelines with simulated PMT response. The *1.0Detector* geometry built within the framework of *LUXSim* has all the detector components thoroughly built, not only the active xenon volume and the PMT arrays but also the grid wires, PMT holders, cryostat stand, reflector sheets/holders, thermal shields and the muon water tank.

Materials used in the construction of LUX detector need to be defined meticulously within *LUXSim* in order to deliver valid information of interactions. Basic proprieties, such as elementary constitution, density, refractive index, radiation absorption length and reflectivity, allow a good computational replication of common interaction processes like ionization, surface reflectivity or Cherenkov radiation.

Possible *LUXSim* radiation sources include single decay generators, single particles and general particle sources inherited from *Geant4* and some specific sources implemented in *LUXSim*, such as entire or partial decay chains, specific particle generators like the WIMP generator, neutron sources like the *AmBe* generator and excited nucleus sources like the *Kr85m* isomer generator for $^{85\mathrm{m}}$Kr decays. Multiple sources can be set in a single volume and different volumes with associated sources can be set simultaneously, allowing versatile and complete distributions of radiation in the detector. Sources are set with independent activities so that coherent event rates can be obtained. These activities can be set per unit mass of the detector component where they are placed, very useful when the mass of the component is not known with precision.

Some of the radiation sources used in *LUXSim* are presented on the following list.

- The particle gun and general particle source (GPS) commands allow simple particles to be set in a certain position in the geometry, with a defined energy and initial direction. The GPS is more powerful than the simple particle gun, allowing surface or volumetric placement of a source and the capability to randomize the kinetic energy, position or direction from a user specified distribution [Asa].

- The single decay command uses the vast *Geant4* libraries to simulate a certain decay of an isotope, with atomic mass specified with *AA* and atomic number specified with *ZZ*.

- Decay chain sources like *U238* or *Th232* are also available and set all chain stages automatically, whether secular equilibrium is considered or the age of the source is given.

- Special sources like *AmBe* or *Kr85m* were designed for *LUXSim* and serve different purposes like calibration, being the former a well characterized neutron source and the latter a usual LUX internal calibration source.

- A WIMP generator is also available, allowing simple studies of the response of *LUXSim* to WIMP-like nuclear recoils generated from WIMPs of different masses following the expected recoil energy spectrum for our dark matter halo [McC10].

LUXSim also inherits the exhaustive physics library of *Geant4* for interaction of radiation with matter. This means that all main interaction processes are well implemented within the simulation, tested thoroughly by the big *Geant4* community. This is the strongest feature of *LUXSim* and *Geant4*: the ability to feature physical processes using stochastic methods that return accurate representations of real physical systems. The physics list of *Geant4* is useful from high-energy to low-energy physics but LUX requires a more complete physics list in the field of noble gases and scintillation processes. The *"Noble Element Simulation Technique"* (NEST) simulation code has been developed at UC Davis and LLNL [SBK$^+$11] to accurately parameterize the response of liquid xenon to radiation interaction and to model electron recoil scintillation and ionization yields and improve the description of nuclear recoils.

The output from *LUXSim* is in a easy to read binary format that allows simple conversion tools to generate data structures ready for analysis. Matlab and ROOT converters are available to process these low-level files and return high-level structures with all the information properly organized. If the simulation includes light propagation to the PMTs, either by following each optical photon or using a parametrization for the light distribution on the PMTs as discussed later on, a specific converter called *LUXSim2evt* generates files[2] with all the complex light pulse shapes, pulse characterization, timing and the corrections required for processing the information of the event with the *Data Processing* analysis chain. Viable *evt* files are only produced if optical photons or thermal electrons are being recorded in the photocathodes of the PMTs in order to produce all the necessary pulse features.

---

[2] These files have the extension *.evt* and are usually cited as *evt* files.

5.1.1 Control variables

LUXSim commands are used to control simulations and ensure proper data collection. For most backgrounds studied, only total energy deposition and interaction position per event is required – this is the case of ^{127}Xe, ^{85}Kr and ^{214}Pb that are uniformly mixed in the liquid xenon and either decay trough β emission or emit γ rays that result in high-energy signatures if they deposit their energy in the xenon volume, not contributing to the low-energy background unless the γ ray exits the active region. For other background sources, a more detailed analysis is required due to the high probability of multiple interactions in the active region – this is the case of γ-rays from sources surrounding the active volume[3]. The level of detail of the recorded data can be controlled using the *recordLevel* variables[4]. Table 5.1 presents the different levels of recording per particle type and their function.

Table 5.1: Summary of the different record levels in *LUXSim*. It should be noted that setting an optical photon or thermal electron record level to an odd number stops the progression of this particle in the specified volume. †energy, position and direction.

Level:	**recordLevel**	**recordLevelOptPhot**	**recordLevelThermElec**
0	Do not record (default)	Do not record (default)	Do not record (default)
1	only total deposited energy	number of optical photons entering the volume and stops these particles	number of thermal electrons entering the volume and stops these particles
2	steps with energy deposition	number of optical photons entering the volume and let them propagate	number of thermal electrons entering the volume and let them propagate
3	all steps, even without energy deposition	all information† about optical photons and stops these particles	all information† about thermal electrons and stops these particles
4	same as level 3	all information† about optical photons and let them propagate	all information† about thermal electrons and let them propagate

Besides record levels, some *LUXSim* control variables can be set to make the simulation faster and lighter, depending on the output information required. Some geometry elements may not be required for a certain run and disabling them makes geometry loading faster. For a simple run with only total energy depositions per event it is unnecessary to load the cryostat stand or grid wires for instance, avoiding a sluggish simulation initialization.

Table 5.2 shows the basic structure of a simulation control file, called a macro file, with the common commands that were used for all simulations.

---

[3] Sources outside the liquid xenon active volume are present in construction materials inside the cryostat of LUX.

[4] There are different record level variables for different particles. The *recordLevel* variable controls the level of detail for all secondary particles except optical photons (scintillation or Cherenkov) and thermal electrons (ionization electrons being drifted and photo-electrons created in the photocathodes), that are controlled by *recordLevelOptPhot* and *recordLevelThermElec* respectively.

Table 5.2: The anatomy of a macro file to define the control variables in *LUXSim*. These values are set in order to extract the required data from a simulation in a optimized way. †The values displayed are the ones used in this analysis, but they were changed after this work.

	variables	
1	/run/initialize	
2	/LUXSim/detector/select	1_0Detector
	/LUXSim/detector/gridWires	on / off
3	/LUXSim/detector/cryoStand	on / off
	/LUXSim/detector/muonVeto	on / off
	/LUXSim/detector/topGridVoltage	-1 kV
	/LUXSim/detector/anodeGridVoltage	3.5 kV
4	/LUXSim/detector/gateGridVoltage	-1.5 kV
	/LUXSim/detector/cathodeGridVoltage	-10.0 kV
	/LUXSim/detector/bottomGridVoltage	-2 kV
5	/LUXSim/detector/update	
6	/LUXSim/physicsList/useOpticalProcesses	0 / 1
7	/LUXSim/physicsList/s1gain	1 / 0.120†
8	/LUXSim/physicsList/s2gain	1 / 0.431†
9	/LUXSim/physicsList/driftElecAttenuation	1 m
10	/LUXSim/detector/recordLevel	[volume] 1 / 2
11	/LUXSim/detector/recordLevelThermElec	PMT_PhotoCathode 0 / 3
12	/LUXSim/detector/recordLevelOptPhot	PMT_PhotoCathode 0 / 3
13	/LUXSim/source/set	[volume] [source] [activity] [units]
14	/LUXSim/beamOn	[number of events]
15	exit	

The first command is always required to initialize the simulation. The second command selects the complete detector and all geometry components. The commands marked with 3 enable/disable the grid wires, cryostat stand and water tank placement, respectively. If grid wires are loaded in the geometry it is possible to set the voltage on each grid with the commands shown in 4. The values presented are taken from the original grid voltages used for the WIMP search run. After all relevant components are selected, command 5 is required to update and build the geometry.

Geant4 (and consequently *LUXSim*) has built-in commands to "turn on or off" some physical processes. If no light propagation is required, like in a study without the need to generate scintillation light, *useOpticalProcesses* can be set to 0 or *false*. Toggling this variable can make the simulation much lighter by not creating photons, or incredibly sluggish because all photons generated are being tracked. For accurate studies of light propagation this variable should be set to 1 or *true* and both *s1gain* and *s2gain* set to 1, at the expense of a lot of simulation time. The thermal electrons simulated from ionization events in the xenon volume are responsible for generating the S2 signal. *LUXSim* uses the values of voltage set to each grid to specify the kinetic energy of the electrons that are then given the adequate direction of motion, opposite to the electric field generated in the respective region. The electroluminescence signal is dependent of the quantity of these thermal electrons extracted to the gas region, that depends of the value of the *s2gain* variable. The variable *driftElecAttenuation* simulates the amount of liquid xenon impurities. The impurity control is important when drifting electrons through the xenon volume is needed, and the last command means that the mean free path set to thermal electrons is 1 m, almost double the active region height, which has 0.54 m. This length value is taken from the measured run 3 mean purity levels [A$^+$13e].

Primary scintillation (S1) and secondary scintillation (S2) gains can toggle a *Fast Simulation* if one or both values are lower than 1. A *Fast Simulation* generates data as if optical photons were being propagated, generating good light distributions as seen by the PMTs (PMT hit maps), but instead of actually propagating scintillation light, *LUXSim* uses lookup tables generated using real data, and which convolutes all the possible bias from real data, that return the expected light yield and PMT hit maps for that kind of event in the active region, resulting in fast and reliable simulations. The alternative values for commands 7 and 8 are the light collection efficiency at the center of the detector (12%) and the extraction probability across the liquid-gas boundary (43.1%), respectively[5].

For total energy deposition studies the *recordLevel* variable can be set to 1 and the remaining record level variables, *recordLevelOptPhot* and *recordLevelThermElec*, can be set to zero, as the respective particles do not need to be followed. However, when a more detailed analysis is required concerning energy deposition, *i.e.* when single or multiple scatters need to be distinguished, following all secondary particles in some volume is achieved by setting the *recordLevel* variable to a higher-than-one value. When scintillation is turned on and the objective is to simulate light propagation and PMT hit maps as they are expected in the real detector, setting the record level for optical photons and thermal electrons in the *PMT_Photocathode* volumes to 3 or 4 is required.

Setting a source in a determined volume requires information on the nature and activity of the source. On some more specific sources like entire decay chains it is also possible to set the age of the source, otherwise secular equilibrium is considered.

The simulation control commands end with the specification of the number of events from the selected source to be simulated. This is done with the *beamOn* command followed by the number of events to produce. Having only one source defined means that all particles will come from that source, but if multiple sources exist in one run the number of particles per source will be weighted using the activities of the sources, returning the number of events defined with *beamOn*.

---

[5] These values were set using a macro file given to me by Kevin O'Sullivan within Slack page *LUXexp:LUXSim*, on March 30th at 7:14 PM. These values were changed after this work, the ones displayed are the ones used in this analysis.

5.2 Analysis of gamma ray sources in *LUXSim*

In the LUX detector, the main background sources are high-energy γ rays from construction materials, from the decay chains of trace amounts of uranium and thorium, as well as trace amounts of naturally-occurring potassium-40 and the cosmogenically activate isotopes cobalt-60 and scandium-46. Most of the mass of the detector, excluding liquid xenon, is in the copper and titanium in structures such as the PMT mounts, radiation shields, field-shaping rings, grid wires and the inner and outer cryostat vessels. These materials have some radioactive content that can produce high-energy radiation capable of interacting with the active xenon.

The following study aims to validate these simulated radiation sources in order to verify the consistency of the γ ray background simulations in *LUXSim*. The sources studied are ^{238}U and progeny, ^{232}Th and progeny, ^{40}K and the activated isotope ^{60}Co. No signs of ^{46}Sc signatures (present in the titanium cryostats) was recorded in LUX, probably due to shielding provided by the internal materials and it was therefore excluded from this analysis.

5.2.1 Potassium-40

^{40}K is a long-living radioactive isotope of potassium with a half-life of 1.2504 ± 0.0030 Gy, present in natural potassium in concentrations of 117 ppm g/g (0.0117%) [ABB$^+$15]. This isotope is one of the rare unstable elements that decays through three different channels [ABB$^+$15]:

1. Decay to calcium-40 via $\beta^- \bar{\nu}$ emission with 1.33 MeV endpoint energy (89.25(17)%)
2. Decay to argon-40 via electron capture (EC) with emission of a 1.460.85 MeV γ-ray and ν (10.55(11)%) or to the ground-state of argon-40 (0.2(1)%)
3. Decay to argon-40 via $\beta^+ \nu$ emission with 482.9 keV endpoint energy ($< 0.001\%$)

The high-energy γ-ray emitted upon electron capture is the main reason why this isotope is an important background, as these γ-rays are energetic enough to reach the inner detector volume and could deposit their energy in the active xenon. The decay scheme of this isotope can be viewed in Appendix A.

^{40}K was detected in the PMTs used in LUX, as described in detail in Section 5.6. To verify that *LUXSim* generates a correct ^{40}K spectrum, a total of 75×10^6 decay events from this source in the PMT window volume were simulated. The γ ray spectrum was obtained using the *LoadAndBuildLUXSim Matlab* tool that reconstructs each event with energy deposition in the liquid xenon volume as the real detector would perceive it (therefore including light propagation). The obtained γ spectrum is represented in Figure 5.1.

All the expected features from a typical ^{40}K spectrum are present in Figure 5.1 with the expected energies.

The obtained branching ratios of the decay of ^{40}K are also consistent with the expected values [ABB$^+$15]:

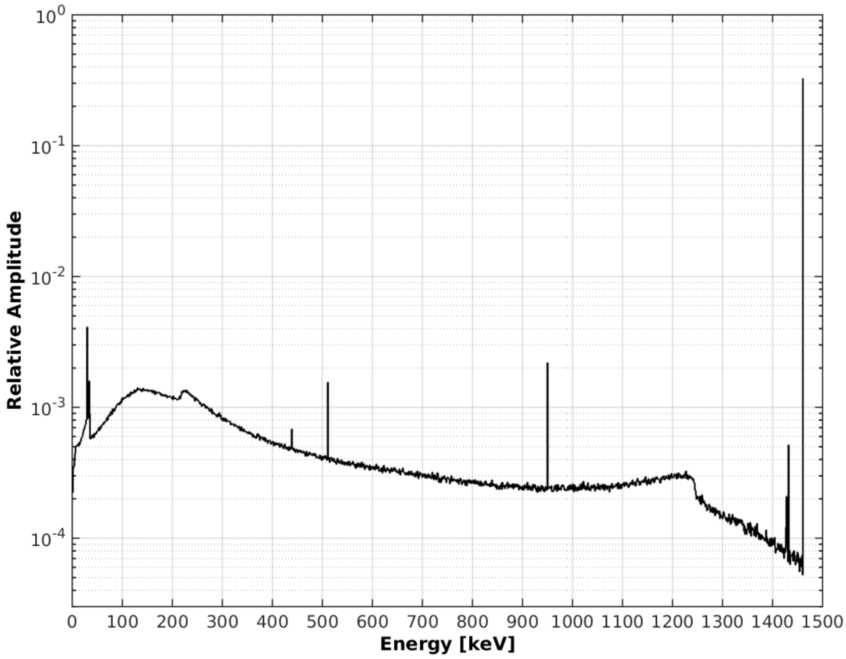

Figure 5.1: Reconstructed γ ray spectrum from ^{40}K decays in the top and bottom PMT windows, obtained using *LUXSim*. All normal γ spectroscopy features are observable, including (in decreasing energy) the photopeak at 1460.85 keV, Compton edge at 1243.35 keV, the first escape peak at 949.85 keV, the annihilation peak from pair-production positrons at 510.95 keV, the backscatter peak between 200 – 250 keV and X-ray features at lower energies, corresponding to absorption of the 29.75 keV $k_{\alpha 1,2}$ line, 33.65 keV $k_{\beta 1}$ line and 34.45 keV $k_{\beta 2}$ line [Rob74]. The peaks near the photopeak, with energies of 1426.45, 1427.15 and 1431.05 keV are from events where the X rays from xenon escaped the volume. The spectrum and the reconstructed energies were obtained using Matlab.

1. Decay to ^{40}Ca via β^- emission - 89.301%
2. Decay to the 1460.83 keV excited state of ^{40}Ar by EC - 10.497%
3. Decay to the ground state of ^{40}Ar by EC - 0.202%

5.2.2 Cobalt-60

^{60}Co is a synthetic isotope produced through neutron activation in construction materials, namely copper. It decays through β^- emission into ^{60}Ni with a half-life of 5.2714 y, releasing two γ-rays with energies of 1.173 MeV and 1.333 MeV through de-excitation of the nickel daughter to the ground state [End93].

Both high-energy γ-rays have a significant mean free path in the dense bulk materials of the detector and can reach the active volume, originating ER background. The decay scheme of this isotope is shown in Appendix A.

The expected activation rate for ^{60}Co in copper components, such as PMT array mounts, γ ray radiation shields, thermal shields and field shaping rings, is taken to be 210 ± 100 kg^{-1} day^{-1} due to the muon-induced neutron flux through the detector internals while these were stored and assembled at the Sanford Surface Laboratory, at an altitude of 1.6 km above sea level [M+14]. The activation is considered negligible underground.

Decay signatures from ^{60}Co were detected in all PMTs (as discussed in detail in Section 5.6). The γ ray spectrum of ^{60}Co was simulated by setting this source in the bottom and top PMT windows. The event reconstructions was obtained using the *LoadAndBuildLUXSim* MAtlab tool, resulting in the γ spectrum represented in Figure 5.2. All the expected features from a typical ^{60}Co spectrum are present and with the expected energies.

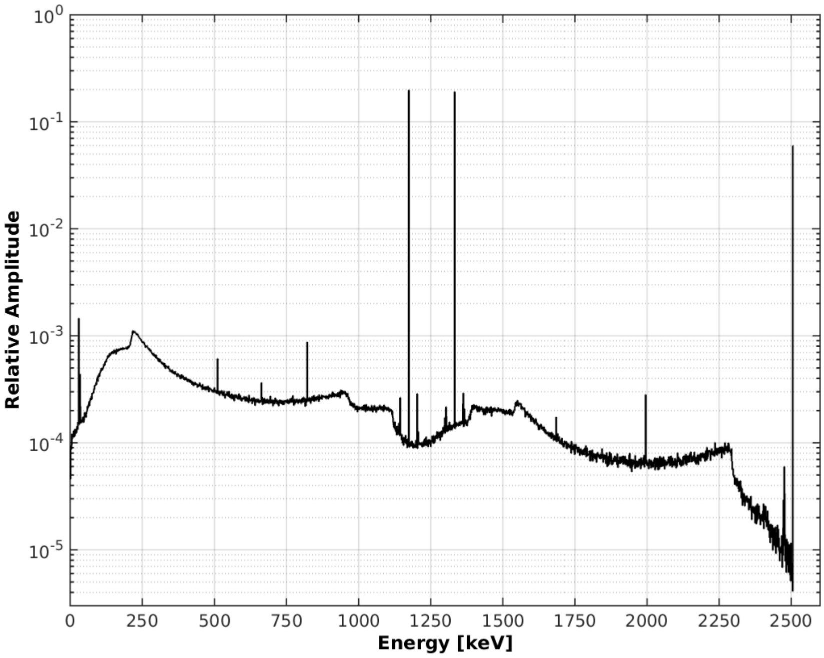

Figure 5.2: Reconstructed γ ray spectrum from ^{60}Co decays in the top and bottom PMT windows, obtained using *LUXSim*. Both ^{60}Ni de-excitation γ rays, with energies 1173.25 keV and 1332.45 keV, are well visible. The peak with energy 2505.75 keV arises from the absorption of both de-excitation γ rays simultaneously. Because we have three distinct photopeaks, three Compton edges arise at energies 963.45 keV for the first photopeak, 1118.15 keV for the second photopeak and 2273.9 keV for the conjoint peak. The escape peaks for the first, second and combined photopeaks have energies of 662.25, 821.45 and 1994.75 keV, respectively. The common features, like the annihilation peak at 510.95 keV, the backscatter peak between $200-250$ keV and the xenon X ray lines are also present. The spectrum also presents some interesting features around the main photopeaks and differing by the energy of the X rays from xenon. These peaks appear when the X rays deposit their energy in coincidence with the γ rays from ^{60}Ni or escape the detector. The spectrum and the reconstructed energies were obtained using Matlab.

5.2.3 Thorium-232

Thorium-232 is a naturally occurring isotope that is responsible for the “Thorium Series” decay chain. The series includes the following elements: actinium, radium, radon, polonium, bismuth, lead and thallium. A thorium-containing sample has all these elements present, at least transiently, and until the stable ^{208}Pb is reached all radionuclides will contribute to the activity of the sample [End00]. Figure A.7 schematically shows the Thorium Series.

LUXSim provides a generator for the Thorium series named *Th232*. This generator simulates the decays of all isotopes present in the chain, calculating the activities of each radioisotope using the given age of this source (otherwise secular equilibrium is considered and all chain steps have the same activity). The generator also accounts for the decay branching of some isotopes, weighing each decay mechanism with the according branching ratio. In the Thorium series this branching occurs in the decay of ^{212}Bi to ^{212}Po (64.06%) and ^{208}Tl (35.94%). A secular equilibrium is considered in this study, and thus the decay of each isotope has the same probability of being simulated using the Thorium series generator in *LUXSim*.

A complete spectrum for this source was obtained (directly from the simulation) by only selecting the energy of γ rays produced by the excited isotopes from decay events, thus excluding other sources of γ radiation such as Bremsstrahlung radiation from high-energy charged particles, Compton scattering or annihilation in the xenon volume of the detector.

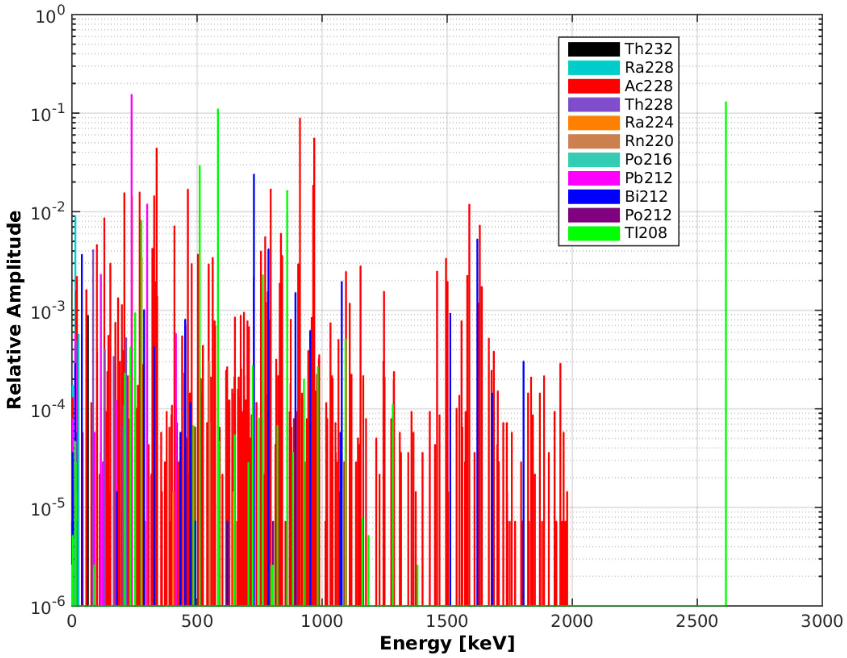

Figure 5.3: Reconstructed γ ray spectrum from ^{232}Th. A simple observation reveals that the isotopes that have a higher contribution to the γ ray spectrum are ^{228}Ac, ^{212}Pb, ^{212}Bi and ^{208}Tl. The residuals between the reconstructed and the total spectrum is 0.1119%. This spectrum and the reconstructed energies were obtained using Matlab.

The total spectrum obtained using the *Th232* generator was then reconstructed using the γ ray contributions from each isotope in the chain, obtained by simulating each isotope individually using *LUXSim* and also excluding secondary γ ray sources. The contribution from each isotope was weighted to account for its activity within the chain. The resulting reconstructed spectrum of ^{232}Th is displayed in Figure 5.3. When comparing the reconstructed spectrum with the one obtained using the generator, a residual of 0.1119% between the total chain activities is obtained, meaning that the synthesization is accurate.

The most worrying γ ray sources along the thorium chain due to their high energy are, as can be seen from Figure 5.3, ^{228}Ac, ^{212}Pb, ^{212}Bi and ^{208}Tl. The relative contribution of these predominant γ emitting isotopes in the Thorium series are summarized in Table 5.3. The decay of ^{228}Ac dominates the spectrum, producing approximately 44.82% of all γ rays in the Thorium series. ^{208}Tl generates a 2614.533 keV γ ray for each decay, very prominent in the spectrum of a thorium containing material. This high-energy γ ray has an average attenuation length in liquid xenon of $\sim$ 10 cm [BHS+98], easily reaching the target xenon volume.

Table 5.3: Contribution of the predominant γ emitting isotopes in the Thorium series. The relative contribution of an isotope is the percentage of γ rays in the reconstructed spectrum that are produced from the decay of that isotope. The most common γ ray energies for each isotope are selected directly from the reconstructed spectrum considering relative amplitudes above 1%.

Isotope	Relative contribution	Main γ energies ($I_r > 1\%$) (keV)
^{228}Ac	44.82%	338.320, 911.204, 968.971
^{212}Pb	17.12%	238.632, 300.087
^{212}Bi	4.65%	727.330
^{208}Tl	30.15%	510.77, 583.191, 860.564, 2614.533

The dominant γ ray energies present in the ^{232}Th spectrum are in agreement with the known radiation energies for all isotopes in the chain [End00, Tul].

5.2.4 Uranium-238

Uranium-238 is another naturally occurring isotope, responsible for the “Uranium Series” decay chain (sometimes called “Radium Series”). The series includes the following elements: protactinium, thorium, radium, radon, astatine, polonium, bismuth, lead, thallium and mercury. A sample containing uranium-238, like the natural and quite common mineral uraninite (UO_2 with $\approx$ 99.284% ^{238}U), has all these elements present, at least transiently. The final isotope to be formed in this series is the stable ^{206}Pb [End00]. Figure A.6 schematically shows the Uranium Series.

LUXSim has a Uranium Series generator named *U238*. Like the *Th232* generator, the activities of each radioisotope present in the decay chain are automatically calculated when providing the age of the uranium source, otherwise secular equilibrium is considered. Secular equilibrium is considered for this source as in the previous case (^{232}Th), and no decay branching is considered for this study because the branching ratios of ^{218}Po, ^{214}Bi, ^{210}Pb and ^{210}Bi (the only isotopes with more than one decay channel in this chain) are lower than 0.021% and therefore negligible [End00].

The method for obtaining the complete spectrum for the Uranium series is the same used in the

Thorium series study. The total spectrum was reconstructed using the γ ray contributions from each isotope in the chain, selecting only γ rays from the decay processes, simulated independently using *LUXSim*, and all contributions were weighed to account for their activity within the chain. The reconstructed spectrum of ^{238}U is displayed in Figure 5.4. In order to correctly reproduce the chain spectrum obtained from the generator, a correction factor of 2 was set to the ^{234}Th, ^{214}Pb, ^{214}Bi when simulated individually. These isotopes contributed to the ^{238}U spectrum with twice the expected amount of γ emissions. Other users within the collaboration have detected that the ^{234}Th and ^{234}Pa decays being counted simultaneously in one single event, while the ^{234}Pa decays were also being computed independently, resulting in a double counting of this isotope [Sha15]. The obtained synthesization is good, with a residual of 3.9847%, possibly due to no decay branching being considered and because of the correction factor used in the activity of some isotopes.

The most concerning γ ray sources along the uranium chain, visible in Figure 5.4, are ^{234}Th, ^{234}Pa, ^{214}Pb and ^{214}Bi. The relative contribution of the predominant γ emitting isotopes in the Uranium series are summarized in Table 5.4. The greatest contributor for this spectrum is ^{234}Pa with approximately 45.79% of the γ rays being produced by the decay of this isotope alone. The decays of the isotope ^{214}Bi, that result in approximately 30.02% of the γ ray content of the uranium spectrum, produce highly energetic radiation, with energies up to 3142.6 keV [End00]. However, γ rays in this energy range (above 2500 keV) are somewhat rare.

The dominant γ ray energies present in the ^{238}U spectrum are in agreement with the known radiation energies for all isotopes in the chain [End00, Tul].

Table 5.4: Contribution of the predominant γ emitting isotopes in the Uranium series. The relative contribution of an isotope is the percentage of γ rays in the reconstructed spectrum that are produced from the decay of that isotope. The most common γ ray energies for each isotope are selected directly from the reconstructed spectrum considering relative amplitudes above 1%.

Isotope	Relative contribution	Main γ ray energies ($I_r > 1\%$) (keV)
^{234}Th	45.79%	63.29, 92.38
^{234}Pa	3.65%	131.30, 152.720, 569.5, 733.39, 880.5, 925.0, 946.00, 980.3
^{214}Pb	15.51%	241.997, 295.224, 351.932
^{214}Bi	30.02%	609.312, 768.356, 1120.287, 1238.110, 1764.494, 2204.21

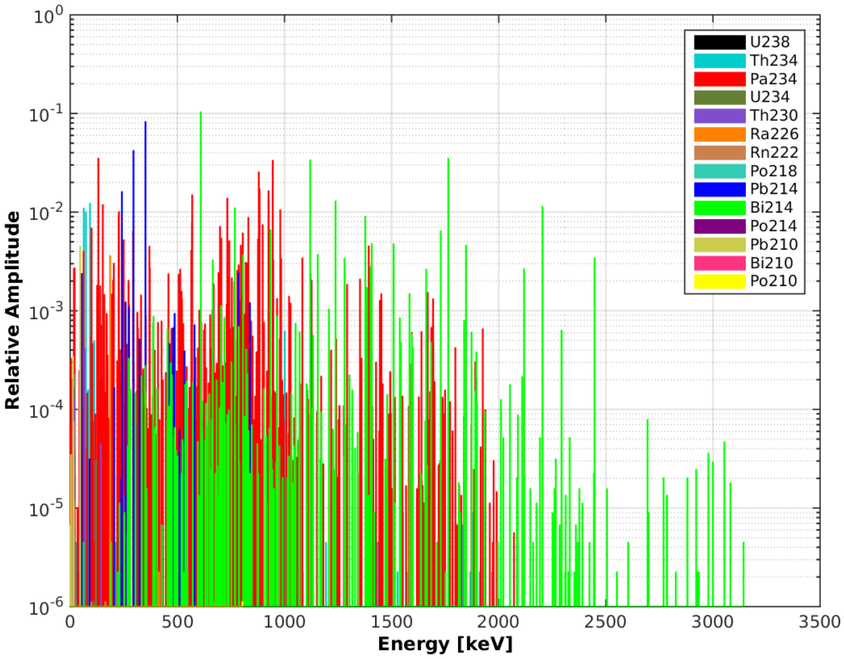

Figure 5.4: Reconstructed γ ray spectrum from the ^{238}U decay chain. The main contributions for this spectrum are from the isotopes ^{234}Th, ^{234}Pa, ^{214}Pb and ^{214}Bi. The residual between the reconstructed and the spectrum obtained using the generator is 3.9847%. A correction factor was used to scale the activities of ^{234}Th, ^{214}Pb, ^{214}Bi when simulated individually to match the activities observed using the generator. This correction factor of 2 presents a problem in the *U238* generator that may be overproducing these isotopes. The spectrum and the reconstructed energies were obtained using Matlab.

5.3 Krypton-85

The isotope ^{85}Kr decays into rubidium-85, ^{85}Rb, with a half-life of 10.756 years mainly by β emission with average energy of $E_\beta = 251$ keV and energy endpoint of $Q = 687$ keV (99.57%), or alternatively by β emission with 173 keV endpoint followed by a 514 keV γ-ray emission (0.43%) [Sie91]. This isotope is produced naturally through interaction of cosmic rays with ^{84}Kr present in the atmosphere of the Earth, generating around 55 Tbq y^{-1}, but the chopping and dissolution of spent fuel rods in nuclear reprocessing facilities of nuclear power plants is the largest source of ^{85}Kr production, releasing around 450 Pbq y^{-1} between 1995 and 2009, meaning that the anthropogenic contribution is four orders of magnitude higher than the natural [A$^+$13d].

Natural krypton, containing the unstable isotope ^{85}Kr, is present in commercial xenon with estimated concentrations of 130 ppb (g/g) upon purchase. The LUX getter only removes electronegative impurities so krypton is not removed with this method. Instead, an independent chromatographic removal system was built using an activated charcoal tower to separate krypton from xenon, with the goal of reducing ^{85}Kr background levels to < 0.2 mDRU$_{ee}$, corresponding to concentrations of $^{\mathrm{nat}}$Kr in xenon < 5 ppt [BBS$^+$07]. Average levels of krypton in the xenon volume during the WIMP search run [M$^+$14] were measured to be:

$$R_{Xe}^{^{nat}Kr} = 3.5 \pm 1.0 \text{ ppt} \tag{5.1}$$

The volumetric activity of ^{85}Kr in natural krypton is taken to be 700 − 800 Bq L$^{-1}_{Kr}$ [K$^+$92]. With a specific activity of $S_{^{85}Kr} = 14.526$ TBq g$^{-1}_{^{85}Kr}$ [Wol] and considering a krypton density of 3.514341 g L^{-1} [LMF11], this corresponds to a fraction of ^{85}Kr present in $^{\mathrm{nat}}$Kr of:

$$R_{^{nat}Kr}^{^{85}Kr} = 1.371 - 1.567 \times 10^{-11}$$

The value presented in [M$^+$14] for this ratio is 20 ppt (g/g) with the uncertainty taken to be a factor ×2. This factor comes from the uncertainty in the volumetric activity of ^{85}Kr in natural krypton obtained in [K$^+$92]. As this value means more krypton activity and corresponds to the worst-case scenario, for this work the ratio used was:

$$R_{^{nat}Kr}^{^{85}Kr} = (2 \pm 1) \times 10^{-11} \tag{5.2}$$

With such a long half-life, ^{85}Kr remains present as a main low-energy background during the entire run 3 length. Considering that all $^{\mathrm{nat}}$Kr remains in the liquid xenon volume because it is not removed any more and ^{85}Kr concentration only decreases due to the decay processes, the variation in concentration during the run 3 length of 109 days is $\sim$ 2%, meaning that a constant activity can be considered for the entire run.

Table 5.5 represents the relative abundance of krypton isotopes in natural krypton, showing the 6 natural stable isotopes (^{78}Kr, ^{80}Kr, ^{82}Kr, ^{83}Kr, ^{84}Kr and ^{86}Kr) and the two natural long-lived unstable ones (^{81}Kr and ^{85}Kr) [Soc01].

Table 5.5: Relative abundance of krypton isotopes in natural krypton and general radioactive proprieties: Half-life (T_{hl}), Specific activity (S) and decay mode. The unstable isotope ^{81}Kr has a longer half-life than ^{85}Kr but a lower specific activity and so it is not considered in LUX background models. All other unstable Kr isotopes have very short half-lives and are not considered.

Isotope	Abundance	T_{hl} (year)	S (TBq g^{-1})	decay mode
^{78}Kr	0.355%	stable	-	-
^{80}Kr	2.286%	stable	-	-
^{82}Kr	11.593%	stable	-	-
^{83}Kr	11.500%	stable	-	-
^{84}Kr	56.987%	stable	-	-
^{86}Kr	17.279%	stable	-	-
^{81}Kr	trace	210×10^3	7.77×10^{-4}	electron capture
^{85}Kr	trace	10.756	14.526	β emission

5.3.1 Krypton Activity in the WIMP search run

As discussed before, the half-life of this isotope is long enough that one can consider a constant concentration in liquid xenon, and so the average activity throughout the WIMP search run is obtained simply by the product of the specific activity $S_{^{85}Kr} = 14.526 \times 10^{12}$ Bq g^{-1} with the concentration fractions 5.1 and 5.2, as shown in Eq. 5.3.

$$\begin{aligned} A_{^{85}Kr} &= S_{^{85}Kr} \;\; R^{^{85}Kr}_{^{nat}Kr} \;\; R^{^{nat}Kr}_{Xe} \\ &= 1.01682 \pm 0.59 \;\; \mu\text{Bq kg}^{-1} \end{aligned} \tag{5.3}$$

This is the ^{85}Kr activity per kilogram of xenon.

Number of events expected

The number of events that are expected for this source in 109 days, in the $m_{Xe} = 224466$ g active volume[6] and considering a constant activity throughout the run, is given by:

$$\begin{aligned} \Delta N &= A_{^{85}Kr} \;\; m_{Xe} \;\; \Delta T = 2149.4873 \\ &\approx 2150 \pm 1238_{sys} \;\; events \end{aligned} \tag{5.4}$$

with $\Delta T = 109$ days the WIMP search run length. The large uncertainty of this value is due to the uncertainty in the fiducial volume mass and mostly from the uncertainty in the activity of krypton.

So, the expected number of decays during the run 3, in the above conditions, is 2150 events.

---

[6] This mass value was taken from the simulation directly, using the known xenon density of $\rho_{lXe} = 2.888$ g cm^{-3} [LMF11] and the geometric volume of the detector calculated using Monte Carlo rejection sampling.

But the WIMP search run was not continuous. The actual live time was in fact 85.3 days. As an approximation, the number of events can be averaged using the ratio of both time lengths. The resulting number of expected ^{85}Kr events is then obtained in 5.5.

$$\langle N \rangle = \frac{\Delta t}{\Delta T} \Delta N \approx 1682 \pm 969_{sys} \;\; events \tag{5.5}$$

This means that, in reality, the expected number of ^{85}Kr decays, averaged over the WIMP search run lasting 85.3 continuous days is 1682 events.

Therefore, the simulated statistics (10^7) is equivalent to ≈ 5945 WIMP search runs of 85.3 days.

5.3.2 Krypton-85 Background Rate

Figure 5.5 exhibits the ^{85}Kr β spectrum obtained with *LUXSim*. This spectrum shows that low-energy events are generated more frequently than higher energy β, resulting in a considerable number of these falling in the WIMP energy window of $0.9 - 5.3$ keV$_{ee}$.

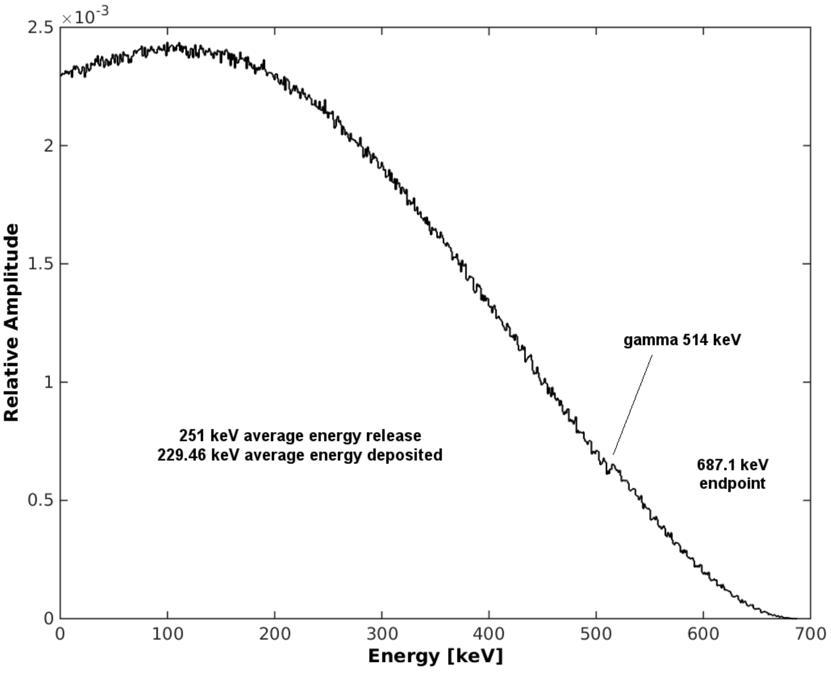

Figure 5.5: Total deposited energy spectrum for ^{85}Kr, with the position of the 514 keV γ ray indicated. Low-energy electrons are more frequent, as expected from a β spectrum, resulting in a significant fraction of the spectrum falling in the WIMP search energy window. The endpoint energy for these β is 687.1 keV and the average β energy release is 251 keV. However, the calculated average energy deposition for this source is 229.46 keV. Decay events with emission of a 514 γ ray ($I_\gamma = 0.43\%$) could contribute further to the low-energy β background if the γ escapes the detector, leaving the associated β to deposit its energy ($Q = 173$ keV) in the active volume.

Figure 5.6 shows the total event density in the liquid xenon volume for 10^7 events. The ^{85}Kr is uniformly mixed in the xenon volume of LUX, meaning that the spacial distribution of Kr events recorded maps the xenon volume defined in geometry. The main xenon volume is easily visible as the region with greater number of events, between $0-54$ cm height and $0-576$ cm^2 squared radius. The xenon between the lower PMT array, directly underneath the active region, presents an interesting pattern, the result of the hexagonal placement of the PMTs (close to an axial symmetry in z with concentric rings of PMTs). A region with a great number of events can be found at $[z \approx -2\text{cm}; r^2 \approx 775\text{cm}^2]$, which should correspond to a gap in the bottom PMT holder in the outer most part of the inner cryostat, filled with liquid xenon [A+12b].

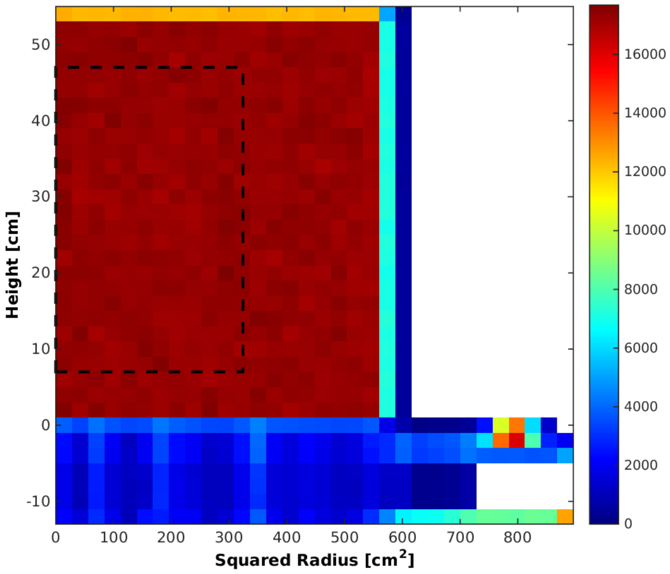

Figure 5.6: Event density of ^{85}Kr decays uniformly distributed in the entire liquid xenon volume, for a 10^7 events simulation. The 118 kg fiducial volume is marked by the dashed rectangle. With this spacial distribution of events it is possible to visualize some geometrical proprieties of the inner cryostat structures like the bottom PMT holder and bottom PMT array, submerged in liquid xenon.

For this intrinsic source, using the data from the spectral and spacial distributions of events, a background rate for the WIMP search energy window of $0.1519 \pm 0.0877_{sys}$ mDRU$_{ee}$ is obtained.

It is possible to tell that the rate for this background in the fiducial volume and in the WIMP search energy window of $0.9-5.3$ keV$_{ee}$ is isotropic and uniform, as expected. The percentage of events that fall into the WIMP search window and in the fiducial volume for this source is $\sim 0.4\%$ of the total number of ^{85}Kr events.

The calculations and methods used to obtain the differential background rate are presented in Eqs. 5.6 and beyond.

$$dR = \frac{N^*}{\Delta t \quad m_{FV} \quad \Delta E} \frac{\langle N \rangle}{N} \text{ DRU} \tag{5.6}$$

where $N^* = 39994$ is the number of simulated events that fall in the WIMP search energy window and fiducial volume, $\Delta t = 85.3$ d is the WIMP search run duration, $m_{FV} = 118.3 \pm 6.5$ kg is the xenon mass in the fiducial volume, $\Delta E = 4.4$ keV is the WIMP energy window size, $\langle N \rangle = 1682$ is the expected number of events of ^{85}Kr for the WIMP search run and $N = 10^7$ is the number of events simulated.

As the ratio of N^* and N represents the fraction of events that fall into the WIMP search window and in the fiducial volume, this new value will now be called P^{Kr85}_{FVWW}. The ratio of $\langle N \rangle$ and Δt represents the average ^{85}Kr activity throughout the run, and so this new variable is denoted by A_{Kr85}. Equation 5.6 can then be rewritten as Eq. 5.7.

$$\begin{aligned} dR_{Kr85} &= \frac{A_{Kr85} \quad P^{Kr85}_{FVWW}}{m_{FV} \quad \Delta E_{WW}} \\ &\approx 0.1519 \pm 0.0877_{sys} \text{ mDRU}_{ee} \end{aligned} \tag{5.7}$$

This result is consistent with the estimated background rate of $0.17 \pm 0.10 \;\; mDRU_{ee}$ obtained in [M$^+$14] for ^{85}Kr during the WIMP search run, based on *LUXSim* data analysis of the source β spectrum.

The associated systematic uncertainty to the rate obtained in this work is mostly due to the big uncertainties in the concentration of krypton in xenon and especially of krypton-85 in natural krypton, taken to be at least 50%, as in [M$^+$14].

5.4 Xenon-127

The isotope ^{127}Xe is present in the LUX xenon via cosmogenic activation of ^{126}Xe that comprises 0.09(1)% of natural xenon [BKPS15]. It decays into ^{127}I by electron capture (EC) with a half-life of 36.358 ± 0.031 days [ABB$^+$15]. The captured electron comes from the K shell with $\sim 85\%$ probability, from the L shell[7] with $\sim 12\%$ probability and the remaining $\sim 3\%$ from higher shells[8], resulting in X-rays or Auger electron cascades with total energies of 33 keV, 5.2 keV and less than 1.2 keV, respectively [KO96, M$^+$14].

The daughter isotope, ^{127}I, is left in the 375 or 203 keV nuclear excited states, with $\sim 47\%$ and $\sim 53\%$ probabilities, respectively. The 375 keV state can decay to ground state via γ emission with a 17% probability, and this γ ray, with a mean free path of 2.6 cm in liquid xenon, can potentially leave the active region without interacting, resulting in a low energy EM signature because of the low energy X-ray deposition from ^{127}Xe decay. The same effect takes place with the escape of the 203 keV γ ray [M$^+$14].

Therefore, the ^{127}Xe background rate depends on the escape probability of these γ rays, and despite the concentration of this radioisotope being (by definition) uniform in the active region, the background varies exponentially with the distance from the edges of the active region. Based on the detector resolution at these energies, it was estimated that around 50% of these low energy EM events originated from the ^{127}Xe L shell cascade (with total energy of 5.2 keV) fall into the WIMP search energy window, as well as 100% of the low energy events from higher shells [M$^+$14].

5.4.1 Xenon Activity in the WIMP search run

The ^{127}Xe short half-life means that the concentration of this isotope in the liquid xenon volume decreases rapidly. So, in order to accurately study the radiogenic background for this source, via *LUXSim* simulation and data processing, the activity at the beginning of run 3 needs to be calculated.

Despite setting the activity in the simulation, *LUXSim* does not calculate the evolution of the activity through time, for any run. Activities only play an active role when multiple sources are set in the same volume, serving as a probability weight for the simulation to randomly sort the events correctly and to guarantee that sources with greater activity have more frequent events. This means that the the time intervals between events have no physical value, as they are calculated based on a unchanging activity. This means that, for single source studies, the activity does not play an active roll.

To obtain the initial activity of ^{127}Xe at the start of the WIMP search run and the expected number of events, the following information was considered:

According to pre-WIMP run measurements, done 13 days after the detector was moved under-

---

[7] Three separate energies should arise, from L_α, L_β and L_γ.

[8] From M, N and so on.

ground and 70 days before the beginning of the run, the ^{127}Xe activity was 2.7 ± 0.5 mBq kg^{-1} of xenon, best fitted using the 375 keV$_{ee}$ peak measured in the LUX data [M$^+$14]. Considering an exponential law for the time varying activity of a radioactive nuclide, and knowing the activity value for $t = 0$, denoted A_0, the activity at any given time can be obtained using Eq. 5.8.

$$A_0 = A_{(t=-70)} e^{-t\lambda} \tag{5.8}$$

where $\lambda = ln(2) T_{hl}^{-1} = (19.0645 \pm 0.0163) \times 10^{-3}$ day^{-1} is the decay constant calculated directly from the half life.

Considering that the xenon activation ceased when the detector was moved underground, and that the initial ^{127}Xe activity 70 days before the run started was $A_{(t=-70)} = 2.7 \pm 0.5$ mBq kg^{-1} [M$^+$14], the value for the activity *per* kilogram of xenon at the beginning of the run of $A_0 = 710.87 \pm 131.82$ μBq kg^{-1} is obtained.

Number of events expected

Because a *single_decay* source is being used, which only sets the time between events based on the given activity and does not re-calculate it, the times are as if the activity and concentration of the isotope were constant. So, in order to analyse the ^{127}Xe background rate, the expected number of events for this source during the WIMP search run needs to be calculated, that lasted 109 calendar days. These calculation are presented next

The number of events that are expected for this source in 109 days, in the xenon volume, is given by Eq. 5.9.

$$\begin{aligned} \Delta N =& N_0 - N = \left(\frac{A_0}{S} m_{Xe} \frac{N_A}{M_{Xe127}} \right) \left(1 - e^{-\Delta T \lambda} \right) \\ \Delta N &= 830787.943 \approx 830788 \pm 154061_{sys} \end{aligned} \tag{5.9}$$

where A_0 is the initial activity calculated using Eq. 5.8, $S = 1.0434 \times 10^{18}$ Bq kg$^{-1}_{^{127}Xe}$ is the specific activity of ^{127}Xe, $m_{Xe} = 293.744$ kg is the entire liquid xenon mass calculated using *LUXSim*, $N_A = 6.022 \times 10^{23}$ mol^{-1} is the Avogadro constant, $M_{Xe127} = 126.905184(4)$ g mol^{-1} is the molar mass of ^{127}Xe and $\Delta T = 109$ days is the WIMP search run length.

So the expected number of decays during the run 3, in the above conditions, is 830482 events. But the WIMP search run was not continuous. The total live-time is in fact $\Delta t = 85.3$ days. So, as an approximation, the number of events can be averaged using the ratio of these two time intervals, as shown in Eq. 5.10.

$$\langle N \rangle = \frac{\Delta t}{\Delta T} \Delta N \approx 650149 \pm 120563_{sys} \text{ events} \tag{5.10}$$

This means that the expected number of ^{127}Xe decays, averaged over the WIMP search run of 85.3 live days is 650149 events. The number of runs equivalent to the number of simulation generated events (3×10^8) is therefore ≈ 461.

5.4.2 Xenon-127 Background Rate

The total energy spectrum for this source is in Figure 5.7. A zoom in to the lower energy region is shown in the inset where the energy lines from the three decay EM cascades can be seen clearly. The WIMP search energy window of $0.9 - 5.3$ keV$_{ee}$ is represented by the red dashed rectangle.

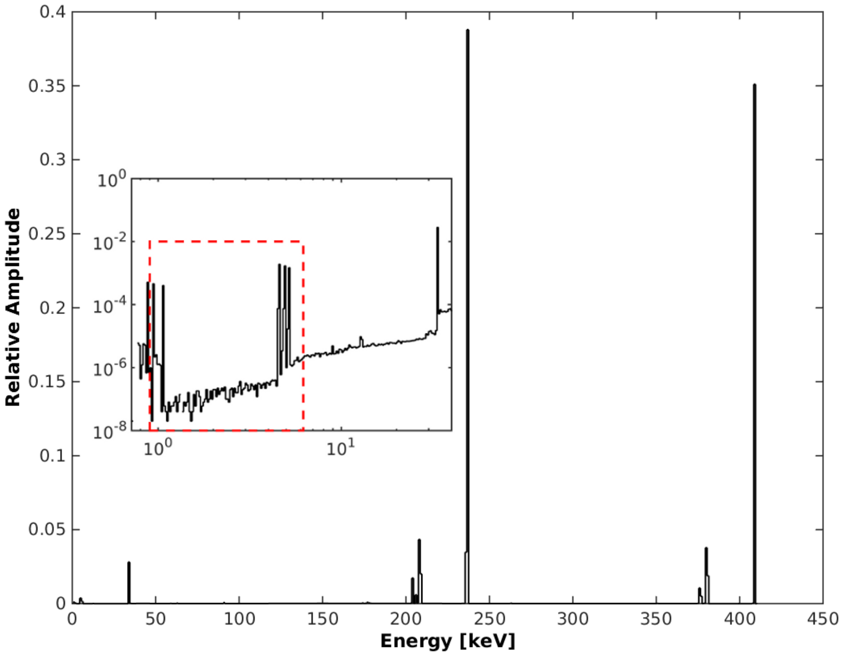

Figure 5.7: Total energy spectrum for ^{127}Xe decay in the entire liquid xenon region, obtained using *LUXSim*, showing the two main peaks with 236.1 and 408.2 keV. The former arises from the absorption in coincidence of the 203 keV γ ray from ^{127}I and the 33 keV K shell energy X-ray from ^{127}Xe decay. The latter arises from the absorption in coincidence of the 375 keV γ ray from ^{127}I and the same 33 keV X-ray from ^{127}Xe decay. Smaller peaks near these can be seen and come from all other combinations between the two ^{127}I excited states and the three EM cascade energies from ^{127}Xe decay. At lower energies, up until 33.15 keV, some peaks are visible, representing the deposition of ^{127}Xe X-rays only, due to the escape of the higher energy γ rays. These cases are the ones which fall in the WIMP energy window. The inset shows the three decay cascade energies. From the K shell electron capture emerges the 33.15 keV peak, from the L shells electron capture the 5.2 keV peak and for higher shells the peaks with energies lower than 1.2 keV. The decay probabilities are 85%, 12% and 3% respectively. These peaks represent the deposition of ^{127}Xe X-rays only.

Conservatively, it is expected that all event from higher shells fall within the energy search window. Half of the L shell X-rays also fall into the energy window of $0.9 - 5.3$ keV$_{ee}$ [M^{+}14] and need to be carefully studied. As this low-energy background is only relevant when the high-energy γ rays leave the volume without interacting, and the probability of this decreases exponentially with the distance from the edges of the active region, the background rate will also behave in the same manner, resulting in less low-energy events at the core of the active region. This gradient effect can be observed in Figure 5.8, representing the event rate for this source in the active region and in the $0.9 - 5.3$ keV$_{ee}$ energy range.

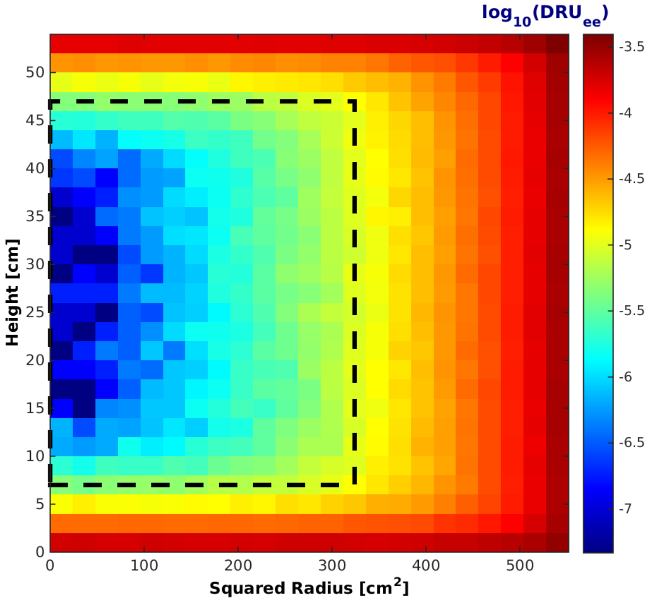

Figure 5.8: Simulated ^{127}Xe ER background density in the range $0.9 - 5.3$ keV$_{ee}$ as a function of position, taken from the decay event density. Rates are in units of log_{10}(DRU$_{ee}$). The 118 kg fiducial volume used in the 85.3 day WIMP search run is overlaid as the black dashed contour.

The center of the volume has a very low background rate (it is quiet) because the γ rays emitted upon the decay of this source are less likely to escape the xenon target, vetoing the low-energy signatures of the X-rays. The low-energy depositions decrease with the distance from the detector edges. The fiducial volume (dashed) is set to a radius of 180 mm and height of 400 mm (from 70 mm to 470 mm above the cathode grid) and contains around 118.3 ± 6.5 kg of liquid xenon [Sil15].

To obtain enough statistics in the central region, the number of decay events simulated was 3×10^{8}, in 1×10^{6} event runs. The percentage of events that fall into the WIMP search region and within the 118 kg fiducial volume in this study was calculated to be 0.003%. Only half the L shell and higher shell decay events in coincidence with the escape of the γ rays from ^{127*}I fall into the energy region of interest, but these events are somewhat rare, when compared to the total number of decays. In order to sort a reasonable amount of the events of interest, many decay events need to be processed.

The calculation method used to obtain the differential BG rate is presented in Eq. 5.11.

$$dR = \frac{N^*}{\Delta t \quad m_{FV} \quad \Delta E} \frac{\langle N \rangle}{N} \tag{5.11}$$
$$(\text{events kg}^{-1} \text{ keV}^{-1} \text{ d}^{-1})$$

where $N^* = 9000$ is the number of events that fall in the WIMP search window, $\Delta t = 85.3$ d is the WIMP search run duration, $m_{FV} = 118.3 \pm 6.5$ kg is the xenon mass in the fiducial volume, $\Delta E = 4.4$ keV is the WIMP energy window size, $\langle N \rangle = 650149$ is the expected number of events of ^{127}Xe decays for the WIMP search run and $N = 3 \times 10^8$ is the number of events simulated.

As mentioned in Section 5.3.2, the ratio of N^* and N can be translated as the percentage of events that fall into the WIMP search window and in the fiducial volume, P^{Xe127}_{FVWW}, and the ratio of $\langle N \rangle$ and Δt as the average ^{127}Xe activity throughout the run, $\bar{A}_{Xe127}$. Equation 5.11 can then be rewritten as Eq. 5.12.

$$\begin{aligned} dR_{Xe127} &= \frac{\bar{A}_{Xe127} \quad P^{Xe127}_{FVWW}}{m_{FV} \quad \Delta E_{WW}} \\ &\approx 0.440 \pm 0.085_{sys} \text{ mDRU}_{ee} \end{aligned} \tag{5.12}$$

This value is consistent with the estimated $0.5 \pm 0.02_{stat} \pm 0.1_{sys}$ mDRU$_{ee}$ obtained in [M$^+$14] for ^{127}Xe, based on data analysis from *LUXSim*, for the WIMP search run, falling between the uncertainty limits. The associated uncertainty to the rate obtained in this work is mostly due to the big uncertainty in the number of ^{127}Xe events expected for run 3, which in turn is due to the relatively large uncertainty in the measured ^{127}Xe initial activity given in [M$^+$14]. The small value of P^{Xe127}_{FVWW} requires that a very large amount of data is simulated in order to obtain a suitable sample of events that fall in the WIMP search window.

5.5 Lead-214

Several radon daughters were identified in LUX data through their α decay signatures - α particles have typical energies of order $5 - 6$ MeV, but reaching higher energies like the α particle from the ^{212}Po decay with energy 8.8 MeV, and these high energy depositions result in large S1 signal, from 4×10^4 to 9×10^4 photoelectrons (phe), when compared to γ ray events which read up to 1.5×10^4 phe [Bra14]. The decay chains of the ^{222}Rn and ^{220}Rn isotopes are considered to be the only sources of α decays in LUX, and amongst the daughter stages are ^{214}Pb and ^{214}Bi for the first and ^{212}Pb and ^{212}Bi for the second. These isotopes can undergo *naked* or *semi-naked* β decay that can produce a low-energy background in the LUX data [M$^+$14].

A *naked* β decay is characterized by the emission of a β particle without any accompanied γ ray emission. One the other hand, a *semi-naked* β decay is characterized by the emission of a β particle accompanied by the emission of a high-energy γ ray. If this high-energy γ leaves the detector without interacting, due to the typically large mean free path of this type of radiation [BHS$^+$98], the observed energy will be only from the interaction of the β particle and the event is perceived as a *naked* β event. A low-energy ER background arises from these *naked* events because there is no high-energy γ ray energy deposition that could veto the event.

Figures A.6 and A.7 represent the decay chains that contain ^{219}Rn, ^{220}Rn and ^{222}Rn. The isotope ^{219}Rn is not considered in these background studies due to its short half-life (4 seconds) existing only in trace amounts on atmospheric radon.

Isotopes that undergo α decay can be easily ruled out of LUX data, as mentioned above, and so only a few radon daughters can generate low-energy ER background capable of falling into the WIMP search window. Furthermore, if a daughter isotope with a very short half-life emits an α particle immediately after the decay of the parent isotope it can "shadow" the signal of the parent, if the time interval between the two events is smaller than the time resolution of the detector[9]. So not only all α decaying isotopes are easily excluded in LUX signal processing but also a large fraction of decays from isotopes with very short-lived, α emitting daughters result in the exclusion of the events from the decaying parents.

These restrictions to which isotopes can contribute to the low-energy background result in just a few candidates left from the decay chains containing radon, which will be discussed below in more detail.

Radon-222

The longest-living isotope, ^{222}Rn, is considered to be the biggest contributor to the radon activity in LUX [M$^+$14]. In its decay chain the only isotopes that do not decay through α emission as the main decay branch[10] are ^{214}Pb and ^{214}Bi.

---

[9] Reconstruction efficiency for short-lived isotopes is limited due to the overlap with the parent event in the LUX 1 ms event window.

[10] Some isotopes by multiple channels, such as ^{218}Po or ^{214}Bi that decay by α or β emission. However, in all the decay chains considered, the branching ratios for any multi-channel decays are disparate, so only the main

The isotope ^{214}Pb decays with a half-life of 26.8 ± 0.9 minutes into ^{214}Bi via β emission with a maximum energy release of 1024 ± 11 keV. The main β energy end-points and associated γ ray energies are shown in Table 5.6. The total energy spectrum for this source, obtained directly from *LUXSim*, is represented in Figure 5.9. As the daughter of this isotope has a half-life of 19.9 minutes the reconstruction efficiency of these decays is $\sim$ 100%. As the decays of this source can generate *naked* and *semi-naked* events, this source will contribute to the low-energy background in LUX.

Table 5.6: Main endpoint energies for ^{214}Pb β emission and associated γ ray energies, for semi-naked decays. The relative probability of each particle emission is also given. Some of these γ rays are very energetic and their escape from the active volume could result in the deposition of the lower energy of the β ray. The *naked* decays corresponding to β emissions with endpoint energy equal to the total energy release (6.3%) do not have any associated γ ray emission that could veto these events as background.

$\mathbf{E}_\beta$ (keV)	P_β (%)	$\mathbf{E}_\gamma$ (keV)	P_γ (%)
136	0.034	-	-
185	2.77	839.04	0.587
226.76	0.021	-	-
490.33	1.18	533.66	0.186
672.07	48.9	351.932	37.6
728.78	42.2	295.224	19.3
1024	6.3	*naked*	-

^{214}Bi decays into ^{214}Po via β emission with a half-life of 19.9 ± 0.4 minutes and a branching ratio of 99.979%, releasing 3272 keV. For the main decay channel, the daughter isotope, ^{214}Po, has a half-life of 164.3 μs before decaying into ^{210}Pb via α decay, making the reconstruction efficiency for these events very limited – with a 90% overlap probability within the LUX 1 ms event window. In order to account for this background, it is considered that 10% of these decay events are detected [M$^+$14].

Radon-220

^{220}Rn was present in LUX during the WIMP search run along with ^{222}Rn. In the respective decay chain, the only isotopes that do not decay through α emission are ^{212}Pb and ^{212}Bi, much similar to the previous chain [Mal13].

^{212}Pb decays via β emission into ^{212}Bi with a half-life of 10.64 ± 0.01 hours and a maximum energy release of 573.8 ± 2.0 keV. The β ray energy end-points and associated γ rays are presented in Table 5.7. The latter β emission does not have any associated γ ray emission and is therefore a *naked* decay, contributing to the low-energy ER background. The total energy spectrum for this source, obtained directly from *LUXSim*, is represented in Figure 5.10. As the daughter of this isotope has a half-life of 60.55 minutes the reconstruction efficiency of these decays is practically total.

---

channel is considered.

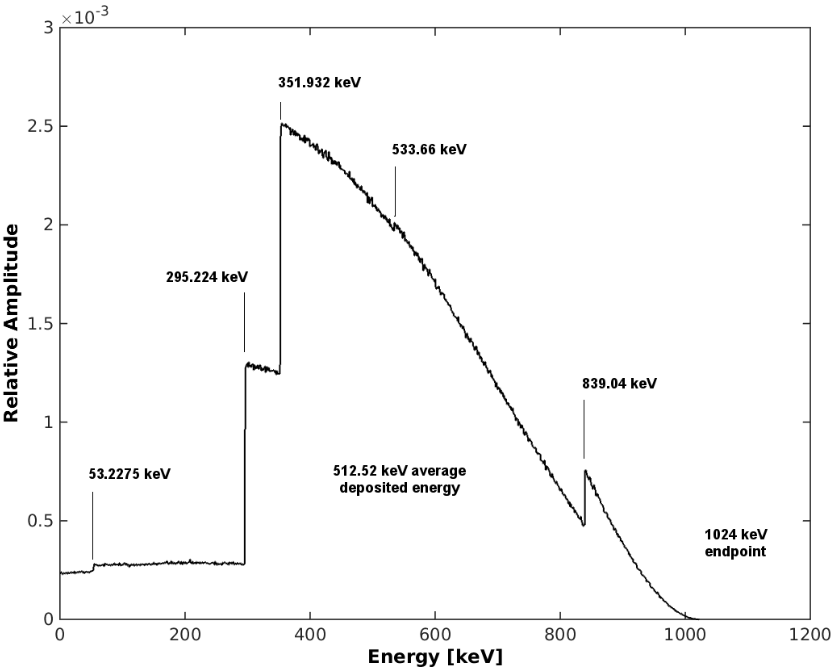

Figure 5.9: Full spectrum for ^{214}Pb beta decay in 1 keV bins (2×10^7 events uniformly distributed in the liquid xenon volume), with major γ ray features highlighted. As this spectrum takes into account the total energy deposition, including γ rays, the shape exhibits discontinuities corresponding to the typical β emission spectrum for each channel summed with the corresponding γ energy. This happens because in most of the decay events both the β and γ rays energy is deposited instantly. However, some of the higher-energy γ rays can escape the active region due to their large mean free path in the material, resulting in a larger contribution to the low-energy region from the β particles alone (this is especially important in the outer regions of the volume, where the probability of these γ rays escaping is larger).

The upper bound for ^{212}Pb activity in the LUX xenon, taken from ^{216}Po measured decay rates, is < 2.8 mBq [M$^+$14], but due to the $\sim$ 11 hour half-life of this isotope it is assumed that it is almost completely removed from xenon by the gas purifier system and is therefore excluded as a significant source of background.

Much like in the case of the ^{222}Rn chain, ^{212}Bi and ^{212}Po events overlap significantly due to the 0.3 μs half-life of the daughter isotope, resulting in no ^{212}Po events being reported [M$^+$14, Mal13]. ^{212}Bi also decays through α emission into ^{208}Tl with 35.94% probability and $Q = 6207.14 \pm 0.04$ keV but as such decay events are easily tagged, the only possible low-energy ER deposition is from the β particle emission of ^{208}Tl with 3.053 ± 4 minute half-life [Ako95]. However, ^{212}Bi activity in LUX xenon is significantly reduced by the removal of the parent isotope ^{212}Pb by the gas purifying system and is not considered in this work.

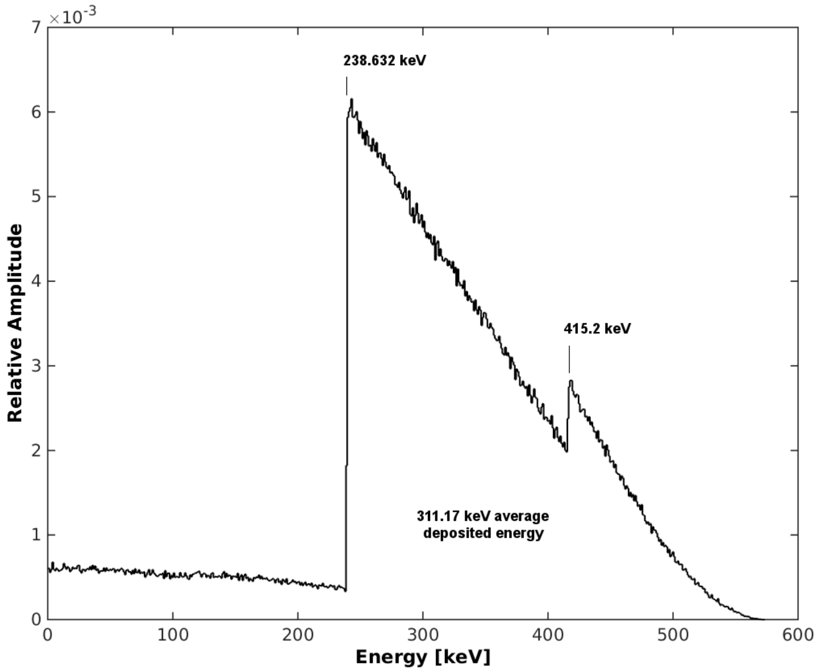

Figure 5.10: Total energy deposition spectrum for ^{212}Pb beta decay in 1 keV intervals (10^6 events) for a homogeneous distribution of decays in the entire liquid xenon volume of LUX. The total energy deposition accounts for γ ray absorption as well. This happens because in most of the decay events, both the β and γ rays deposit energy and at a close distance from the decay position.

Table 5.7: Main endpoint energies for ^{212}Pb β emission and associated γ ray energies, for semi-naked decays. The relative probability of each particle emission is also given.

$\mathbf{E}_\beta$ (keV)	P_β (%)	$\mathbf{E}_\gamma$ (keV)	P_γ (%)
158.53	5.17	415.2	0.143
335.17	82.5	238.632	43.3
573.8	12.3	-	-

5.5.1 Lead-214 and overall Radon activity in LUX

Using the Bateman equation, a mathematical model to describe the abundance evolution of isotopes in a decay chain based on the decay rates and initial abundances [Bat43], shown in 5.13, the activity evolution within a decay chain can be studied. This method can be implemented easily in computer code, but only if no two decay constants have a similar value, otherwise the results diverge. ^{214}Pb and ^{214}Bi have similar decay constants but the difference between them is acceptable and Bateman equation does not diverge.

$$N_n(t) = \prod_{j=1}^{n-1} \lambda_j \sum_{i=1}^{n} \sum_{j=i}^{n} \left(\frac{N_i(0) e^{-\lambda_j t}}{\prod_{p=i,p\neq j}^{n} (\lambda_p - \lambda_j)} \right) \tag{5.13}$$

The relevant data for all isotopes in the ^{222}Rn chain is shown in Table 5.8. It is considered that the only isotope[11] present inside the LUX target at the beginning of the run was ^{222}Rn, meaning that only the concentration of this source is relevant. According to [M$^+$14] the average activity for this isotope is 17.9 ± 0.2 mBq for the full active region.

Table 5.8: Data for isotopes within the Uranium series, from ^{222}Rn to ^{210}Pb. The average activity for the first isotope is 17.9 ± 0.2 mBq [M$^+$14]. All decay constants have distinct values and the Bateman equation can be used.

Isotope	half-life	decay constant (s^{-1})	decay mode
^{222}Rn	3.82 *d*	2.100×10^{-6}	α
^{218}Po	3.1 *min*	3.726×10^{-3}	α
^{214}Pb	26.8 *min*	4.311×10^{-4}	β
^{214}Bi	19.9 *min*	5.805×10^{-4}	β
^{214}Po	164.3 μs	4.219×10^{3}	α
^{210}Pb	22.2 *yr*	9.894×10^{-10}	β

Considering Eq. 5.13, one can obtain the plot shown in Figure 5.11, which shows the evolution over time of the relative concentration of those isotopes during the run 3 time span. Figure 5.12 shows the relative activity for the ^{222}Rn daughters during the run 3 length, considering that no radon was introduced in xenon during this time.

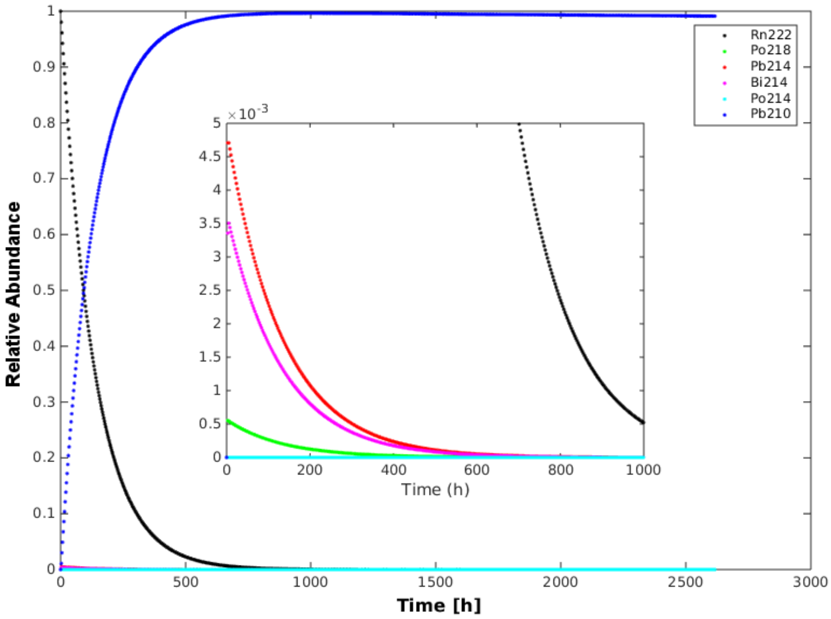

Figure 5.11: Relative concentration of radon-222 daughters down to ^{210}Pb during run 3. The inset is a detail of the relative concentration from short half-life isotopes. In particular, the ^{214}Po concentration quickly becomes insignificant due to its 164.3 μs half-life.

---

[11] For this chain in particular.

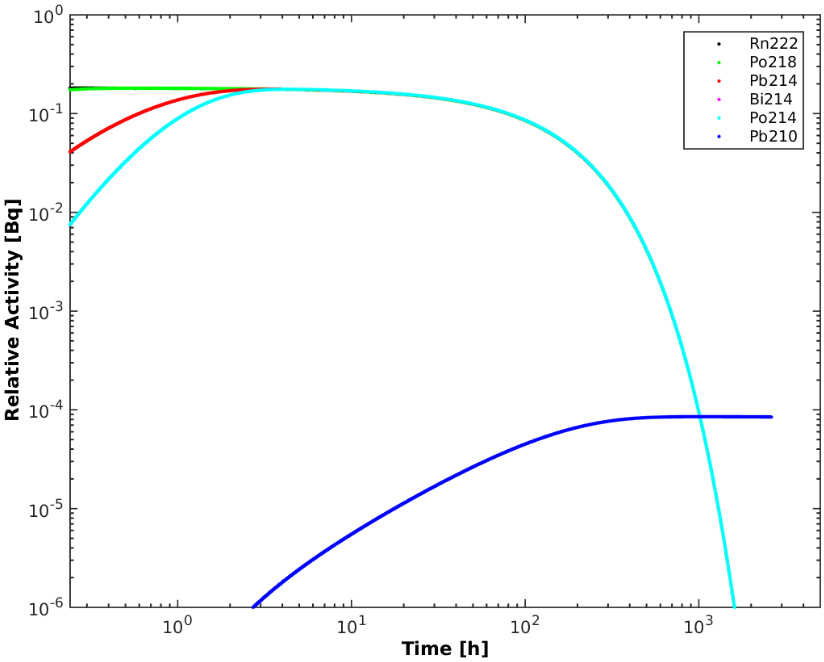

Figure 5.12: Relative Activity of radon-222 daughters down to ^{210}Pb during run 3. After just a few hours, considering that no more radon is added to the xenon, secular equilibrium is reached. The activity for all radon daughters down to ^{214}Po is virtually the same, meaning that it is possible to constrict the ^{214}Pb activity using the parent and daughter isotopes. It can also be seen that due to the very short half-life of ^{214}Po the superposition of the activity of this isotope with the one from ^{214}Bi is such that no data value can be seen for the latter. A very similar plot can be found in [Mal14].

Lead-214 Activity

In order to constrain the ^{214}Pb activity, the decay rates of the parent and daughter isotopes were measured using α particle decays signatures. Figure 5.12 shows that the secular equilibrium is reached very early in run 3, meaning that all radon daughters in the volume should have the same activity. This is not observed, however, as all α emitters have different measured decay rates [M$^+$14], and so measuring the activities for ^{218}Po and ^{214}Po gives upper and lower limits to the lead-214 activity. In the LUX active region, the expected ^{214}Pb activity is therefore in the 3.5 ± 0.1 $-$ 14.4 ± 0.2 mBq range, or in terms of detector mass between 13.95 ± 0.40 $-$ 57.39 ± 0.80 μBq kg^{-1}.

The value of 14.4 ± 0.2 mBq for ^{218}Po activity is $\sim$ 20% lower than the measured activity for ^{222}Rn, of 17.9 ± 0.2 mBq despite being neighbouring decays in this chain and secular equilibrium being reached very early in the run. Considering the 3.1 minute half-life of ^{218}Po, no purification process should remove a significant amount of this isotope from the active region to justify such difference [M$^+$14]. A possible explanation for this phenomenon may be ion mobility in regions of strong electric fields, mainly in the regions below the cathode and above the gate [Her14]. The electrical mobility is the ability of a charged particle to move through a medium in response to an electric field applied, and can be mathematically described as the ratio between the velocity of the particle across the medium and the magnitude of the electric field pulling the particle [HSK94]. As shown schematically in Figure 5.13, the circulation of liquid xenon inside the cryostat drags the impurities with it and when this flow reaches the cathode all positive-charged ions move towards it. Ions with less mobility are dragged further with the xenon circulation, resulting in a more uniform distribution in the xy plane, while ions with a high mobility reach the cathode faster and are retained closer to the xenon down flow edge. This results in the retaining of the impurities with high electric mobility below the active region of the detector and reducing the number of events that can be detected[12], resulting in less activity measured. Observing the different distributions of events in the xy plane for a given energy signature[13] means that the different ions present have distinct mobilities in liquid xenon. In Figure 5.14 the xenon flow is evident, as it shows the separation between the neighbouring decay events (^{222}Rn and ^{218}Po) by tagging the decay signatures of both isotopes and associating the respective position vertices, resulting in greater distances between the vertices of the 2 events where the flow is faster.

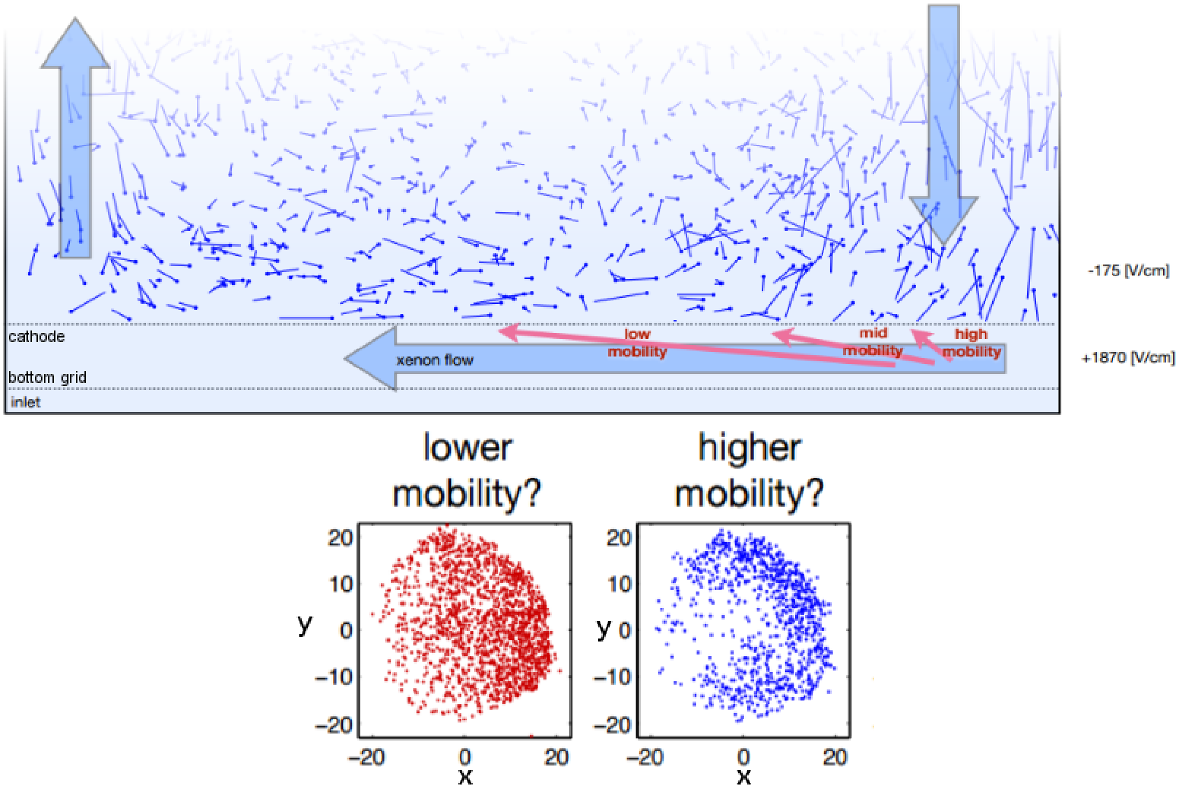

Figure 5.13: Representation of the expected behaviour of different ion species with different mobilities dragged by the liquid xenon flow below the cathode grid, in the reverse field region. The lower images are sets of data taken with S1 light only and using energy selection cuts to separate the contribution from each isotope. Different mobilities result in different distributions of events in the xy plane, but the low energy resolution makes isotope identification difficult. Images taken from [Her14].

---

[12] Below the cathode grid the electric field is reversed (reverse field region) and any ionization yield by an interaction in that region does not generate S2 signal. The primary scintillation is still detectable though.

[13] α decays are easily detected and measured using scintillation alone.

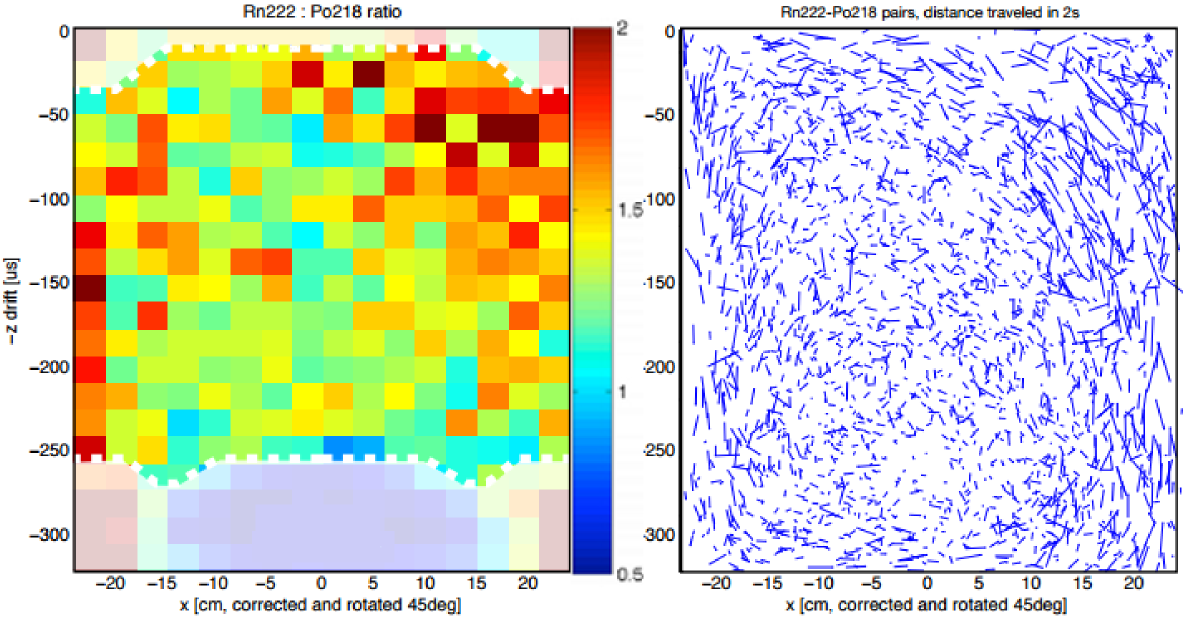

Figure 5.14: Left image: distribution of the ratio of ^{222}Rn/^{218}Po events in liquid xenon. Right image: separation between positions of neighbouring decay events for ^{222}Rn and ^{218}Po, distinguished by measuring the large S1 signal for the energetic α particles, resulting in greater distances between the vertices of the 2 events where the flow is faster. The x axis is rotated 45 degrees to be better aligned with the xenon convection, resulting in the downward flow being on the positive limit of the axis in both images. Images taken from [Her14].

Another constraint to the lead-214 activity is obtained by measuring the ER spectrum in a low-background 30 kg fiducial volume (in the center of the detector) and in the range of $300 - 350$ keV, using the nearby ^{127}Xe peaks to calibrate cut efficiencies and estimate ^{214}Pb activity. The energy range was chosen to avoid the 236 and 408 keV xenon-127 energy deposition peaks. To impose an upper limit, it is considered that no γ ray background is present in this region and energy range and that all the activity is due to ^{214}Pb alone. This results in an upper limit of < 32 μBq kg^{-1} at 90% confidence level. This is a much stronger upper limit than that obtained by α decay activities and it will be used in this work [M^{+}14].

In summary, with the collective analysis of ^{218}Po and ^{214}Po α decay rates and the ^{127}Xe activity comparison with ^{214}Pb background, the activity of this last source is bounded between $13.95 - 32$ μBq kg^{-1}, or for the entire active region between $3.5 \pm 0.1 \;\; - \;\; 8.0 \pm 0.8)$ mBq.

Events in the WIMP search Window

The fraction of ^{214}Pb events in the active region that fall into the WIMP search Window of $0.9 - 5.3$ keV$_{ee}$ and within the 118 kg fiducial volume is $P^{Pb214}_{FVWW} = 0.021912 \pm 0.000357\%$, taken directly from the β spectrum obtained with *LUXSim* and represented in Figure 5.9. In a 2×10^{7} event simulation where 17086486 ± 4134 events are measured in the active region, only 3744 ± 61

events fell into the search window. This number is relatively low and the statistical uncertainty is rather large.

For ^{214}Bi activity in LUX, considering the β spectrum and event distribution of this source, in a 1×10^6 event simulation where 854073 ± 924 events occur in the active region, only 125 ± 11 events fell into the search window, meaning that the fraction of events in the region of interest is $P^{Bi214}_{FVWW} = 0.014636 \pm 0.001288\%$. However, the 10% peak separation efficiency between the ^{214}Bi and ^{214}Po means that only this percentage of events is accounted for and so the percentage of measurable events would really be $P^{Bi214}_{FVWW} = (1.4636 \pm 0.1288) \times 10^{-3}\%$.

Figure 5.15 shows the difference between the radon-222 chain spectrum considering all decay events for all short-lived daughters (black) and Figure 5.16 shows the same spectrum with exclusion of 90% of ^{214}Bi and ^{214}Po decay events (blue), used to calculate the background rate in this work.

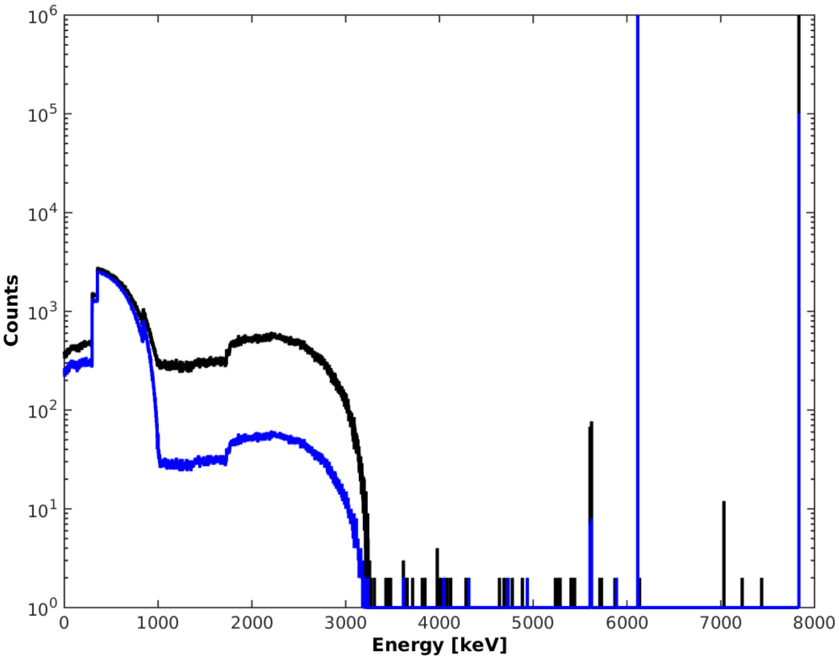

Figure 5.15: Deposited energy spectra for radon-222 events from ^{218}Po to ^{214}Po in the active volume, considering all events (black) and excluding 90% of both ^{214}Bi and ^{214}Po events due to event superposition in the LUX 1 ms event window (blue).

5.5.2 Radon-related Background Rates

Figure 5.17 shows total deposited energy in the entire detector volume, where one can also notice the gradient effect caused by the missing energy towards the detector borders from the escaping γ rays.

The event rate for ^{214}Pb in the active region and in the range $0.9 - 5.3$ keV$_{ee}$ is shown in

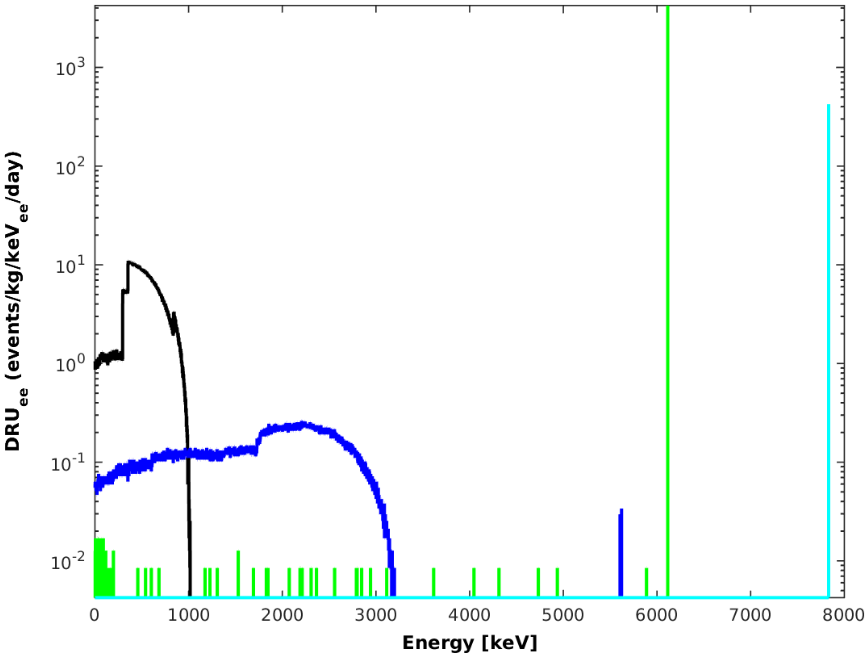

Figure 5.16: Contributions of the radon-222 daughters to the differential event rate in the active volume: ^{218}Po (green), ^{214}Pb (black), ^{214}Bi (dark blue), ^{214}Po (light blue), with exclusion of 90% of the events from both ^{214}Bi and ^{214}Po. In the WIMP search energy window of 0.9 – 5.3 keV the major contributor for ER events is ^{214}Pb.

Figure 5.18. The fiducial volume (represented by the dashed line) is set to a radius of 180 mm and height of 400 mm (from 70 mm to 470 mm above the bottom PMT bank) and contains $m_{FV} = 118.3 \pm 6.5$ kg of liquid xenon. It is clear that the semi-naked decay events dominate in the outer-most regions of the detector, where the energetic γ rays are more likely to escape the xenon volume and leave a low-energy deposition signature, resulting in the gradient effect observed.

The method used to obtain the differential BG rates is shown in Eq. 5.14.

$$dR_{Pb214} = \frac{A_{Pb214} \quad P^{Pb214}_{FVWW}}{m_{FV} \quad \Delta E_{WW}} \tag{5.14}$$

$$= 0.1273^{\pm 0.0079 sys}_{\pm 0.0021 stat} - 0.2910^{\pm 0.0332 sys}_{\pm 0.0047 stat} \mathrm{mDRU}_{ee} \tag{5.15}$$

where the average activity of ^{214}Pb is $3.5(1) < A_{Pb214} < 8.0(8) < 14.4(2)$ mBq, the calculated probability of a ^{214}Pb decay event falling into the WIMP search window and in the fiducial volume is $P^{Pb214}_{FVWW} = (2.1912 \pm 0.0357_{stat}) \times 10^{-4}$, obtained through *LUXSim* data, $m_{FV} = 118.3 \pm 6.5$ kg is the xenon mass in the fiducial volume and $\Delta E_{WW} = 4.4$ keV is the WIMP

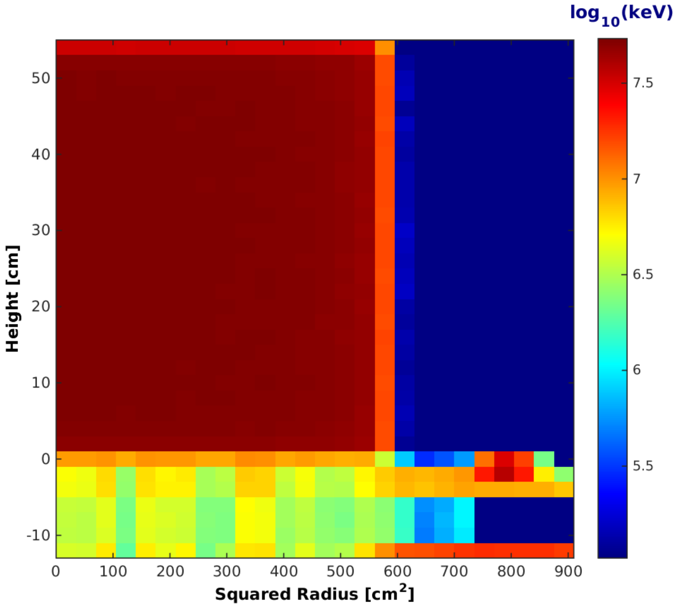

Figure 5.17: Geometric distribution of the deposited energy in the entire detector volume. ^{214}Pb has some energetic γ rays associated with the beta decay, and when these escape the detector the energy deposited due to the semi-naked β particle originates the low-energy signature responsible for the faint gradient effect closer to the detector edges.

energy window size.

Using the same method but with the data obtained for ^{214}Bi, specifically $A_{Bi214} = A_{Pb214}$ and $P^{Bi214}_{FVWW} = (1.4636 \pm 0.1288_{stat}) \times 10^{-5}$, the differential rate is:

$$dR_{Bi214} = 0.0085^{\pm 0.0005 sys}_{\pm 0.0008 stat} - 0.0194^{\pm 0.0022 sys}_{\pm 0.0017 stat} \mathrm{mDRU}_{ee} \tag{5.16}$$

The expected background rate for these two sources together, based on data analysis from *LUXSim*, for the WIMP search run is $0.1358^{\pm 0.0084 sys}_{\pm 0.0029 stat} - 0.3104^{\pm 0.0354 sys}_{\pm 0.0064 stat}$ mDRU$_{ee}$.

These values are somewhat different from those obtained in [M$^+$14], of $0.11 - 0.22$ mDRU$_{ee}$ for the analysis of ^{214}Pb alone. The calculated values are around $\sim 14\%$ and $\sim 24\%$ larger than the ones expected, for the lower and upper limits of the activity, respectively. This difference is even larger if the contribution from ^{214}Bi is considered. The uncertainties presented for the background rate are mostly from the uncertainties in the activity limits for ^{214}Pb and ^{214}Bi because of the large uncertainty in the measured ^{218}Po, ^{214}Po and ^{127}Xe activities given in [M$^+$14]. Furthermore, the uncertainty associated to the background rate for ^{214}Bi has a considerable contribution of the large uncertainty on the percentage P^{Bi214}_{FVWW} due to the low event statistics.

The background rate for this source was initially obtained by Malling and Bradley [Bra14, Mal13] considering that, of all ^{214}Pb activity, only *naked-β* decays contribute to the low-energy background. With a 9.2% branching ratio for the *naked-β* emission, the activity for this source

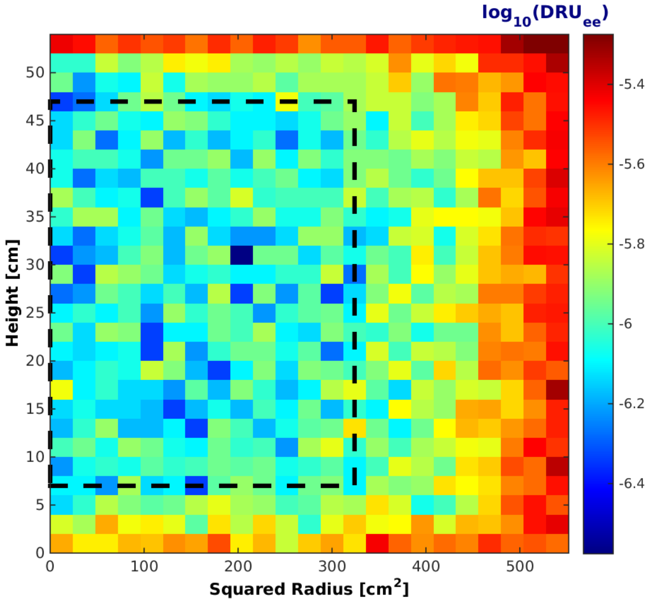

Figure 5.18: Background rate for ^{214}Pb in the LUX active region for energies between $0.9 - 5.3$ keV$_{ee}$. The dashed contour represents the fiducial volume and one can observe that the background relative to the semi-naked decay is insignificant due to the lower probability of a γ ray escaping. The lower rate obtained in the region of larger squared radii is due to the dodecahedral shape of the PTFE reflectors that limit the active region, resulting in a lower effective volume and thus lacking in number of events.

can be scaled to only consider these events. Furthermore, the fraction of events per unit of mass and energy that fall in a $M_{100kg} = 100$ kg fiducial volume, defined by $r < 17.5$ cm ; 12.5 cm $< Z < 47$ cm in [Mal13], but containing from geometry and liquid xenon density $\sim$ 95.9 kg, and in the range of $\Delta E_{0-5keV} = 0 - 5$ keV is given by $P_{100kg}^{0-5keV} = 1.3 \times 10^{-6}$ (^{214}Pb decays in 100 kg FV), obtained via *LUXSim* analysis of the beta spectrum [Mal13]. Scaling this to the entire active region, considered $M_{AV} = 270$ kg as in [Bra14], the expected range of rates of $0.10 - 0.41$ mDRU$_{ee}$ is obtained. The method can be summarized in Eq. 5.17.

$$dR = \frac{A_{Pb214} \times p(BR)_{naked-\beta} P_{100kg}^{0-5keV}}{\Delta E_{0-5keV}} \frac{M_{AV}}{M_{100kg}} \tag{5.17}$$

Where A_{Pb214} is ^{214}Pb activity and $p(BR) = 0.092_{naked-\beta}$ is the branching ratio of naked β decays.

This analysis is somewhat similar to the one used in this work, but uses some assumptions that may not be necessary, as the scaling of the activity to the naked-β decays. However, even in the same conditions as Malling and Bradley's work, the percentage of events given by P_{FVWW}^{Pb214} on Eq. 5.17 is also different than the one obtained in the studies for this work, being the latter of 1.0406×10^{-6}.

The method used in this work uses the official fiducial volume limits and ER energy range of run 3 and does not rely in any volume scaling or branching ratios. The spectrum of energy deposited per event, obtained via *LUXSim*, gives the number of events per source decay that fall into the fiducial volume and the WIMP search energy window, and it is the only required variable for the rate calculation. No errors were found in this analysis despite the rate values being different from those reported in [M^+14]. Nevertheless, this method is reliable and the results are compatible to the ones obtained in the previous reference.

The associated uncertainties in the rates obtained in this work are mostly due to the large uncertainty in the number of ^{214}Pb events expected for run 3, which in turn is due to the relatively large uncertainty in the measured ^{218}Po, ^{214}Po and ^{127}Xe activities as reported in [M^+14].

5.6 Gamma-rays from PMTs and construction materials

The signals arising from interaction in the active xenon volume of LUX are measured and recorded using two arrays of 61 photomultiplier tubes (PMT) each placed above and at the bottom of the active region [A$^+$12b].

All PMTs used in the experiment are 12-stage, 5.7 cm diameter Hamamatsu R8778 PMTs [A$^+$12c]. These were developed with the XMASS collaboration specifically for operating in LXe [A$^+$12b], being sensitive to the 178 nm scintillation light produced and being able to operate at LXe conditions, at temperatures of 170 K and pressures up to 5 atm.

The unstable isotopes ^{40}K, ^{60}Co, ^{232}Th and ^{238}U are present in PMT materials and detector construction materials, mainly the titanium vessels and copper parts. These isotopes can generate γ-rays capable of reaching the active region and deposit some energy, producing electron recoils (ER) and thus generating background signal. In particular, the latter two isotopes originate long lasting decay chains that produce several α, β and γ-emitting daughters. A more detailed description of these sources is found in Section 5.2.

As these different sources emit different types of radiation and with a very wide range of energies, the contribution to the spacial distribution of events is a function of the activity of each individual source, the type of radiation it emits and the position of the source. The "leakage" of events into the active volume is energy dependent, *i.e.* the more energetic the γ radiation a source can emit the bigger the mean free path of said radiation in liquid xenon will be and the probability of reaching further into the LXe volume increases. So if some sources reach further into the active volume than others, the different activities will have to be taken into account separately for each source in each region.

5.6.1 Activity of LUX materials in the WIMP search run

Samples of the main materials used in the construction of the LUX detector were tested to determine the total radioactivity yield within them. These tests were performed at the *Soudan Low-Background Counting Facility* (SOLO) and at the *Berkeley Oroville* facility [A$^+$11c]. The detector includes 231 kg of titanium for the inner and outer cryostat vessels and around 620 kg of copper in several components (mainly in the shields, PMT mounts and field shaping rings).

Measurement of activities from LUX materials

The inner and outer cryostat vessels are made of commercially pure titanium sheets selected from an extremely low-radioactivity batch. An 8.0 kg sample was tested at Oroville for 13 live days, yielding a total activity of < 12 mBq kg^{-1} from γ radiation measurements. Some of the measured activity comes from ^{46}Sc, but no energy deposition signatures were recorded in LUX for this source, probably due to shielding of inner materials [A$^+$11c].

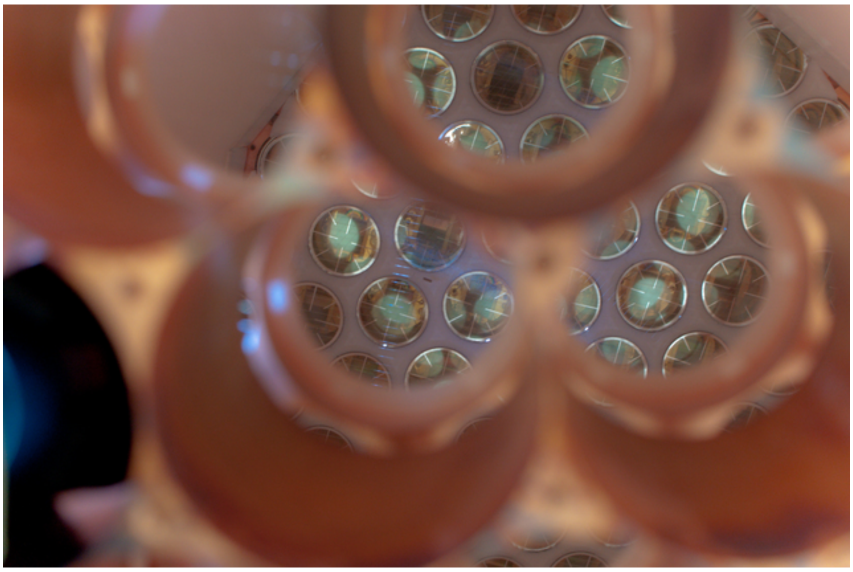

Figure 5.19: Top PMT array as seen from the holes of the opposite PMT holder (copper structure). These holes will support the other 61 PMTs of the bottom array. The volume between the two sets is the liquid xenon target yet to be filled and the only visible part of the PMTs is the window and photocathode with eight metal strips, or "fingers", placed radially in order to decrease the average cathode resistance and extend the operating temperature range [A+03]. This copper holder is made with top grade, very pure material to reduce the abundance of radioactive sources within. Figure taken from [Fah12].

Field shaping rings and PMT mounts are made of ultra-low-activity oxygen-free high-thermal conductivity copper. These components were tested at SOLO: a 15 kg sample of the copper used in the field shaping rings[14] tested during 9 live days, yielding an activity of $< 1.6 \ mBq;$ kg^{-1}, and a 1.1 kg sample of the copper used in the PMT mounts was tested during 5 live days, yielding an activity of < 5.8 mBq kg^{-1} [M+14]. The remaining copper structures were also tested at SOLO. Details of the screening values can be found in [M+14].

PMTs for LUX were also sampled for radioactivity measurements at SOLO. A total of 20 R8778 PMTs were screened in four batches of five unit each, with an average 9 live days per batch. The averaged results for each isotope found are listed in Table 5.9. Furthermore, studies of PMT activity were performed when the LUX detector was running.

Table 5.9: Results of the screening of 20 R8778 PMTs at SOLO. All PMTs were screened for four benchmark isotopes identified: ^{238}U, ^{232}Th, ^{40}K, and ^{60}Co. Separate columns are provided for completeness for "early" and "late" ^{238}U chain measurements, allowing for potential equilibrium breakage. Errors are statistical and quoted at $\pm 1\sigma$. Upper limits are given at 90% confidence level. Results are normalized *per* PMT for comparison [A+12c].

PMT	**Activity [mBq/PMT]**				
	^{238}U (^{234m}Pa)	^{238}U (^{226}Ra)	^{232}Th (^{228}Ra)	^{40}K	^{60}Co
R8778	< 22	9.5 ± 0.6	2.7 ± 0.3	66 ± 6	2.6 ± 0.2

---

[14] Approximately half the mass of this component.

The activity of each isotope in each region (top, bottom and sides) was varied independently in the simulations to obtain the best fit to the measured γ-ray spectrum as a function of position in the active region, excluding events below 500 keV$_{ee}$ to avoid ^{127}Xe influence. The obtained results are shown in Table 5.10.

Table 5.10: Screening estimates from SOLO and best-fit activity values for radioisotopes modelled in high-energy γ-ray analysis in LUX. Errors on the best-fit values are estimated to be 25%. Values taken from [M$^+$14].

Region	Isotope	Screening Estimate [Bq]	Best Fit [Bq]
Bottom	^{238}U	0.58 ± 0.04	0.62 ± 0.16
	^{232}Th	0.16 ± 0.02	0.23 ± 0.06
	^{40}K	4.0 ± 0.4	2.7 ± 0.7
	^{60}Co	0.16 ± 0.01	0.22 ± 0.06
Top	^{238}U	0.58 ± 0.04	0.87 ± 0.2
	^{232}Th	0.16 ± 0.02	0.25 ± 0.06
	^{40}K	4.0 ± 0.4	3.8 ± 1.0
	^{60}Co	0.16 ± 0.01	0.30 ± 0.08
Side	^{238}U	0.94 ± 0.14	0.22 ± 0.06
	^{232}Th	0.36 ± 0.07	1.50 ± 0.38
	^{40}K	1.4 ± 0.1	2.4 ± 0.6
	^{60}Co	–	0.36 ± 0.09

Some of the screening values are not consistent with LUX measurements. A reanalysis is ongoing where additional independent sources are thought to be contributing to the γ ray background in the lower detector volume. An additional source was proposed in the bottom copper shield volume to explain these excess events. This problem was not initially evident due to an offset error while converting drift time to depth in the active region, in the original 2013 analysis.

Processing *LUXSim* data

Potassium-40 and cobalt-60 undergo decays that ultimately result in stable states of ^{40}Ca or ^{40}Ar for the former and in ^{60}Ni for the latter. However both uranium-238 and thorium-232 originate a series of chained decays as discussed in Section 5.2, and so the activity and involved energies are due to the respective decay chains as a whole. *LUXSim DecayChain* generator distributes the total activity of one chain to each radioisotope in it.

Using the resulting output data from *LUXSim*, it is possible to reconstruct the simulated events to obtain energy depositions and corresponding positions. A Matlab converter bundles data from clusters of energy depositions due to secondary particle production in each event, weighting position-time distributions of energy deposition vertices and reconstructing them as one single energy deposition associated to an energy-averaged position and time. All step deposition vertices that are inside an acceptance region, defined by the pulse *xy* position separation efficiency and pulse drift time separation efficiency of the detector, are coupled together and recorded as one single interaction. If two energy deposition vertices are separated by a distance that would result in two separated S2 pulses for one S1 pulse being detected, the corresponding event is tagged as a multiple scatter and it is discarded promptly. This is to best mimic what the actual detector would record in one of these events.

5.6.2 Gamma Background Rate

Due to the lack of time and processing resources, the simulated data does not allow a complete background rate analysis, as these events are somewhat rare within the WIMP search energy window. To be able to study this background, the amount of data generated is insufficient and only with more computational power could this study be performed. For this reason, the γ ray background study presented in this work was made using the official simulated data for the background model used in the reanalysis of the run 3 of LUX[15].

Only the main contributions for this background were processed, namely the cryostat vessels, the top and bottom arrays of 122 PMTs (separately), the copper thermal shields, the copper PMT mounts and the Mylar sheets around the bodies of the PMTs. A list of the main γ ray sources for this background is presented in Table 5.11. The full list of the sources considered is shown in Appendix B.

Table 5.11: Activities and number of events simulated for the main γ ray sources considered in the background analysis, obtained from the official simulated data for the background model used in the reanalysis of run 03. The PMT arrays are the main contributors for the top and bottom regions, while the cryostat vessels are the main contributors for the sides of the detector. From the Uranium chain, only the daughters beyond ^{226}Ra were considered and the Thorium chain was analysed separating it in the "early" chain – from ^{232}Th to ^{228}Ac – and in the "late" chain – from ^{228}Ra to the stable ^{208}Pb (See Section A for more details of the decay chains). The isotope ^{46}Sc was set in the titanium cryostat despite no evidence of γ ray signatures being measured in LUX data [M+14]. The full list of γ ray sources considered can be found in Appendix B.

Component	Isotope	Activity [mBq]	Events simulated ($\times 10^3$)
Cryostat	^{40}K	369.6	27250
	^{226}Ra	85.47	58500
	^{46}Sc	1016.4	74750
	^{232}Th early	184.8	41250
	^{232}Th late	184.8	110000
Top PMT and bases	^{60}Co	160.43	23750
	^{40}K	4099.2	602250
	^{226}Ra	664.9	879750
	^{232}Th early	172.63	76500
	^{232}Th late	172.63	204000
Bottom PMT and bases	^{60}Co	160.43	23750
	^{40}K	4099.2	602250
	^{226}Ra	664.9	879750
	^{232}Th early	172.63	76500
	^{232}Th late	172.63	204000

---

[15] The simulated data and information were obtained from Brian Tennyson of *Yale University, CT, USA*.

Figure 5.20 represents the background differential rate of single scatter events in the target region, where the dashed rectangle delimits the fiducial volume. The white pixels that dominate in the innermost region of the detector indicate that no simulated energy deposition occurred at those positions. The fiducial volume is shielded from the γ rays by the outer layers of liquid xenon, resulting in less background events being recorded at the center.

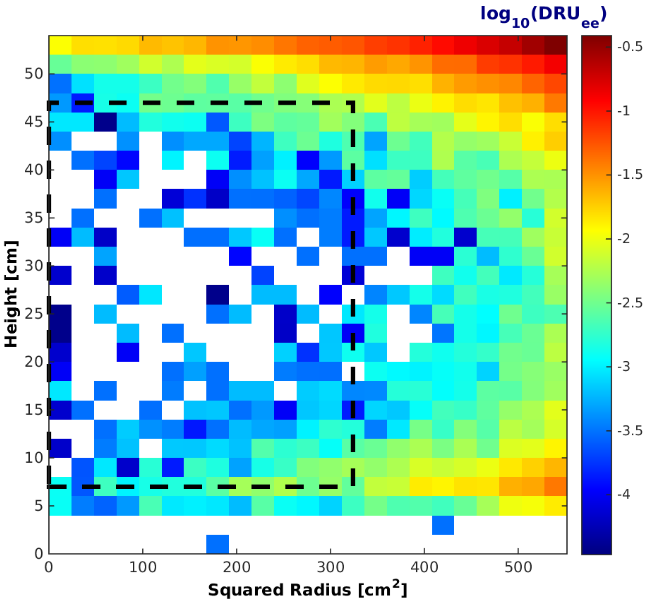

Figure 5.20: Simulated γ ray ER background rate in the range $0.9-5.3$ keV$_{ee}$ as a function of position. Rates are in units of $log_{10}(\mathrm{DRU}_{ee})$. The 118 kg fiducial volume used in the 85.3 day WIMP search run is overlaid as the black dashed contour. On this analysis only the main γ ray sources were considered.

The background rate is obtained directly from the simulated data by weighing the probability of an event reaching the 118.3 kg fiducial volume with the activities for each independent source. The resulting rate for these sources is:

$$\begin{aligned} dR &= \frac{1}{\Delta E \ \ m_{FV}} \sum_i A_i P^{\gamma}_{FVWW;i} \\ &= 0.9795 \pm 0.0538 \text{ mDRU}_{ee} \end{aligned} \tag{5.18}$$

where the sum is over all the different sources i, and $P^{\gamma}_{FVWW;i}$ is the fraction of events that fall into the FV and WIMP energy window for each source.

The rate obtained with this analysis is approximately half of the expected rate for this source according to [M$^+$14], with a value of $1.8 \pm 0.2_{stat} \pm 0.3_{sys}$ mDRU$_{ee}$. The reasons for this factor of 2 between the obtained and expected rates is not understood, and further analysis of this problem is required.

5.6.3 Xenon self shielding proprieties

As stated in Section 5.6.2, the simulated data did not allow a complete background rate analysis with the available computational resources because low-energy events from γ rays in the fiducial volume are somewhat rare, due to the self-shielding proprieties of liquid xenon. However, the data obtained can be used to illustrate this shielding effect.

Figure 5.21 represents the distributions of deposited energy produced by γ rays from 10^7 ^{40}K decay events simulated in all 122 PMT windows. The shielding provided by the dense liquid xenon is easily visible by the lack of single scatter events in the center of the detector, where the fiducial volume (dashed) is defined. The red dots represent the reconstructed energy depositions between $0.9-5.3$ keV$_{ee}$. Only 23 events produced by the 10^7 ^{40}K decays have energy depositions in the WIMP search energy window and in the 118 kg fiducial volume, proving that liquid xenon provides an important shielding of the internal volume where WIMPs are being searched.

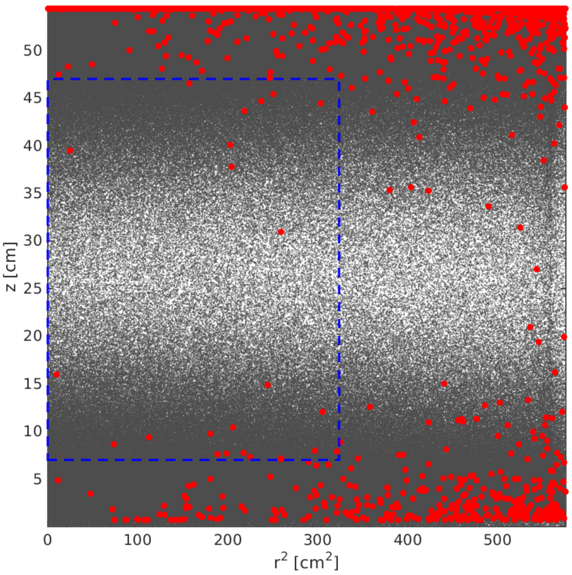

Figure 5.21: Energy depositions in the xenon volume from 10^7 ^{40}K decays on the top and bottom PMT arrays. The gray dots represent the position of all energy depositions reconstructed, while the red dots mark the positions of events with a single interaction and with reconstructed energy deposition inside the WIMP search energy window, of $0.9-5.3$ keV$_{ee}$. The dashed rectangle indicates the limits of the 118 kg fiducial volume.

From this analysis, the lack of statistical data to perform a γ ray background study is clear. Only around 2 decay events per million from ^{40}K alone can generate a signature that falls into the WIMP search window.

Chapter 6

Data analysis and WIMP detection efficiency

The efficiency to detect WIMP-like events is one of the most important parameters in dark matter experiments. The WIMP detection efficiency of LUX can be estimated by simulating the expected nuclear recoils produced by WIMP particles of different masses in the Xenon target. The WIMP generator used in *LUXSim* follows the same model described in Chapter 3.2 and by Lewin and Smith, allowing to study the hypothetical signal response of the detector to a real WIMP scatter event in Xenon. These events can then be processed using the same data processing and analysis chain as real data.

The efficiency is defined as the ratio between the number of "golden" events as selected by the analysis software and the number of WIMP events simulated, for the considered fiducial volume. A "golden" event is one for which a single S1 signal followed by a single valid S2 signal were produced, as expected from a single scatter event, meaning that the two can be paired to determine the recoil energy and position of the interaction[1].

The signals measured in the PMT arrays are recorded by the LUX data acquisition (DAQ) and trigger system to generate a pulse *timeline* 1 ms long, 500 μs on each side of the trigger signal, that can be processed using the data processing framework (DPF) to characterize each pulse and produce an output with a set of reduced quantities (RQs) wich can be used for higher level physical analysis [A$^+$12d, Col15a]. The DPF consists in a sequence of self-contained modules that perform predefined tasks such as calibration, pulse finding, classification and interaction vertex position reconstruction. The pulses are characterized as S1 signal, S2 signal, single photoelectron (SPE), single electron (SE) and unknown (if the pulse does not fit the requirements

---

[1] See Chapter 4 for a discussion of the S1 and S2 signals and Figure 4.2 for a schematic of the event reconstruction using these pulses.

of the previous categories).

The simulated data can be analysed in the same manner as the real LUX data. For that purpose, the output of *LUXSim* can be converted into *evt* files (see Section 5.1), that can be then processed by the DPF.

Figure 6.1 shows simulated NR spectra in xenon for interactions of WIMPs of different masses, obtained using the WIMP generator in *LUXSim*.

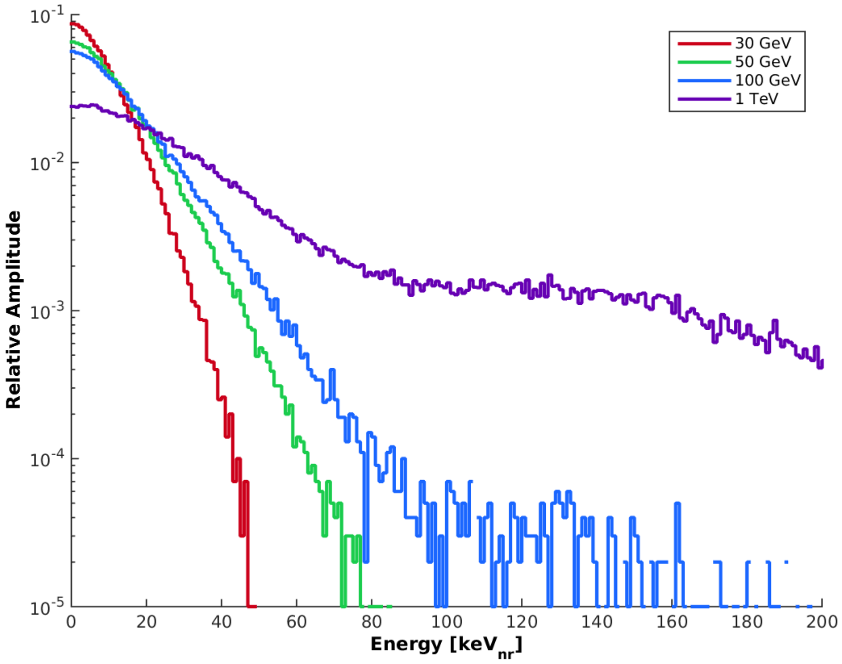

Figure 6.1: WIMP nuclear recoil spectra for different WIMP masses, obtained with the WIMP generator in *LUXSim*. These spectra are smooth and exponentially decreasing, as expected from Eq. 3.28. The 1 TeV spectrum (violet line) presents an interesting characteristic: around the 100 keV region one can see the damping effect of the form factor discussed in Section 3.2.1. The average energy deposited increases with increasing WIMP mass, with values of 8.1, 11.2, 13.8 and 44.6 keV for masses of 30 GeV, 50 GeV, 100 GeV and 1 TeV, respectively.

6.1 Detection Efficiency

In order to study the WIMP detection efficiency several simulations of WIMP NR in the fiducial volume alone were made using *LUXSim* and the WIMP generator for different WIMP masses. The simulated data was first processed to mimic real detector *timelines*, with S1 and S2 pulses, and then was processed as real data would be by the DPF to return the RQs. The resulting RQ files have the high level information that allows a proper reconstitution of the events.

Information from the original simulation can also be retrieved from the RQ files and serves as the control data. A *ROOT* [BR96] filtering algorithm is used to select the "golden" events and store only the relevant RQs into a single file for analysis. The data is then separated into 1 keV$_{nr}$ energy bins that are compared with the control data in order to obtain the ratio of "golden" events to total events per energy unit.

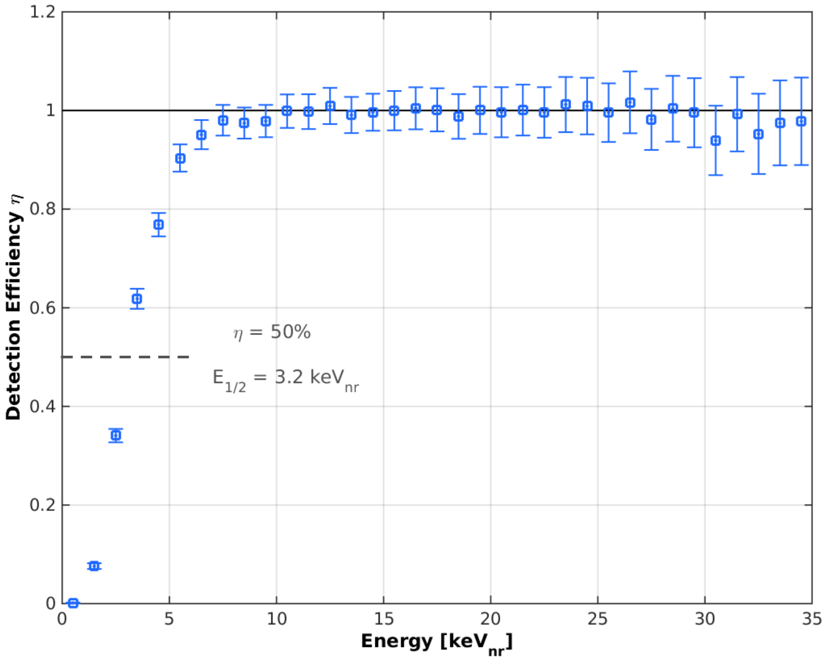

Figure 6.2: Simulated efficiency curve as function of nuclear recoil energy for single scatter events of a 100 GeV WIMP in the fiducial volume. The decreasing efficiency at lower energies is dominated by the S1 detection efficiency - see main text for discussion. For higher energies the efficiency becomes close to unity, as all events in the fiducial volume should be detected and provide the necessary characteristics to be tagged as "golden" events. The efficiency values presented here were normalized to unity at energies between 12 – 24 keV using the average efficiency in this range. This was necessary to account for a population of events, uniformly distributed across the entire energy range, for which the generated *timeline* was inconsistent with the position and energy deposited. The origin of this population is still being studied. See main text for more details.

The efficiency response of the detector is the convolution of all efficiency responses in each detection and signal processing step. The loss of efficiency at lower energies is dominated by the low detection efficiency of small S1 signals, either due to the low scintillation light yield, absorption of S1 light by the grids or reflectors, the event resulting in a single PMT response - PMTs are grouped together into 16 trigger channels with no adjacent PMTs belonging to the same group [A$^+$13e, Col15a] and if only one or two PMTs from the same channel detect the light signal from an event, that event is not considered "golden" - or misidentification of the pulse by the pulse finder or classifier algorithms. This lower efficiency is visible in Figure 6.2, obtained from the simulated data for a WIMP mass of 100 GeV.

The data points presented were normalized in order to set to unity the average value of efficiency in the range of $12 - 24$ keV, to compensate for a problem detected within the data, where the *timelines* for a population of events were not being properly generated or processed. A visual hand scan of the events excluded revealed that around 10% had a single pulse, similar to a large S1 that resulted in the event not being considered "golden" by the analysis chain. These events are similar to those obtained when simulating interactions in the region below the cathode grid, where the reverse field inhibits the formation of the S2 signal and only S1 light pulses are recorded, but as stated above, only events inside the FV were considered in this study. Furthermore, the fraction of excluded events is approximately the same as the volumetric fraction of liquid xenon below the cathode grid. A possible cause for this error could be a misidentification of the position vertex of the simulated single scatter due to an error in *LUXSim* or in the output converter. Some events, however, revealed good S1 and S2 pulse topologies that make them "golden" but were still missed by the pulse finder or pulse classifier, and contribute to the real efficiency loss.

LUXSim is part of a software repository used by the LUX collaboration and can undergo several changes made by the users, sometimes on a daily basis. No WIMP detection efficiency studies were performed by the analysis group with the version used in this analysis and there are no guaranties that the version is stable[2]. All simulated information was obtained with the same version of *LUXSim*, chosen at the beginning of this work, to ensure total consistency throughout this analysis.

An additional study with official NR simulated data was made to ensure that our normalization is indeed correct and that the low efficiency at higher energies is a problem of this particular *LUXSim* version. For this, a flat NR spectrum was used *i.e.*, each 0.25 keV$_{nr}$ energy bin has the same number of events. The official data did not include events with the same characteristics of those encountered in this work, and the efficiency curve obtained is used as a benchmark. The official efficiency curve processed with the same tools is represented in Figure 6.3.

If no fiducial cuts are set in the official data, the corresponding efficiency curve displays a behaviour similar to that obtained in this work prior to normalization, flattening out at $\sim 90\%$. This suggests that the population of bad events encountered could be the result of misidentification of the position vertex of the interaction as previously stated.

Figure 6.4 represents the detection efficiency for different WIMP masses ranging from 30 GeV to 1 TeV, as well as the combined plot for all WIMP masses in study. The presented curves

---

[2] The Noble Element Simulation Technique used by LUXSim is under continuous updating and could have directly affected the simulated data used in this work.

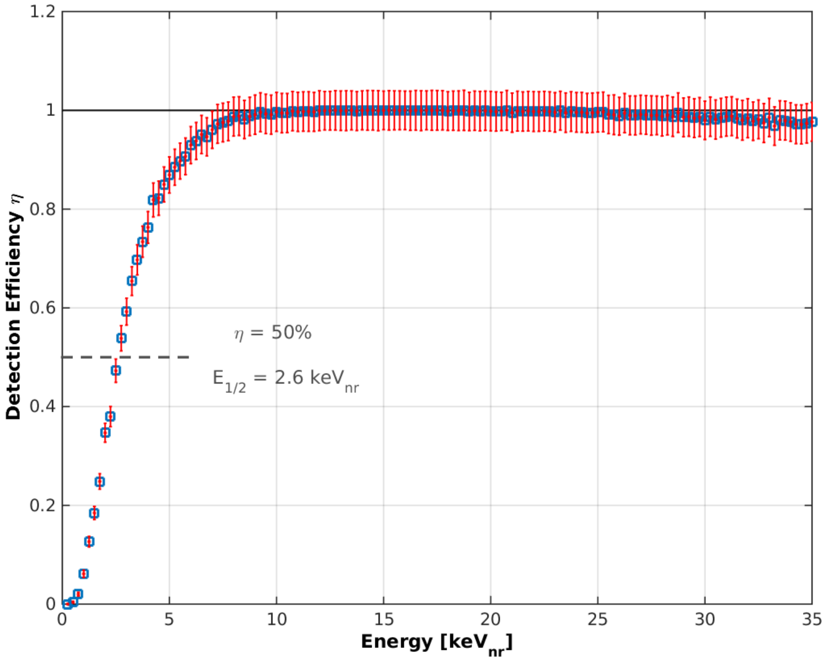

Figure 6.3: LUX NR detection efficiency as function of the recoil energy, produced from official simulation data, obtained using a different version of *LUXSim*. The efficiency was calculated using the same method and tools as the data generated in this work to demonstrate the validity of the processing tools developed. Each energy bin corresponds to 0.25 keV$_{nr}$. The curve displays the same behaviour as the one in this work after normalization. Notice that the efficiency is effectively unity above energies of 10 keV$_{nr}$ and begins to gently decrease above 25 keV$_{nr}$. This curve was not normalized.

are all equivalent both in shape and in efficiency values per energy bin. This means that the detection efficiency of LUX is independent of the WIMP mass, as expected, and depends mostly on the ability to successfully detect the S1 pulses from low-energy recoils. A detailed analysis of detection efficiency for S1 and S2 pulses is presented in [RL13].

LUX presents a high detection efficiency in the studied energy window of $3.4 - 25$ keV$_{nr}$. This high efficiency combined with background suppression results in increasing sensitivity to the rare nuclear recoils arising from dark matter particles.

6.2 WIMP nuclear recoil band

The ratio between primary scintillation and ionization produced in an interaction with a xenon atom differs from electron recoils to nuclear recoils, as stated in Chapter 4, usually being lower for nuclear recoils in comparison to electron recoils with the same energy transfer.

This separation relatively to the nature of the recoil becomes clear when analysing the S2/S1 ratio as function of the S1 signal. A $log(S2/S1) vs S1$ distribution will be different for nuclear and electron recoils, due to the different excitation channel yields in each case, and two distinct

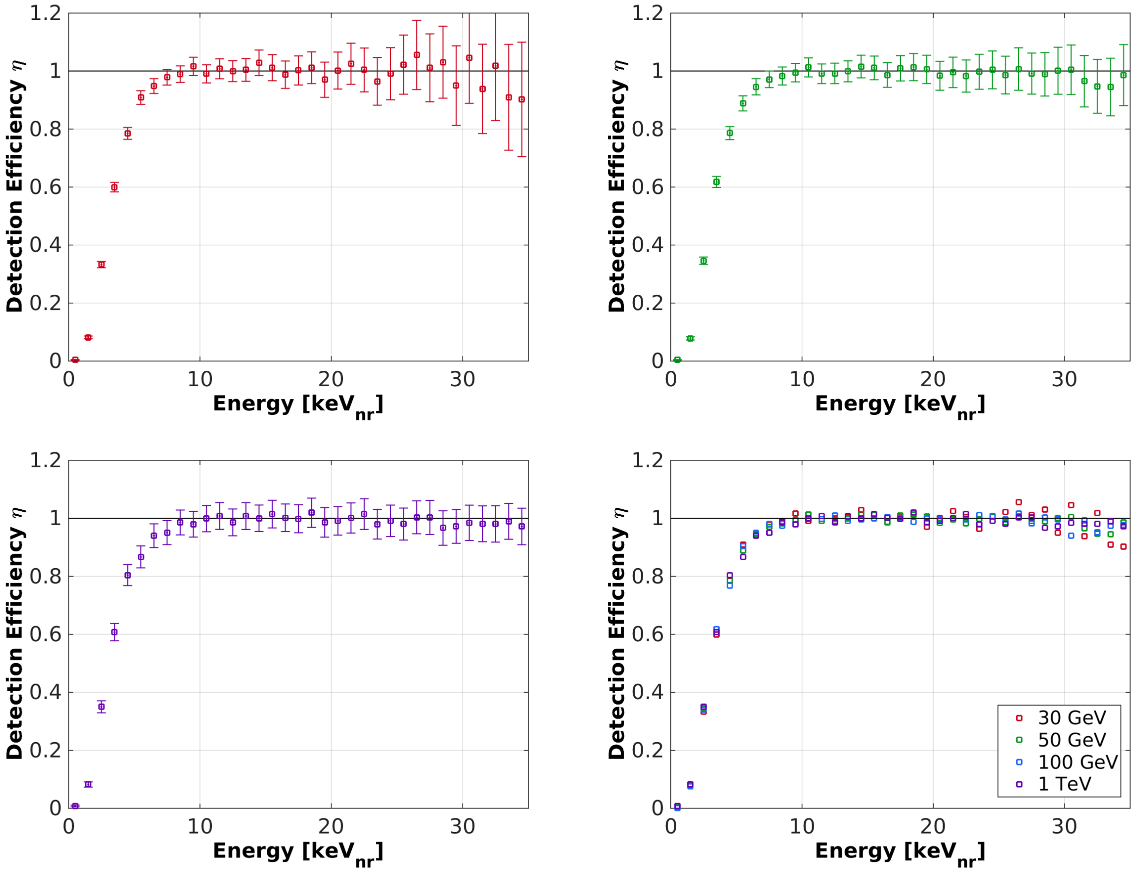

Figure 6.4: Simulated efficiency curves as function of recoil energy for WIMP masses of 30 GeV (red, top left), 50 GeV (green, top right) and 1 TeV (purple, bottom left). The bottom right plot is the combination of all four WIMP masses processed, including the 100 GeV samples displayed in Figure 6.2. For each energy sample the efficiency values are similar and all datasets present the same behaviour, decreasing at lower energies due to threshold effects and becoming stable and close to unity at higher energies. The fluctuations in the efficiency values are justified by statistical fluctuations in the data. In the last plot the error bars were removed to ease the comparison between the different datasets.

regions populated by the ER and NR distributions arise. This can be observed in Figure 6.5, where the black dots represent the distribution of ER events from the background sources studied in Chapter 5 and the density (coloured) regions represent the WIMP NR event distributions for masses of (from top to bottom) 10 GeV, 30 GeV and 100 GeV. A vertical separation is clear between the two data sets, as WIMP events occupy the (lower) NR band and background events are distributed in the (upper) ER band.

The background data used to generate the ER distribution corresponds to the expected background rates for 10 run 3 equivalent, or around 860 live days. All sources analysed in Chapter 5 were included: ^{85}Kr, ^{127}Xe, ^{214}Pb and γ-ray sources from construction materials. The background sources were weighed to account for the different activities and individual event rates obtained in the background modelling. The ER event distribution is the same for all the three plots in Figure 6.5, as the objective is to compare different NR distributions for different WIMP

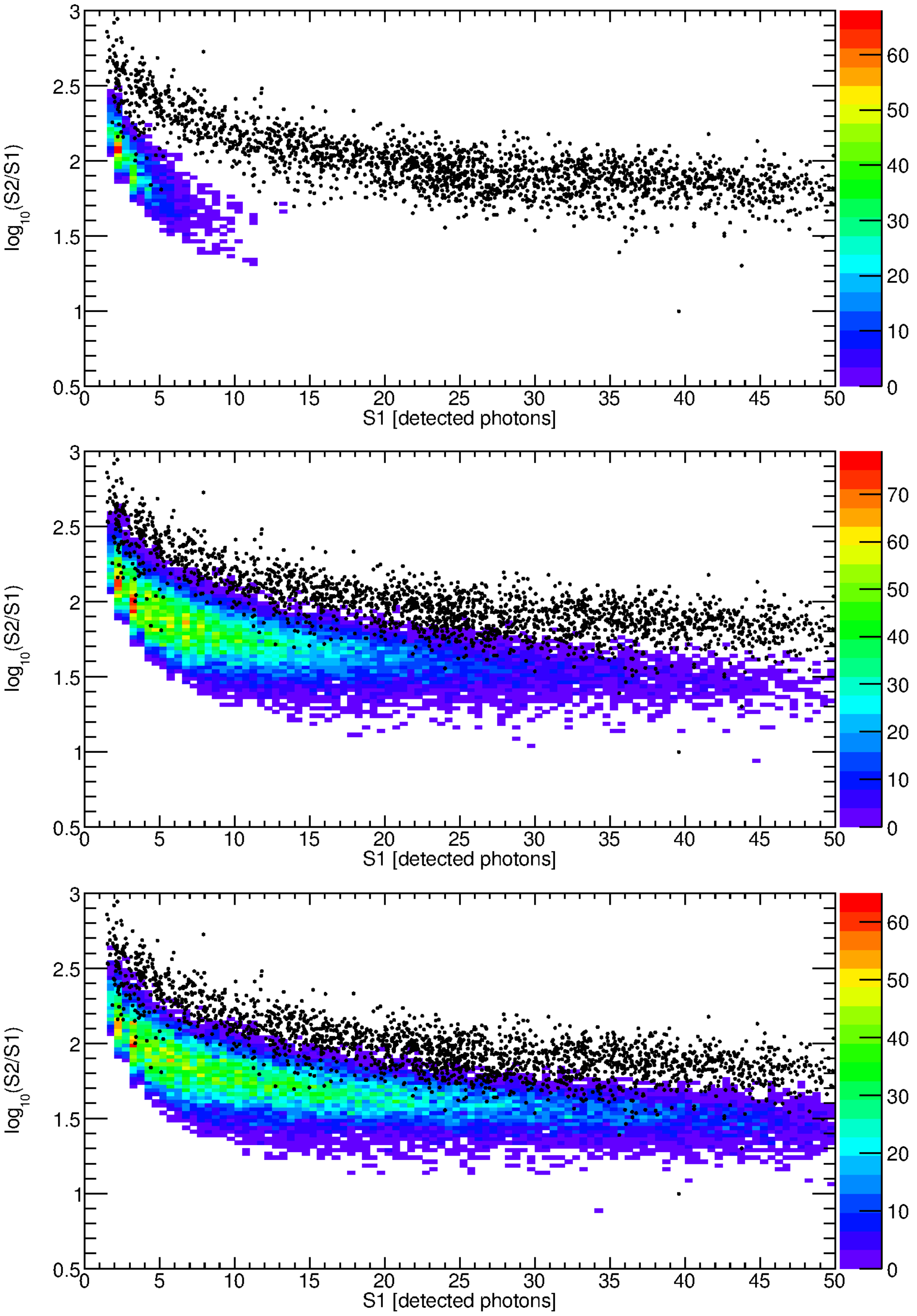

Figure 6.5: Relation between the S2 and S1 yields as function of the S1 signal (used as a proxy for deposited energy), for ER events from the simulated background sources in Chapter 5 (black dots) and NR events from simulated WIMP interactions (colour density distributions). Distributions for WIMP masses of 10 GeV, 30 GeV and 100 GeV are displayed in the top, middle and bottom figures, respectively. The background ER band and WIMP NR band profiles have a clear offset that can be used as a background discrimination technique (see Chapter 4). The background model presented in all plots is equivalent to approximately 860 live days, or 10 run 3 exposures, and includes ^{85}Kr, ^{127}Xe, ^{214}Pb and γ-ray sources in materials. The number of WIMP NR events in each plot is merely to represent the distribution profile and corresponds to 4×10^4 events simulated in the fiducial volume for each mass value. Some examples of the expected number of WIMP scatters for realistic interaction cross section values are presented in Table 6.1.

masses. A few background events spilled into the lower region of the plot in positions apparently not explainable by simple statistical fluctuations of the ER band. These events are being studied to understand why are they present at this stage.

WIMP particles with higher mass will transfer on average more energy in a scatter event, as can be seen in the WIMP NR spectra in Figure 6.1. The result is an extension of the NR band to higher energies for heavier WIMPs *i.e.*, on average more S1 (and S2) photons are produced per interaction. The profile of an eventual NR band arising from WIMP scattering events being recorded in a direct detection experiment, such as LUX, will allow the use of profile likelihood methods to best estimate the mass of the particle.

The CDMS II experiment claimed to have detected three WIMP-like events during the 2007 and 2008 final run of 140.2 kg-days [A$^+$13c]. A profile likelihood[3] analysis of the three events disfavoured the background-only scenario and returns the best likelihood for a WIMP of mass 8.6 GeV and WIMP-nucleon cross section of 1.9×10^{-41} cm^2. Such particles should also be detectable in LUX, as the sensitivity of LUX is higher than that of CDMS II by two orders of magnitude for this mass (see Figure 4.1).

For the WIMP mass and interaction cross section obtained by the CDMS II experiment, around 1550 WIMP events would be expected in the conditions of the LUX 85.3 days WIMP search run. Taking into consideration the 10 GeV WIMP mass as an approximation to the mass obtained by CDMS II, a distribution profile of events like the one in the top panel of Figure 6.5 is expected.

Figure 6.6 shows the official LUX WIMP search run detected "golden" events that passed all data processing and analysis cuts. The surviving events are consistent with the ER band (defined by the blue dashed lines and solid blue line for the ER median). The few events that fall below the NR median (red solid line) are consistent with statistical leakage from the ER band (for a discrimination of $(99.8 \pm 0.1_{sys})\%$ [Col15a]). This result is consistent with the background-only model.

Clearly, no WIMP-like events were seen during the first WIMP search run of LUX. There are no events in the region where 10 GeV WIMP event distribution profile is expected, despite the higher sensitivity of LUX. These results contradict the detection claims of CDMS II and other experiments (DAMA, CRESST and CoGeNT) for the described proprieties of a WIMP particle [B$^+$13, A$^+$13c].

Table 6.1 collects some examples of WIMP masses and realistic interaction cross sections, displaying for each case the expected number of NR events that would be observed in LUX during the 85.3 day WIMP search run. So far the best constrains on the WIMP-nucleon interaction cross section were set by LUX with a minimum upper-limit on the cross section of 7.6×10^{-46} cm^2 for a WIMP mass of 33 GeV [A$^+$13e]. The undergoing science run of LUX, with 300 day live time exposure and improved background reduction will further constrain the WIMP-nucleon interaction cross section.

---

[3] Although different from the method used by noble gas experiments for scintillation versus ionization yields, CDMS II semiconductors use profile likelihood of distinct nuclear recoil signatures in ionization and phonon yields.

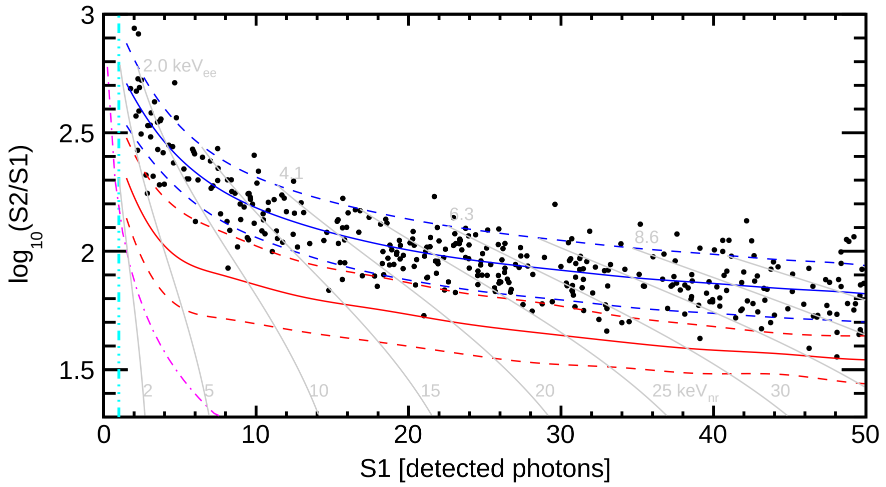

Figure 6.6: Official WIMP search run analysis plot of surviving events. The red dashed lines are 80% confidence limits for the NR band from distribution calibrations using a mono-energetic neutron source, with the median represented by the solid red line. The blue dashed lines are 80% confidence limits for the ER band obtained by calibration with γ ray sources, with the blue solid line representing the ER median. Grey lines represent iso-energy contours in both the ER and NR energy scales. A profile likelihood method was used to analyse the distribution and found it compatible with the background-only scenario. Figure taken from [Lin13].

Table 6.1: Expected number of WIMP NR events for different interaction cross section values and WIMP mass combinations, considering the same conditions as in the 85.3-day WIMP search run. If WIMP particles were to have the proprieties presented in the table, the current sensitivity of LUX would allow the detection of these particles. As it can be seen from Figure 6.6, no WIMP-like events were recorded during the LUX search run, excluding previous claims of WIMP direct detection.

WIMP mass (M_χ)	cross section ($\sigma_{0,Wn,SI}$)	Expected events	Reference	Notes
8.6 GeV	1.9×10^{-41} cm^2	1550	[A$^+$13c]	CDMS-II Si detection claim
10 GeV	1×10^{-41} cm^2	2700	-	as above but for a 10 GeV WIMP
1 TeV	1.9×10^{-44} cm^2	9	[A$^+$08]	Previous best limit for 1 TeV WIMPs (Xenon100)

Chapter 7

Conclusions

Dark matter search is one of the most exciting subjects being researched at the present time. New physics is being developed along with new techniques to probe the "dark sector" of the Universe and shed light on some of the most important mysteries of science today. The current motivation for dark matter search in direct detection experiments arises from the unambiguous evidence of dark matter as a main constituent of the unexplored content of the Universe.

LUX is a state of the art dark matter direct detection experiment that uses dual-phase xenon technology to search for rare nuclear recoils arising from WIMP interaction with the xenon atoms. The current best constraints on the WIMP-nucleon interaction cross section were provided by the LUX experiment in 2014 for a 85.3 day run, reaching an unprecedented sensitivity of 7.6×10^{-46} cm^2 [A$^+$13e].

The increased sensitivity of the LUX detector is the result of the improvements in background reduction, shielding and carefully selected instrumentation – such as the 122 custom Hamamatsu PMTs. The major background sources concerning LUX, and studied in this work, are ER events caused by γ and β rays from radioactive decays of naturally occurring or consmogenic activated isotopes in the detector internals.

A detailed analysis of the main internal radiation sources was performed, and extensive simulations were used to reproduce the results obtained in the official background analysis [M$^+$14]. The event rates presented on Chapter 5 are comparable and within the predicted uncertainties of the official analysis, except for the results obtained in the analysis of the γ ray background from construction materials, that presents a background rate approximately half of that expected from the background model. Due to the lack of computational resources and time, the γ ray background was studied using official simulation data for the background reanalysis of the 85.3 day WIMP search run. The problem was not yet identified and is being analysed. The method implemented for this background analysis is similar to the method used in the official analysis, and was reviewed by other collaboration members and acknowledged as functional. Therefore, the background analysis performed in this work provides a reliable demonstration of the background data processing methodology and explores the several considerations required to perform this task.

Table 7.1 summarizes the results obtained in this work for the background analysis of the 85.3 day WIMP search run and compares them with the results obtained in the official background analysis [M$^+$14].

Table 7.1: Results obtained for the simulated backgrounds in the LUX 118 kg fiducial volume during the 85.3 day WIMP search run, and comparison with the official predictions [M$^+$14].

Source	Background Rate [mDRU$_{ee}$]	Official Prediction [mDRU$_{ee}$]
^{85}Kr	0.1519 ± 0.0877	0.17 ± 0.10
^{127}Xe	0.440 ± 0.085	0.5 ± 0.1
^{214}Pb	$0.1273 - 0.2910$	$0.11 - 0.22$
γ rays	0.9795 ± 0.0538	1.8 ± 0.3
Total	1.8624 ± 0.1335	2.6 ± 0.4

The results obtained on Chapter 6 for the NR detection efficiency demonstrate the amazing sensitivity of the LUX detector and the ability to successfully detect WIMP-like events within the target xenon volume. The dual-phase xenon detector technology is very efficient at detecting the measurable excitation channels arising from particle interactions with the target material. The excellent background discrimination techniques further improve the sensitivity of the detector, resulting in increased sensitivity beyond any other dark matter direct detection experiment.

LUX is undergoing a final 300 live-days exposure that runs into 2015, with better background suppression, calibration and analysis techniques that will allow LUX to surpass the sensitivity of the first WIMP search run by a factor of around five [Gha14].

The LUX-ZEPLIN (LZ) experiment will operate with a 7 tonne liquid xenon active region, replacing LUX on the Davis Campus at SURF and reuse some of the existing structures, such as the water tank. The next generation LZ detector will be a scale up of the LUX detector, with a fiducial target mass $\sim$ 45 times the mass used in the FV of LUX. The projected sensitivity for LZ is of 10^{48} cm^2 for a full 1000-day exposure, exploring the electroweak parameter space beyond any other dark matter experiment [A$^+$11b, Gha14].

The aptitudes and skills developed during this work are a major contribution to the overall scientific achievements and training and for a future career in scientific research. The development of technical skills such as data processing, on-site training at research facilities and detector management tasks are a valuable asset for future work in LUX or in a next generation dark matter direct detection experiment, like the LZ experiment. Soft skills obtained through teamwork, integration into a major scientific collaboration, the responsibility of maintaining an integral part of the simulation, as the *LUXSimMatlabReader* manager, and scientific outreach also improved the overall scientific training.

List of Figures

List of Tables

References

[A$^+$03] H.M. Araujo et al. Low-temperature study of 35 photomultiplier tubes for the ZEPLIN III experiment. *Nucl. Inst. Meth. in Phys. Res. A 521*, pages 407–415, October 2003.

[A$^+$07] D. Yu Akimov et al. The ZEPLIN-III dark matter detector: instrument design, manufacture and commissioning. *Astropart. Phys.*, 27:46–60, 2007. doi:10.1016/j.astropartphys.2006.09.005.

[A$^+$08] J. Angle et al. First Results from the XENON10 Dark Matter Experiment at the Gran Sasso National Laboratory. *Phys. Rev. Lett.*, 100, 2008. doi:10.1103/PhysRevLett.100.021303.

[A$^+$10] Z. Ahmed et al. Dark Matter Search Results from the CDMS II Experiment. *Science*, 327:1619, 2010. doi:10.1126/science.1186112.

[A$^+$11a] N. Ackerman et al. Observation of Two-Neutrino Double-Beta Decay in ^{136}Xe with EXO-200. *Phys. Rev. Lett.*, 107:212501, 2011. doi:10.1103/PhysRevLett.107.212501.

[A$^+$11b] D.S. Akerib et al. After LUX: The LZ Program. *Astro-ph.IM*, October 2011. arXiv:1110.0103.

[A$^+$11c] D.S Akerib et al. Radio-assay of Titanium samples for the LUX experiment. *phisics.ins-det*, 2011. arXiv:1112.1376.

[A$^+$11d] E. Aprile et al. Design and Performance of the XENON10 Dark Matter Experiment. *Astropart. Phys.*, 34:679–698, 2011. doi:10.1016/j.astropartphys.2011.01.006.

[A$^+$12a] Georges Aad et al. Observation of a new particle in the search for the Standard Model Higgs boson with the ATLAS detector at the LHC. *Phys. Lett.*, B716:1–29, 2012. doi:10.1016/j.physletb.2012.08.020.

[A$^+$12b] D.S. Akerib, , et al. The Large Underground Xenon (LUX) Experiment. *physics.ins-det*, November 2012. doi:10.1016/j.nima.2012.11.135.

[A+12c] D.S. Akerib et al. An Ultra-Low Background PMT for Liquid Xenon Detectors. *Nucl. Inst. Meth. A.*, November 2012. 10.1016/j.nima.2012.11.020.

[A+12d] D.S. Akerib et al. Data acquisition and readout system for the LUX dark matter experiment. *Nucl. Inst. Meth. in Phys. Res. A*, 668:1–8, 2012. doi:10.1016/j.nima.2011.11.063.

[A+12e] D.S. Akerib et al. LUXSim: A component-centric approach to low-background simulations. *Nucl. Inst. Meth. in Phys. Res. A*, 675:63–77, May 2012. doi:10.1016/j.nima.2012.02.010.

[A+12f] E. Aprile et al. Dark Matter Results from 225 Live Days of XENON100 Data. *Phys. Rev. Lett.*, 109, 2012. doi:10.1103/PhysRevLett.109.181301.

[A+13a] Georges Aad et al. Search for dark matter candidates and large extra dimensions in events with a jet and missing transverse momentum with the ATLAS detector. *JHEP*, 04:075, 2013. doi:10.1007/JHEP04(2013)075.

[A+13b] Georges Aad et al. Search for dark matter candidates and large extra dimensions in events with a photon and missing transverse momentum in *pp* collision data at $\sqrt{s} = 7$ TeV with the ATLAS detector. *Phys. Rev. Lett.*, 110(1):011802, 2013. doi:10.1103/PhysRevLett.110.011802.

[A+13c] R. Agnese et al. Silicon Detector Dark Matter Results from the Final Exposure of CDMS II. *Phys. Rev. Lett.*, 111(25):251301, 2013. doi:10.1103/PhysRevLett.111.251301.

[A+13d] J. Ahlswede et al. Update and improvement of the global krypton-85 emission inventory. *Journal of Environmental Radioactivity*, (115):34–42, November 2013. doi:10.1016/j.jenvrad.2012.07.006.

[A+13e] D.S. Akerib et al. First results from the LUX dark matter experiment at the Sanford Underground Research Facility. *Astro-ph.CO*, October 2013. arXiv:[1310.8214v1].

[A+13f] E. Aprile et al. Limits on Spin-Dependent WIMP-Nucleon Cross Sections from 225 Live Days of XENON100 Data. *Phys. Rev. Lett.*, 111:021301, 2013. doi:10.1103/PhysRevLett.111.021301.

[A+14] Georges Aad et al. Search for dark matter in events with a hadronically decaying W or Z boson and missing transverse momentum in *pp* collisions at $\sqrt{s} = 8$ TeV with the ATLAS detector. *Phys. Rev. Lett.*, 112(4):041802, 2014. doi:10.1103/PhysRevLett.112.041802.

[A+15] Georges Aad et al. Search for Dark Matter in Events with Missing Transverse Momentum and a Higgs Boson Decaying to Two Photons in *pp* Collisions at $\sqrt{s} = 8$ TeV with the ATLAS Detector. *ArXiv e-prints*, 2015. arXiv:1506.01081.

[ABB+15] A. Arinc, M.M. Bé, E. Browne, et al. Atomic and Nuclear Data - Recommended Data, 2015. `http://www.nucleide.org` - accessed 2 June 2015.

[AFZ06] G.W. Angus, B. Famaey, and H.S. Zhao. Can MOND take a bullet? Analytical comparisons of three versions of MOND beyond spherical symmetry. *Mon. Not. Roy. Astron. Soc.*, 371:138–146, 2006. doi:10.1111/j.1365-2966.2006.10668.x.

[AH48] R.A. Alpher and R.C. Herman. On the Relative Abundance of the Elements. *Phys. Rev.*, 74:1737–1742, 1948. doi:10.1103/PhysRev.74.1737.

[Ako95] Y.A. Akovali. Table of Radioactive Isotopes - Lead-214, 1995. `http://ie.lbl.gov/toi/nuclide.asp?iZA=830214` - accessed 04 April 2015.

[Asa] Makoto Asai. GEANT4 tutorial course - Particle Gun. `http://geant4.slac.stanford.edu/SLACTutorial09/ParticleGun.pdf` - accessed 20 July 2015.

[Ati13] Dobi Atila. Fiducial Mass from Tritium. Internal LUX Collaboration document, 2013.

[B$^+$03] R. Bernabei et al. Dark matter search. *Riv. Nuovo Cim.*, 26N1:1–73, 2003. arXiv:astro-ph/0307403.

[B$^+$06] C. A. Baker et al. Improved Experimental Limit on the Electric Dipole Moment of the Neutron. *Phys. Rev. Lett.*, 97:131801, 2006. doi:10.1103/PhysRevLett.97.131801.

[B$^+$12a] E. Behnke et al. First dark matter search results from a 4-kg CF_3I bubble chamber operated in a deep underground site. *Physical Review D.*, 86(5):052001, 2012. doi:10.1103/PhysRevD.86.052001.

[B$^+$12b] J. Beringer et al. Review of Particle Physics. *Phys. Rev. D*, 86:010001, 2012. doi:10.1103/PhysRevD.86.010001.

[B$^+$12c] J. Bovy et al. The Milky Way's Circular-velocity Curve between 4 and 14 kpc from APOGEE data. *Astrophys. J.*, 759:131, 2012. doi:10.1088/0004-637X/759/2/131.

[B$^+$13] R. Bernabei et al. Final model independent result of DAMA/LIBRA-phase1. *European Physical Journal C*, 73:2648, 2013. doi:10.1140/epjc/s10052-013-2648-7.

[Bat43] H. Bateman. Solution of a system of differential equations occurring in the theory of radioactive transformations. *Proceedings of the Cambridge Philosophical Society, Mathematical and physical sciences*, 15, 1843.

[BBS$^+$07] A.I. Bolozdynya, P.P. Brusov, T. Shutt, C.E. Dahl, and J. Kwong. A chromatographic system for removal of radioactive 85Kr from xenon. In *Proceedings of the 11th Symposium on Radiation Measurements and Applications*, volume 579, pages 50 – 53, 2007. doi:10.1016/j.nima.2007.04.011.

[BCnG10] Gianfranco Bertone, David G Cerdeño, and Anne M. Green. *Particle Dark Matter: Observations, Models and Searches*, chapter 17, pages 347–369. Cambridge University Press, 2010. ISBN:9780521763684.

[BFH10] Yang Bai, Patrick J. Fox, and Roni Harnik. The Tevatron at the Frontier of Dark Matter Direct Detection. *JHEP*, 12:048, 2010. doi:10.1007/JHEP12(2010)048.

[BHS$^+$98] M.J. Berger, J.H. Hubbell, S.M. Seltzer, J. Chang, J.S. Coursey, R. Sukumar, D.S. Zucker, and K. Olsen. XCOM: Photon Cross Sections Database. NIST, PML, Radiation Physics Division, 1998. `http://www.nist.gov/pml/data/xcom/index.cfm` - accessed 20 July 2015.

[BHS05] G. Bertone, D. Hooper, and J. Silk. Particle dark matter: evidence, candidates and constraints. *Phys. Rep.*, 405:279–390, 2005. doi:10.1016/j.physrep.2004.08.031.

[BKPS15] L. Baudis, A. Kish, F. Piastra, and M. Schumann. Cosmogenic activation of xenon and copper. *astro-ph.IM*, July 2015. arXiv:1507.03792.

[BR96] Rene Brun and Fons Rademakers. ROOT - An Object Oriented Data Analysis Framework. *Nucl. Inst. Meth. in Phys. Res. A*, 389:81–86, 1996. `http://root.cern.ch/`.

[Bra14] A.W. Bradley. *LUX thermosyphon cryogenics and Radon-related Backgrounds for the first WIMP result.* PhD thesis, Department of Physics, Case Western Reserve University, May 2014.

[C$^+$10] S. Cebrian et al. Cosmogenic activation in germanium and copper for rare event searches. *Astropart. Phys.*, 33:316–329, 2010. doi:10.1016/j.astropartphys.2010.03.002.

[C$^+$12] Serguei Chatrchyan et al. Search for dark matter and large extra dimensions in monojet events in pp collisions at $\sqrt{s} = 7$ TeV. *JHEP*, 09:094, 2012. doi:10.1007/JHEP09(2012)094.

[CBG$^+$06] Douglas Clowe, Maruša Bradač, Anthony H. Gonzalez, Maxim Markevitch, Scott W. Randall, Christine Jones, and Dennis Zaritsky. A Direct Empirical Proof of the Existence of Dark Matter. *Astrophys. J.*, 648(2):L109, 2006. doi:10.1086/508162.

[CCP06] Giacomo Cacciapaglia, Csaba Csaki, and Seong Chan Park. Fully radiative electroweak symmetry breaking. *JHEP*, 03:099, 2006. doi:10.1088/1126-6708/2006/03/099.

[CCRS15] Rodrigo C.V. Coelho, Maurício O. Calvão, Ribamar R.R. Reis, and Beatriz B. Siffert. Standardization of type Ia supernovae. *Eur. J. Phys.*, 36:015007, 2015. doi:10.1088/0143-0807/36/1/015007.

[Cha14] Jeremy Chapman. LUX Run03 Dark Matter Limit Plots (Full up to date set). Internal LUX Collaboration document, 2014.

[CHL15] Eric Carlson, Dan Hooper, and Tim Linden. Improving the Sensitivity of Gamma-Ray Telescopes to Dark Matter Annihilation in Dwarf Spheroidal Galaxies. *Phys. Rev.*, D91(6):061302, 2015. doi:10.1103/PhysRevD.91.061302.

[CK09] Robert Caldwell and Marc Kamionkowski. Cosmology: Dark matter and dark energy. *Nature*, 458:587–589, 2009. doi:10.1038/458587a.

[Coc13] Alain Coc. Primordial Nucleosynthesis. *Journal of Physics: Conference Series*, 420(1):012136, 2013.

[Col15a] LUX Collaboration. LUX Run03 results comprehensive paper. Internal LUX Collaboration document, 2015.

[Col15b] Planck Collaboration. Planck mission Picture Gallery. `http://www.cosmos.esa.int/web/planck/picture-gallery`, 2015. accessed 10 August 2015.

[Com] Wikipedia Commons. Nuclear Binding Energy curve. `https://commons.wikimedia.org/wiki/File:Binding_energyBA.jpg` - accessed 31 July 2015.

[CPT92] S.M. Carroll, W.H. Press, and E.L. Turner. The cosmological constant. *Ann. Rev. Astron. Astrophys.*, 30:499–542, 1992. doi:10.1146/annurev.aa.30.090192.002435.

[Cun15] J.L.P. Cunha. Tópicos de Astrofísica Moderna. Class Material for the Topics of Modern Astrophysics Course [MAIE], University of Coimbra, 2015.

[End93] P.M. Endt. Table of Radioactive Isotopes - Cobalt-60, 1993. `http://ie.lbl.gov/toi/nuclide.asp?iZA=270060` - accessed 04 April 2015.

[End00] P.M. Endt. The Berkeley Laboratory Isotopes Project, May 2000. `http://ie.lbl.gov/education/isotopes.htm` - accessed 10 May 2015.

[ESW07] Daniel J. Eisenstein, Hee-jong Seo, and Martin J. White. On the Robustness of the Acoustic Scale in the Low-Redshift Clustering of Matter. *Astrophys. J.*, 664:660–674, 2007. doi:10.1086/518755.

[Eva93] N. W. Evans. Simple galaxy models with massive haloes. *Mon. Not. Roy. Astron. Soc.*, 260(1):191–201, 1993. doi:10.1093/mnras/260.1.191.

[F^+01] Wendy L. Freedman et al. Final Results from the Hubble Space Telescope Key Project to Measure the Hubble Constant. *Astrophys. J.*, 553(1):47, 2001. doi:10.1086/320638.

[Fah12] C. Faham. Photo galleries from construction, installation and operation of LUX. Internal LUX Collaboration document, 2012.

[Fah14] C.H. Faham. *Prototype, Surface Commissioning and Photomultiplier Tube Characterization for the Large Underground Xenon (LUX) Direct Dark Matter Search Experiment.* PhD thesis, Physics department at Brown University, Providence, Rhode Island, May 2014.

[Fri99a] A. Friedmann. On the Curvature of Space. *General Relativity and Gravitation*, 31(12):1991–2000, 1999. doi:10.1023/A:1026751225741.

[Fri99b] A. Friedmann. On the Possibility of a World with Constant Negative Curvature of Space. *General Relativity and Gravitation*, 31(12):2001–2008, 1999. doi:10.1023/A:1026755309811.

[FRS$^+$14] G. W. Fraser, A. M. Read, S. Sembay, J. A. Carter, and E. Schyns. Potential solar axion signatures in X-ray observations with the XMM–Newton observatory. *Mon. Not. Roy. Astron. Soc.*, 445(2):2146–2168, 2014. doi:10.1093/mnras/stu1865.

[FT13] C. Fry and M. Thoennessen. Discovery of actinium, thorium, protactinium, and uranium isotopes. *Atomic Data and Nuclear Data Tables*, 99(3):345 – 364, 2013. doi:10.1016/j.adt.2012.03.002.

[Gam48] G. Gamow. The Origin of Elements and the Separation of Galaxies. *Phys. Rev.*, 74:505–506, 1948. doi:10.1103/PhysRev.74.505.2.

[GGRZ04] M.S. Gordon, P. Goldhagen, K.P. Rodbell, and T.H. Zabel. Measurement of the flux and energy spectrum of cosmic-ray induced neutrons on the ground. *Nuclear Science, IEEE Transactions*, 51(6):3427 – 3434, December 2004. doi:10.1109/TNS.2004.839134.

[GGT95] Evalyn I. Gates, Geza Gyuk, and Michael S. Turner. The Local halo density. *Astrophys. J.*, 449:L123–L126, 1995. doi:10.1086/309652.

[Gha14] Chamkaur Ghag. The LUX direct dark matter search experiment. *arXiv e-prints*, 2014. arXiv:1412.4660.

[Hel56] R. H. Helm. Inelastic and Elastic Scattering of 187-Mev Electrons from Selected Even-Even Nuclei. *Phys. Rev.*, 104:1466–1475, 1956. doi:10.1103/PhysRev.104.1466.

[Her14] S. Hertel. Where is Po218 going? Internal LUX Collaboration document, February 2014.

[HKRR13] W. Hillebrandt, M. Kromer, F.K. Röpke, and A.J. Ruiter. Towards an understanding of Type Ia supernovae from a synthesis of theory and observations. *Frontiers of Physics*, 8:116–143, 2013. doi:10.1007/s11467-013-0303-2.

[HSK94] 0. Hilt, W.F. Schmidt, and A.G. Khtapak. Ionic Mobilities in Liquid Xenon. *IEEE Transactions on Dielectrics and Electrical Insulation*, 1(4), August 1994.

[HSS97] Wayne Hu, Naoshi Sugiyama, and Joseph Silk. The Physics of microwave background anisotropies. *Nature*, 386:37–43, 1997. doi:10.1038/386037a0.

[Hu08] Wayne Hu. Lecture Notes on CMB Theory: From Nucleosynthesis to Recombination. *ArXiv e-prints*, 2008. ArXiv:[0802.3688].

[JKG96] Gerard Jungman, Marc Kamionkowski, and Kim Griest. Supersymmetric dark matter. *Phys. Rept.*, 267:195–373, 1996. doi:10.1016/0370-1573(95)00058-5.

[K+92] V.V. Kuz'minov et al. Radioactive Kr85 in Krypton Enriched with a Light Isotope. *Atomic Energy*, (73):1010–1011, December 1992.

[KK98] Marc Kamionkowski and Ali Kinkhabwala. Galactic halo models and particle dark-matter detection. *Phys. Rev. D*, 57:3256–3263, 1998. doi:10.1103/PhysRevD.57.3256.

[KK04] Andriy Kurylov and Marc Kamionkowski. Generalized analysis of weakly interacting massive particle searches. *Phys. Rev.*, D69:063503, 2004. doi:10.1103/PhysRevD.69.063503.

[KO96] K. Kitao and M. Oshima. Table of Radioactive Isotopes - Xenon-127, 1996. `http://ie.lbl.gov/toi/nuclide.asp?iZA=540127` - accessed 25 February 2015.

[KSLB14] Prajwal Raj Kafle, Sanjib Sharma, Geraint F. Lewis, and Joss Bland-Hawthorn. On the Shoulders of Giants: Properties of the Stellar Halo and the Milky Way Mass Distribution. *Astrophys. J.*, 794(1):59, 2014. doi:10.1088/0004-637X/794/1/59.

[KYYK15] J. Koda, M. Yagi, H. Yamanoi, and Y. Komiyama. Approximately a Thousand Ultra-diffuse Galaxies in the Coma Cluster. *Astrophys. J.*, 807:L2, 2015. doi:10.1088/2041-8205/807/1/L2.

[LA+13] LHCb collaboration, R. Aaij, et al. Measurement of the $B_s^0 \to \mu^-\mu^+$ branching fraction and search for $B^0 \to \mu^-\mu^+$ decays at the LHCb experiment. *Phys. Rev. Lett.*, 111:101805, 2013. doi:10.1103/PhysRevLett.111.101805.

[Lem31] Abbé G. Lemaître. A Homogeneous Universe of Constant Mass and Increasing Radius accounting for the Radial Velocity of Extra-galactic Nebulæ. *Mon. Not. Roy. Astron. Soc.*, 91(5):483–490, 1931. doi:10.1093/mnras/91.5.483.

[Lin13] A. Lindote. First results from the LUX experiment. In *LIP seminar*, 2013.

[LM15] Julien Lavalle and Stefano Magni. Making sense of the local Galactic escape speed estimates in direct dark matter searches. *Phys. Rev.*, D91(2):023510, 2015. doi:10.1103/PhysRevD.91.023510.

[LMF11] E.W. Lemmon, M.O. McLinden, and D.G. Friend. Thermophysical Properties of Krypton, 2011. `http://webbook.nist.gov/cgi/fluid.cgi?ID=C7439909&Action=Page` - accessed 02 March 2015.

[LS96] J. D. Lewin and P. F. Smith. Review of mathematics, numerical factors, and corrections for dark matter experiments based on elastic nuclear recoil. *Astropart. Phys.*, 6:87–112, 1996. doi:10.1016/S0927-6505(96)00047-3.

[M+14] D.C. Malling et al. Radiogenic and Muon-Induced Backgrounds in the LUX Dark Matter Detector. *Astro-ph.IM*, March 2014. arXiv:[1403.1299v1].

[Mal13] D.C. Malling. Low Energy Backgrounds Estimates from ^{222}Rn. Internal LUX Collaboration document, 2013.

[Mal14] D.C. Malling. *Measurement and Analysis of WIMP Detection Backgrounds, and Characterization and Performance of the Large Underground Xenon Dark Matter Search Experiment.* PhD thesis, Physics Department at Brown University, Providence, Rhode Island, May 2014.

[McC10] Christopher McCabe. Astrophysical uncertainties of dark matter direct detection experiments. *Phys. Rev. D*, 82:023530, July 2010. doi:10.1103/PhysRevD.82.023530.

[MCK+10] A. Manzur, A. Curioni, L. Kastens, D.N. McKinsey, K. Ni, and T. Wongjirad. Scintillation efficiency and ionization yield of liquid xenon for monoenergetic nuclear recoils down to 4 keV. *Phys. Rev.*, 81(2), February 2010. doi:10.1103/PhysRevC.81.025808.

[Mel99] Yannick Mellier. Probing the universe with weak lensing. *Ann. Rev. Astron. Astrophys.*, 37:127–189, 1999. doi:10.1146/annurev.astro.37.1.127.

[MH06] D.M. Mei and A. Hime. Muon-induced background study for underground laboratories. *Phys. Rev. D*, 73:053004, Mar 2006. doi:10.1103/PhysRevD.73.053004.

[Oor32] J.H. Oort. The force exerted by the stellar system in the direction perpendicular to the galactic plane and some related problems. *Bulletin of the Astronomical Institutes of the Netherlands*, 6:249, 1932.

[P+97] S. Perlmutter et al. Measurements of the cosmological parameters Ω and Λ from the first 7 supernovae at $z \geq 0.35$. *Astrophys. J.*, 483:565, 1997. doi:10.1086/304265.

[P+14] T. Piffl et al. The RAVE survey: the Galactic escape speed and the mass of the Milky Way. *Astron. Astrophys.*, 562:A91, 2014. doi:10.1051/0004-6361/201322531.

[PA+14] Planck Collaboration, P.A.R. Ade, et al. Planck 2013 results. XVI. Cosmological parameters. *Astron. Astrophys.*, 571:A16, 2014. doi:10.1051/0004-6361/201321591.

[PA+15] Planck Collaboration, P.A.R. Ade, et al. Planck 2015 results. XIII. Cosmological parameters. *astro-ph.CO*, February 2015. arXiv:[1502.01589].

[PW65] A.A. Penzias and R.W. Wilson. A Measurement of Excess Antenna Temperature at 4080 Mc/s. *"Astrophys. J."*, 142:419–421, 1965. doi:10.1086/148307.

[RL13] Lea Reichhart and Alex Lindote. Efficiency study using flat NR simulations processed with DPF stable release version 1.3. Internal LUX Collaboration document, 2013.

[Rob35] H.P. Robertson. Kinematics and World-Structure. *Astrophys. J.*, 82(12):284, 1935. doi:10.1086/143681.

[Rob74] J.W. Robinson. *Handbook of Spectroscopy*, volume 1, pages 4–22. CRC Press, Cleveland, 1974.

[Rod57] A. W. Rodgers. Radius Variation and Population Type of Cepheid Variables. *Mon. Not. Roy. Astron. Soc.*, 117(1):85–94, 1957. doi:10.1093/mnras/117.1.85.

[RT15] Marco Roncadelli and Fabrizio Tavecchio. No axions from the Sun. *Mon. Not. Roy. Astron. Soc.*, 450(1):L26–L28, 2015. doi:10.1093/mnrasl/slv040.

[Rub83] V.C. Rubin. Dark matter in spiral galaxies. *Scientific American*, 248:96–106, 1983. doi:10.1038/scientificamerican0683-96.

[Ryd03] B. Ryden. *Introduction to cosmology.* Addison-Wesley 244 p, San Francisco, USA, 2003.

[S^+11] V.N. Solovov et al. Position Reconstruction in a Dual Phase Xenon Scintillation Detector. *accepted for publication in IEEE Trans. on Nuc. Sci*, 2011. doi:10.1109/TNS.2012.2221742.

[S^+12] N. Suzuki et al. The Hubble Space Telescope Cluster Supernova Survey. V. Improving the Dark-energy Constraints above z ¿ 1 and Building an Early-type-hosted Supernova Sample. *Astrophys. J.*, 746(1):85, 2012. doi:10.1088/0004-637X/746/1/85.

[SBK^+11] M. Szydagis, N. Barry, K. Kazkaz, J. Mock, D. Stolp, M. Sweany, M. Tripathi, S. Uvarov, N. Walsh, and M. Woods. NEST: a comprehensive model for scintillation yield in liquid xenon. *Journal of Instrumentation*, 6(10):P10002, 2011. doi:10.1088/1748-0221/6/10/P10002.

[Sca06] R. Scarpa. Modified Newtonian Dynamics, an Introductory Review. In E.J. Lerner and J.B. Almeida, editors, *First Crisis in Cosmology Conference*, volume 822 of *American Institute of Physics Conference Series*, pages 253–265, 2006. doi:10.1063/1.2189141.

[Sch10] R.W. Schnee. Introduction to Dark Matter Experiments. *Astro-ph.CO*, pages 629–681, 2010. arXiv:1101.5205 [astro-ph.CO].

[SD11] P. Sorensen and C.E. Dahl. Nuclear recoil energy scale in liquid xenon with application to the direct detection of dark matter. *Phys. Rev. D*, 83(6):063501, March 2011. doi:10.1103/PhysRevD.83.063501.

[Sha15] Sally Shaw. Gamma counting in U238 and Th232 decay chains in Geant4. Internal LZ Collaboration document, August 2015.

[Sie91] H. Sievers. Table of Radioactive Isotopes - Krypton-85, 1991. `http://ie.lbl.gov/toi/nuclide.asp?iZA=360085` - accessed 25 February 2015.

[SIK^+13] Anse Slosar, Vid Irsic, David Kirkby, Stephen Bailey, Nicolas G. Busca, et al. Measurement of Baryon Acoustic Oscillations in the Lyman-alpha Forest Fluctuations in BOSS Data Release 9. *J. Cosmology and Astrop. Phys.*, 1304:026, 2013. doi:10.1088/1475-7516/2013/04/026.

[Sil15] C.P. Silva. Weighting LUX using tritium. Internal LUX Collaboration document, 2015.

[Soc01] Heath Physics Society. Human Health Fact Sheet: Krypton, October 2001. `http://hpschapters.org/northcarolina/NSDS/krypton.pdf` - accessed 27 February 2015.

[Ste15] Gary Steigman. CMB Constraints On The Thermal WIMP Mass And Annihilation Cross Section. *Phys. Rev.*, 91, 2015. doi:10.1103/PhysRevD.91.083538.

[SZ70] R.A. Sunyaev and Y.B. Zeldovich. Small-Scale Fluctuations of Relic Radiation. *Astrophysics and Space Science*, 7:3–19, 1970. doi:10.1007/BF00653471.

[T^+06] Max Tegmark et al. Cosmological Constraints from the SDSS Luminous Red Galaxies. *Phys. Rev.*, D74:123507, 2006. doi:10.1103/PhysRevD.74.123507.

[T^+07] P. Tisserand et al. Limits on the Macho Content of the Galactic Halo from the EROS-2 Survey of the Magellanic Clouds. *Astron. Astrophys.*, 469:387–404, 2007. doi:10.1051/0004-6361:20066017.

[Tul] Jagdish K. Tuli. Chart of Nuclides. `http://www.nndc.bnl.gov/chart/` - accessed 20 July 2015.

[vBBS85] T.S. van Albada, J.N. Bahcall, K. Begeman, and R. Sancisi. Distribution of dark matter in the spiral galaxy NGC 3198. *Astrophys. J.*, 295:305–313, August 1985. doi:10.1086/163375.

[vBC13] Karl van Bibber and Gianpaolo Carosi. Status of the ADMX and ADMX-HF experiments. *physics.ins-det*, 2013. arXiv:1304.7803.

[Viv10] L. Viveiros. *Optimization of Signal versus Background in Liquid Xe Detectors Used for Dark Matter Direct Detection Experiments.* PhD thesis, Physics department at Brown University, Providence, Rhode Island, May 2010.

[WHC^+15] Wenting Wang, Jiaxin Han, Andrew P. Cooper, Shaun Cole, Carlos Frenk, and Ben Lowing. Estimating the dark matter halo mass of our Milky Way using dynamical tracers. *Astro-ph.GA*, July 2015. arXiv:1502.03477.

[Wol] WolframAlpha. krypton 85. `http://www.wolframalpha.com/input/?i=krypton+85` - accessed 27 February 2015.

[Zwi33] F. Zwicky. Die Rotreshiebung von extragalaktishen Nebeln. *Helv. Phys. Acta*, 6:110–127, 1933.

[Zwi37] F. Zwicky. On the Masses of Nebulae and of Clusters of Nebulae. *Astrophys. J.*, 86:217, October 1937. doi:10.1086/143864.

Attachments

Appendix A

Decay Schemes and Decay chains

Decay schemes of common LUX internal sources.

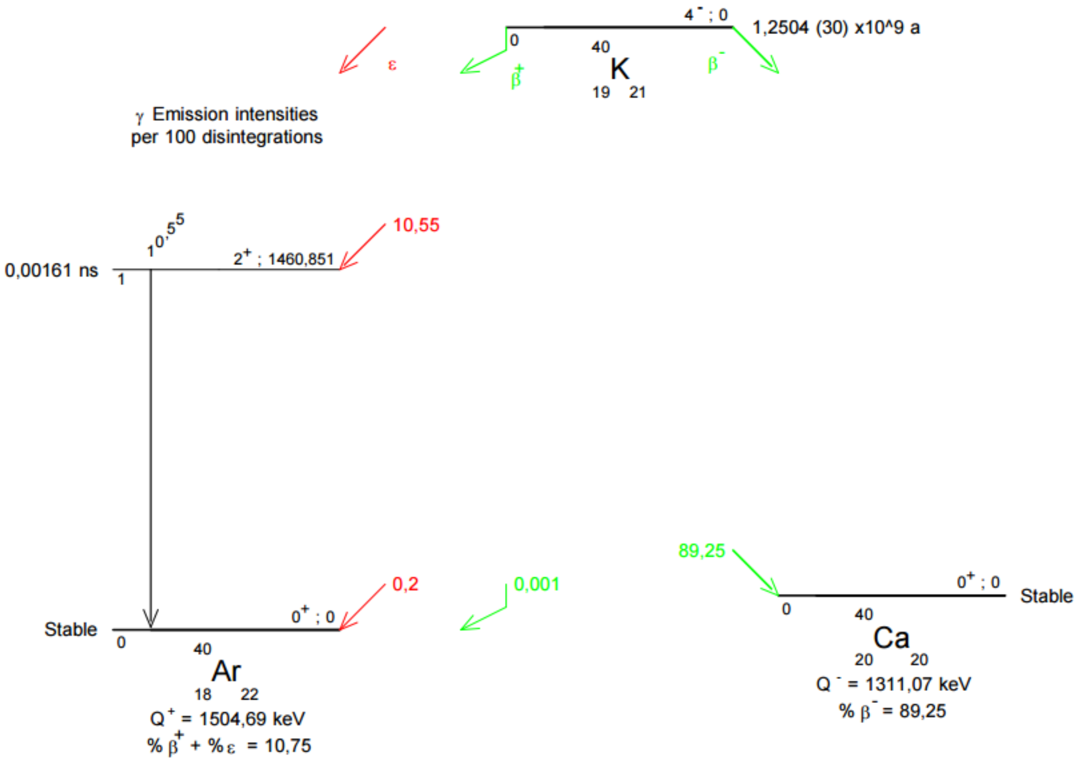

Figure A.1: Decay scheme for potassium-40.

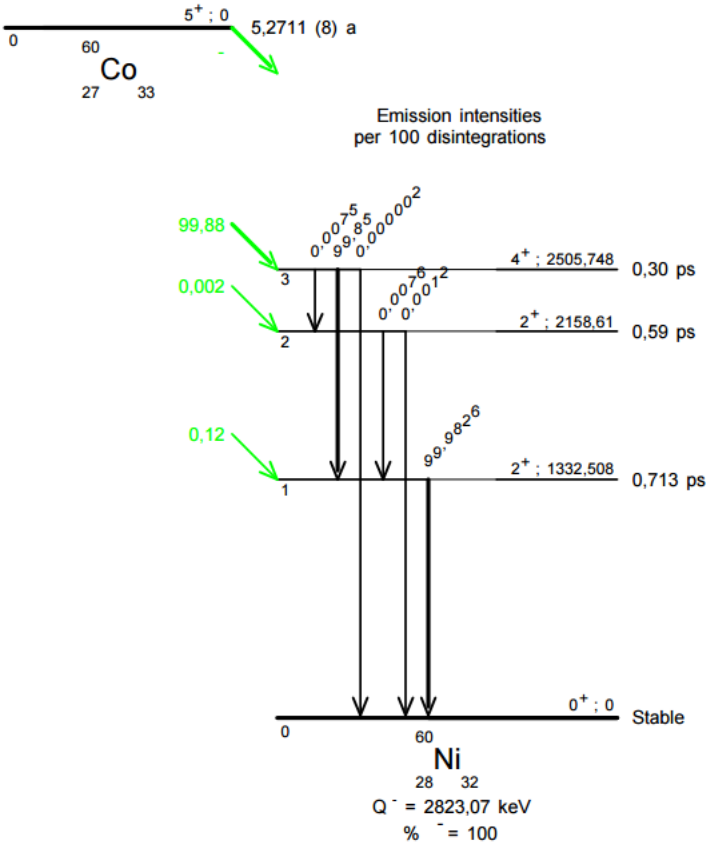

Figure A.2: Decay scheme for cobalt-60.

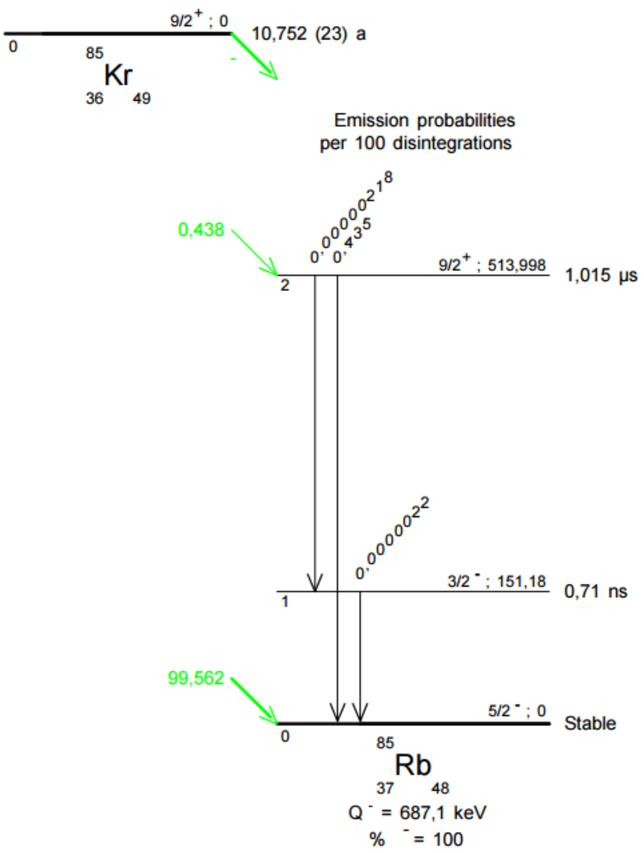

Figure A.3: Decay scheme for krypton-85.

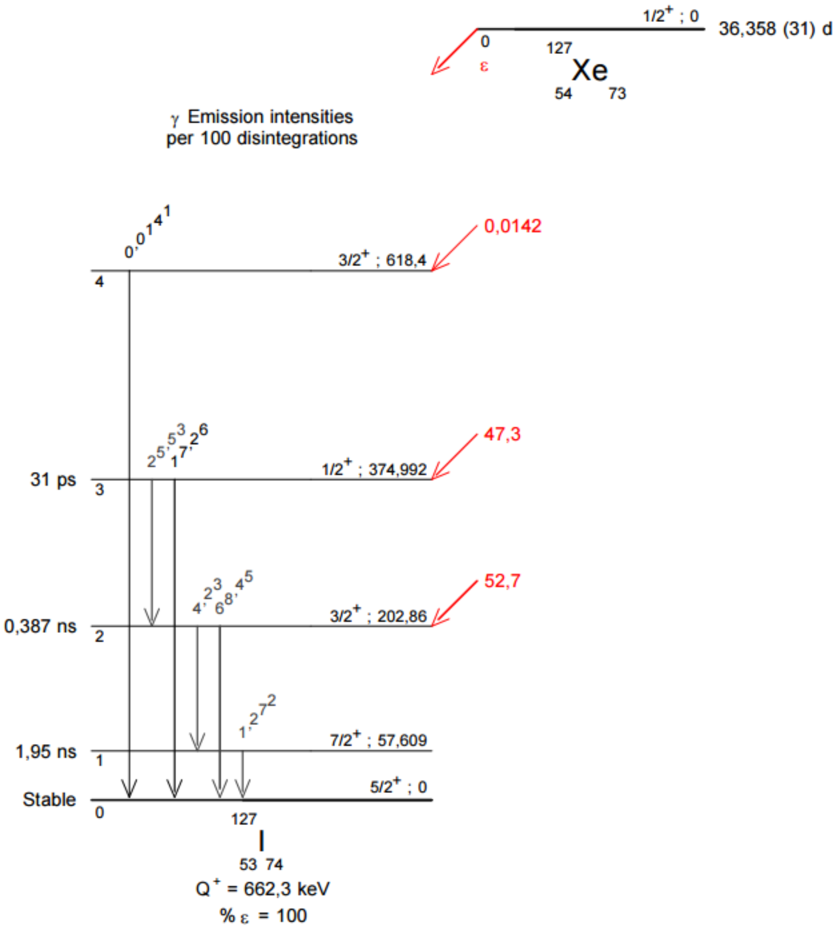

Figure A.4: Decay scheme for xenon-127.

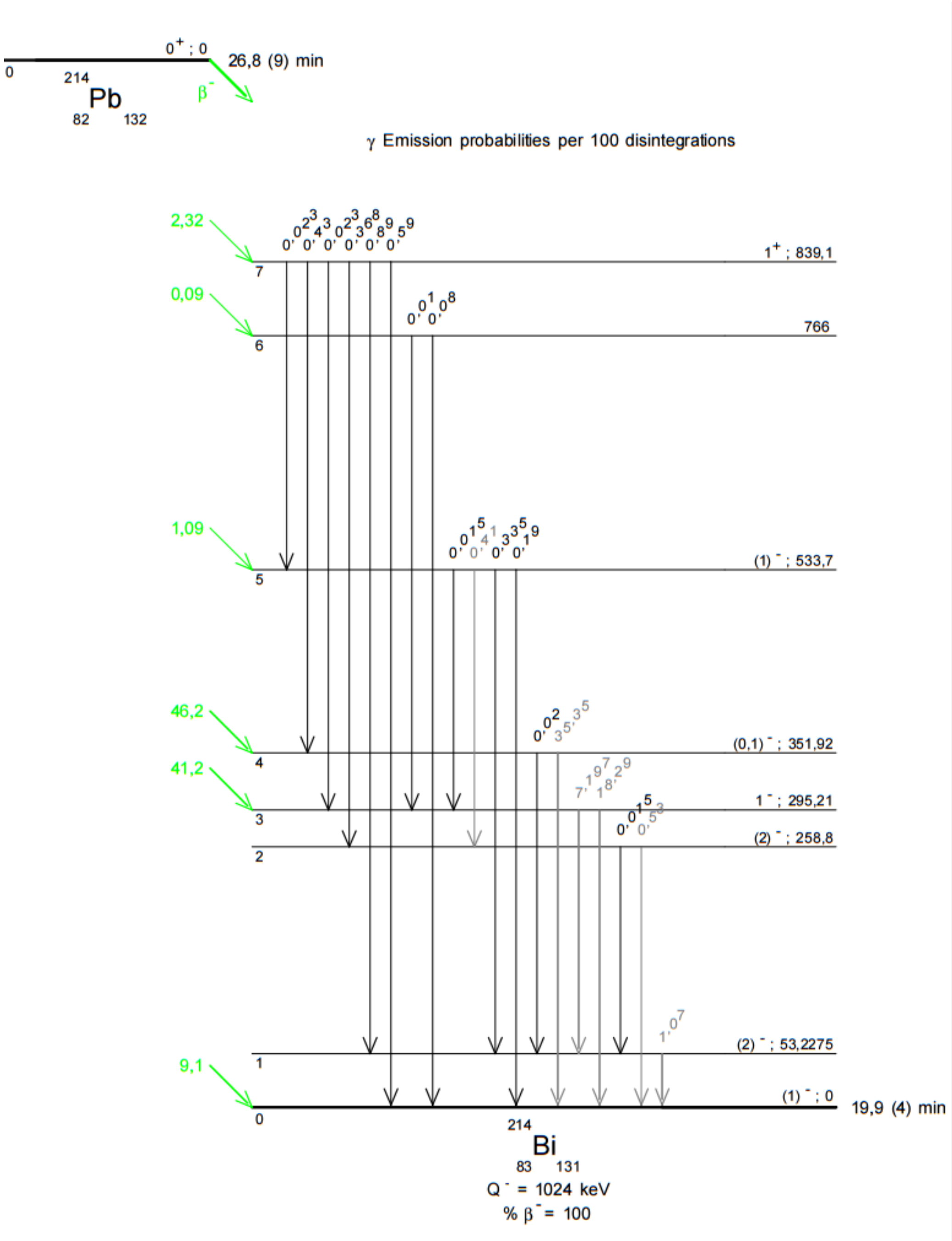

Figure A.5: Decay scheme for lead-214.

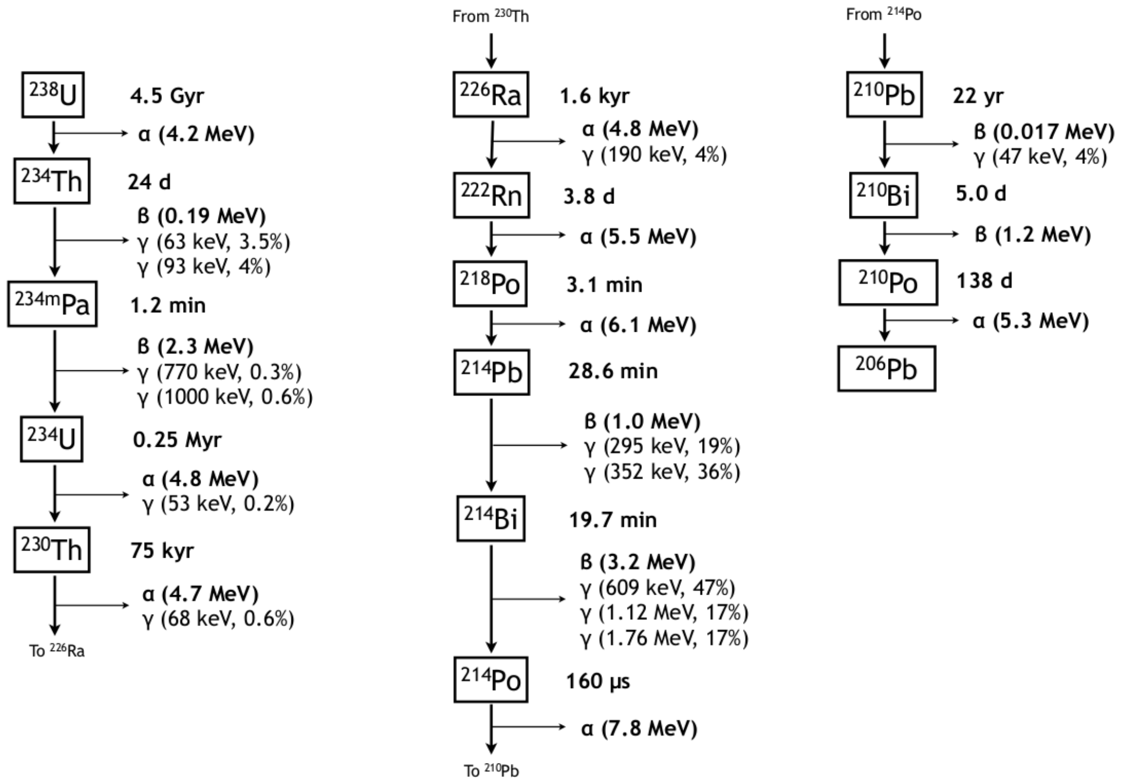

Figure A.6: Uranium series diagram evidencing the main radiation energies emitted by each isotope. The Uranium decay chain starts with the naturally-occurring isotope ^{238}U and terminates with the stable ^{206}Pb following a $4n + 2$ rule for the mass number [FT13]. The total energy release for this chain is 51.7 MeV. The isotope ^{222}Rn, with a half-life of $T_{hl} = 3.8$ d, is produced along this decay chain. Figure taken from [Mal14].

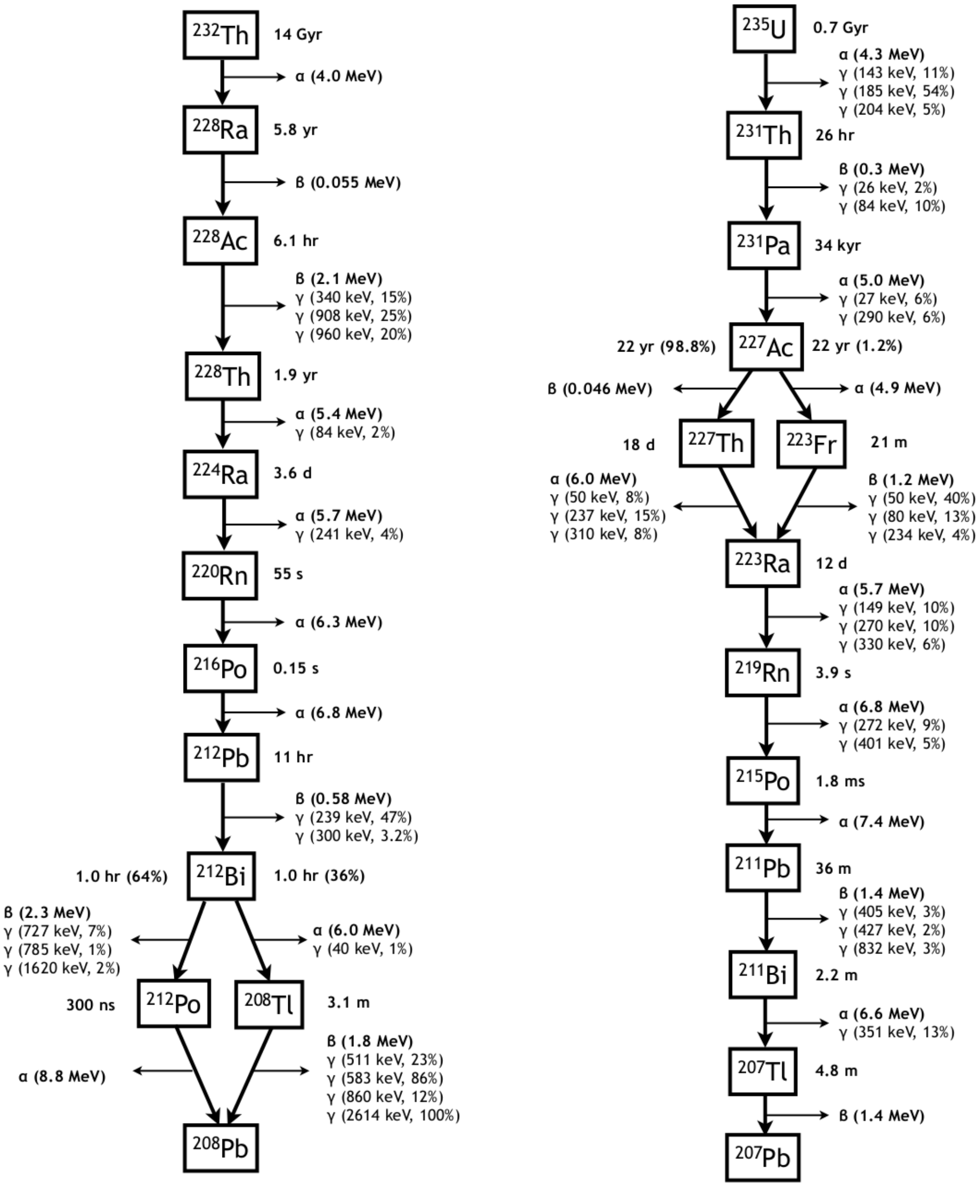

Figure A.7: From left to right: the Thorium and Actinium series. The Actinium decay chain starts with the naturally-occurring isotope ^{235}U and terminates with the stable ^{207}Pb following a $4n+3$ rule for the mass number A [FT13]. The total energy release for this chain is 46.4 MeV. The Thorium decay chain starts with the naturally-occurring isotope ^{232}Th and terminates with the stable ^{208}Pb following a $4n$ rule for the mass number. The total energy release for this chain is 42.6 MeV. The isotopes ^{219}Rn ($T_{hl} = 4$ s) and ^{220}Rn ($T_{hl} = 55$ s) are produced along the Actinium and Thorium decay chains, respectively. Figure taken from [Mal14].

Appendix B

List of the γ ray sources considered in the background analysis

Table B.1: Activities and number of events simulated for all the γ ray sources considered in the background analysis.

Component	**Isotope**	**Activity [mBq]**	**Events simulated** ($\times 10^3$)
Cryostat	^{40}K	369.6	27250
	^{226}Ra	85.47	58500
	^{46}Sc	1016.4	74750
	^{232}Th early	184.8	41250
	^{232}Th late	184.8	110000
Top PMT and bases	^{60}Co	160.43	23750
	^{40}K	4099.2	602250
	^{226}Ra	664.9	879750
	^{232}Th early	172.63	76500
	^{232}Th late	172.63	204000
Bottom PMT and bases	^{60}Co	160.43	23750
	^{40}K	4099.2	602250
	^{226}Ra	664.9	879750
	^{232}Th early	172.63	76500
	^{232}Th late	172.63	204000
PMT mounts	^{60}Co	287.3	21250
	^{226}Ra	371.8	247500
	^{232}Th early	490.1	108000
	^{232}Th late	490.1	288000

Component	**Isotope**	**Activity [mBq]**	**Events simulated** ($\times 10^3$)
Superinsulation (Mylar)	^{40}K	1408	103500
	^{226}Ra	160.6	108000
	^{232}Th early	30.8	7500
	^{232}Th late	30.8	20000
Top shield	^{60}Co	205.7	15250
	^{226}Ra	266.2	177750
	^{232}Th early	350.9	78000
	^{232}Th late	350.9	208000
Filler chiller shield	^{60}Co	498.1	36750
	^{226}Ra	644.6	427500
	^{232}Th early	849.7	187500
	^{232}Th late	849.7	250000
Electric field grids	^{60}Co	6.3	500
	^{40}K	1.8	250
	^{226}Ra	6.3	4500
	^{232}Th early	1.035	750
	^{232}Th late	1.035	2000
Field shaping rings	^{60}Co	8.4	750
	^{226}Ra	14	11250
	^{232}Th early	22.4	5250
	^{232}Th late	22.4	14000
Field ring supports	^{226}Ra	106.65	72000
	^{232}Th early	54.35	12000
	^{232}Th late	54.35	32000
PTFE grid supports	^{226}Ra	46.5	31500
	^{232}Th early	12.09	3000
	^{232}Th late	12.09	8000
Reflector panels	^{226}Ra	46.5	31500
	^{232}Th early	15.5	3750
	^{232}Th late	15.5	10000
Thermal Insulation	^{40}K	600	44250
	^{226}Ra	780	517500
	^{232}Th early	330	72750
	^{232}Th late	330	194000